IOWA STATE UNIVERSITY
Digital Repository

2013

Raman spectroscopic characterization and analysis of agricultural and biological systems

Qi Wang
Iowa State University

**Raman spectroscopic characterization and analysis
of agricultural and biological systems**

by

Qi Wang

A dissertation submitted to the graduate faculty

in partial fulfillment of the requirements for the degree of

DOCTOR OF PHILOSOPHY

Major: Agricultural Engineering

Program of Study Committee:
Chenxu Yu, Major Professor
Jacek Adam Koziel
Kenneth J Koehler
Lie Tang
Sinisa Grozdanic

Iowa State University
Ames, Iowa
2013

TABLE OF CONTENTS

LIST OF TABLES

LIST OF FIGURES

ABSTRACT

Technical progresses in the past two decades in instrumental design, laser and electronic technology, and computer-based data analysis have made Raman spectroscopy, a noninvasive, nondestructive optical molecular spectroscopic imaging technique, an attractive choice for analytical tasks. Raman spectroscopy provides chemical structural information at molecular level with minimal sample preparation in a quick, easy-to-operate and reproducible fashion. In recent years it has been applied more and more to the analysis and characterization of agricultural products and biological samples. This dissertation documents the innovative research in Raman spectroscopic characterization and analysis in both biomedical and agricultural systems that I have been working on throughout my PhD training.

The biomedical research conducted was focused on glaucoma. Glaucoma is a chronic neurodegenerative disease characterized by apoptosis of retinal ganglion cells and subsequent loss of visual function. Early detection of pathological changes and progression in glaucoma and other neuroretinal diseases, which is critical for the prevention of permanent structural damage and irreversible vision loss, remains a great challenge. In my research, the Raman spectra from canine retinal tissues were subjected to multivariate discriminant analysis with a support vector machine algorithm to differentiate disease tissues versus healthy tissues. The high classification accuracy suggests that Raman spectroscopic screening can be used for *in vitro* detection of glaucomatous changes in retinal tissue not only at late stage but also at early stage with high specificity.

To expand the scope of application of Raman analysis, it was also applied to characterize agricultural and food materials. More specifically, Raman spectroscopy was applied to analyze meat. Existing objective methods (e.g., mechanical stress/strain analysis,

near infrared spectroscopy) to predict sensory attributes of pork in general do not yield satisfactory correlation to panel evaluations. Raman spectroscopic methodology was investigated in this study to evaluate and predict tenderness, juiciness and chewiness of fresh, uncooked pork loins from 169 pigs. The method developed in this thesis yielded good prediction of sensory attributes such as tenderness and chewiness, and it has the potential to become a rapid objective assay for tenderness and chewiness of pork products that may find practical applications in pork industry. In addition, a Raman spectroscopic screening method in conjunction with discriminant modeling was developed for rapid evaluation of boar taint level in pork. Through the research demonstrated in this dissertation, Raman spectroscopy has been shown to have great potential to address analytical needs in new fields with great potential for innovative applications.

Chapter 1. GENERAL INTRODUCTION

1.1 Introduction

1.1.1 Raman spectroscopy and its instrumentation

The phenomenon of inelastic scattering of light by matter was first observed experimentally by C.V. Raman, an Indian physics professor, and his collaborator K.S. Krishnan in1928 (Raman and Krishnan 1928). In 1930, he won the Nobel Prize in physics for his work on the scattering of light and for the discovery of the effect named after him.

The mechanism for Raman scattering lies in the change of the rotational or vibrational quantum states of molecules being illuminated. When light shines on a sample most of the scattering that takes place is elastic with no loss of energy, and therefore no frequency change, this is known as Rayleigh scattering (Figure 1.1). Raman scattering, however, is due to inelastic scattering of the incident photons whereby energy is transferred to or received from the sample due to changes in the vibrational or rotational modes of sample molecules, causing a change in the energy, and therefore the frequency of the scattered light. If the incident photon gives up energy to the sample it is scattered with a red-shifted frequency and referred to as stokes shift (Figure 1.1). If the molecule is already in an exited energy state, and gives energy to the scattered photon, the output has a blue-shifted frequency, and is referred to as anti-stokes shift (Figure 1.1). Because the probability of a molecule being in an excited state is much lower than being in the ground state, the anti-stokes shift occurs much less frequently than the stokes-shift. In most cases, the Raman scattering photons collected and analyzed are the Stokes photons, referred to as Stokes lines. Although the rarity of anti-stokes photons result in much weaker anti-stokes lines, they are sometimes favored in analysis due to absence of fluorescence interference, which could be a

big problem for stokes lines. It is important to note that Raman scattering is much different from fluorescence (Figure 1.1). In fluorescence, the incoming photon is completely absorbed by the molecule and causes an electronic energy state change. A fluorescent photon is later released when the molecule relaxes back to a lower energy state (Szymanski 1967) whereas Raman scattered photon is released instantaneously.

The selection rule governing Raman scattering is determined by changes in polarizibility during the vibration (Ingle Jr and Crouch 1988), which is different from another vibrational spectroscopic technique – infrared spectrometry (IR). In IR spectroscopy, the frequency of incident light has to match the energy differences between ground and excited vibrational states (Figure 1.1); and the energy loss of the incident light is detected. The molecular vibration can only be observed in IR spectroscopy when there is a change in dipole moment during vibration. Raman scattering spectrum provides essentially the same type of information as the infrared (IR) absorption spectrum, namely, the energies of molecular vibrational modes. However, the two methods differ fundamentally in mechanism and selection rules, and each has specific advantages and disadvantages for biological applications(Miura and Thomas Jr 1995) For example, it is problematic to compare quantitatively the scattering intensities of Raman bands, whereas IR absorption intensities are governed by Beer's Law. Conversely, water is a notoriously strong IR-absorbing medium, and aqueous systems cannot be investigated with ease by IR methods. In contrast, water interferes only feebly with Raman spectra of aqueous solutions and hydrated solids.
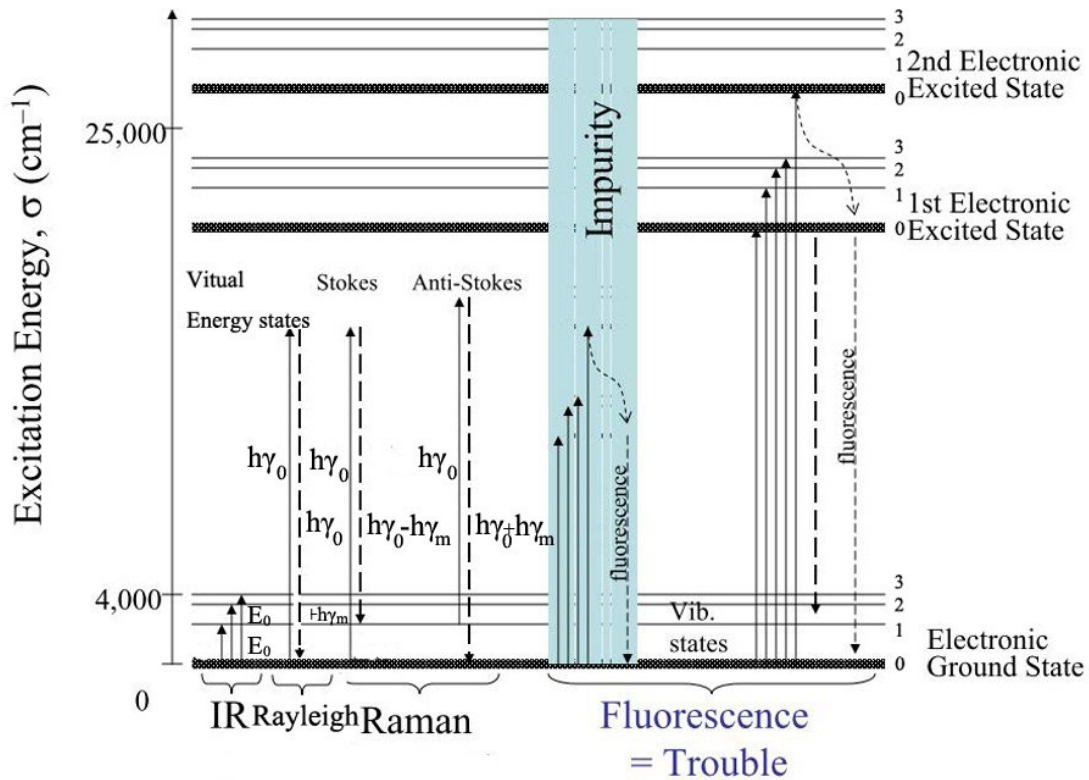
Figure 1.1 Diagram of Rayleigh, Raman scattering, and fluorescence processes

The frequency shift, Raman shift, is a measure of the energy of the molecular vibrational modes. Raman measurements hence provide valuable information for molecular characterization of complex systems(Braiman 2006). Figure 1.2 shows a typical schematics of Raman instrumentation for biological samples(Hata, Scholz et al. 2000). Excitation light from an argon laser is routed via optical fiber, beam expanding lens L3, laser bandpass filter F2, dichroic mirror BS, and lens L2 to the tissue. The Raman shifted backscattered light is collimated by lens L2, directed through BS, filtered by holographic rejection filter F1, focused by lens L1on to a fiber, and sent to a spectrograph. The wavelength dispersed signals are detected by a charge-coupled array detector CCD, and displayed on a computer monitor (PC).
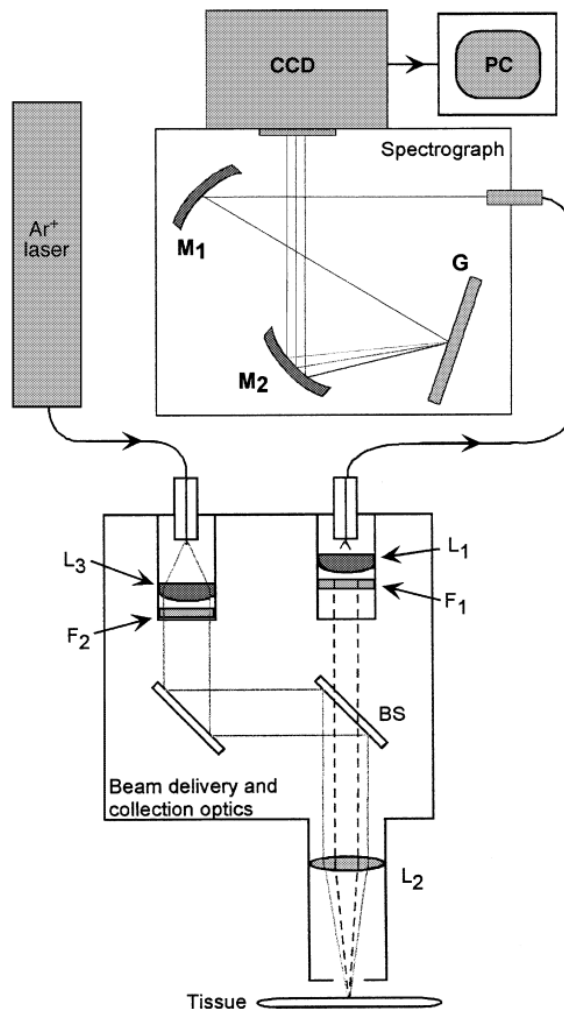
Figure 1.2 Schematics of basic Raman scattering instrumentation.

The successful application of Raman spectroscopy to bioanalysis is a direct result of the advances in Raman instrument design. Better detectors, spectrometers, Rayleigh rejection filters, sources and collection optics have shortened analysis time and increased signal-to-noise ratios. It is now possible to observe and study Raman signals from materials that would have been completely out of reach by many orders of magnitude at the time Raman discovered the effect. Moreover, with the advent of commercial 'read-to-use' Raman spectrometers, and even portable systems, the technique becomes increasingly available to a wider range of users(Mukhopadhyay 2007).

1.1.2   Application of Raman spectroscopy

1.1.2.1 General application

Over the past twenty years, there have been plenty of literatures published in Raman spectroscopic applications. (Long 2002; Demtröder 2003); W. Kiefer has published a review of recent advances in Raman spectroscopy with over 300 references of key developments published only in the Journal of Raman spectroscopy until 2007 (Kiefer 2007), which reported applications of Raman spectroscopy in the fields of art and archeology(Bellot-Gurlet, Pagès-Camagna et al. 2006), biosciences(Schweitzer-Stenner 2005), vibrational studies and analytical chemistry(Tuttolomondo, Navarro et al. 2005), solid state physics(minerals, crystals, glasses, ceramics, etc.)(Frost, Wills et al. 2005), liquids and liquid interactions(Kwac and Cho 2005), and nano-materials(Schmitt and Popp 2006). Here I intend to highlight applications of Raman spectroscopy in biology in which it has several advantages. Raman spectroscopy is noninvasive and nondestructive, it requires minimal sample preparation and small sample volume. In addition, Raman spectroscopy, unlike IR spectroscopy, does not suffer from severe water interference. Since water is omnipresent in biological systems, Raman spectroscopy is especially suitable for analyzing biological samples(De Gelder, De Gussem et al. 2007).

1.1.2.2 General application in Bio-medical systems

Due to these advantages, Raman spectroscopy has been widely utilized for biomedical analysis(Pappas, Smith et al. 2000; Notingher 2007). Raman spectroscopy is extremely suitable for probing the relationship between structure, dynamics and function of biomolecules (e.g. synthetic polypeptides, proteins, pharmacologically relevant molecules, vitamins, etc.)(Schmitt and Popp 2006). Furthermore, human and animal tissues provide

exciting prospects for the application of Raman imaging. Diseases and other pathological anomalies cause chemical and structural changes at the molecular level which can be captured by the Raman spectral measurements(Krafft and Sergo 2006), and the resulted Raman spectral changes can be used as sensitive and phenotypic spectral markers for the diseases(Erckens, Jongsma et al. 2001). These spectral markers are very specific and unique, so that they can be considered as fingerprints of the pathological samples(Katz, Kruger et al. 2003; Wang, Grozdanic et al. 2011). Small structural features and compositional differences provide Raman spectral markers for a variety of disease states, such as brain cancer(Koljenovi, cacute et al. 2002), gastrointestinal disorders(Kendall, Stone et al. 2003) and dental disease (Ko, Hewko et al. 2005). Raman spectra have also been used to develop classification models to diagnose certain cancers. Such as bladder cancer(De Jong, Schut et al. 2006), prostatic cancer(Panza and Maier 2007), basal cell carcinoma(Nijssen, Schut et al. 2002). The potential benefits of using Raman spectroscopy to diagnose breast cancer have been studied by several research groups(Frank, McCreery et al. 1995; Haka, Shafer-Peltier et al. 2005; Chowdary, Kumar et al. 2006; Yu, Gestl et al. 2006; Brożek-Płuska, Placek et al. 2008; Stone and Matousek 2008). The surfaced enhanced Raman scattering (SERS) microscopy, which enhances the intensity of the Raman scattered signal from an analyte by orders of 10^6 or more, combines the advantage of bio-functionalized metal nanoparticles and Raman micro-spectroscopy. At the single-nanoparticle level, recent theoretical work by Xu et al. (Xu, Aizpurua et al. 2000) suggested that the maximum enhancement factor through electromagnetic fields is about 10^{11}. SERS is capable of providing detailed spectroscopic information and is a novel method of vibrational micro-spectroscopic imaging for the selective detection and identification of single biomolecules such as protein and DNA located

on the nanoparticle surface or at the junction of two particles under ambient conditions in targeted research(Sun, Yu et al. 2007; Yu and Irudayaraj 2007; Yu, Varghese et al. 2007).

1.1.2.3 Application in ocular system and glaucoma

The eyes are the most important sensory organs and the window to the soul. Raman spectroscopy has also been applied in ocular system. Based on functional illustrations, the eyeball can be simplified as three major structures, from the outer to inner layers, to achieve focusing and the transmission of light (Figure 1.3). The cornea and sclera layers can be found in the outermost layer. The middle layer consists of the choroid, ciliary body, lens, and iris. As light penetrates into the eyes from the environment, the photosensitive cells in the retina (the innermost layer) receive the light. According to specific structures in eye anatomy, ocular diseases can be further clinically classified into five groups: infectious, immunologic, congenital, degenerative, and traumatic diseases. Clinical approaches for ophthalmic diseases are based on the general medical approach but pay more attention to information regarding subjective vision and ocular structures. Measurement of Raman spectra has been developed as a novel qualitative and quantitative optical technique by the scattering of radiation to improve the diagnostic quality, rapidity and convenience.
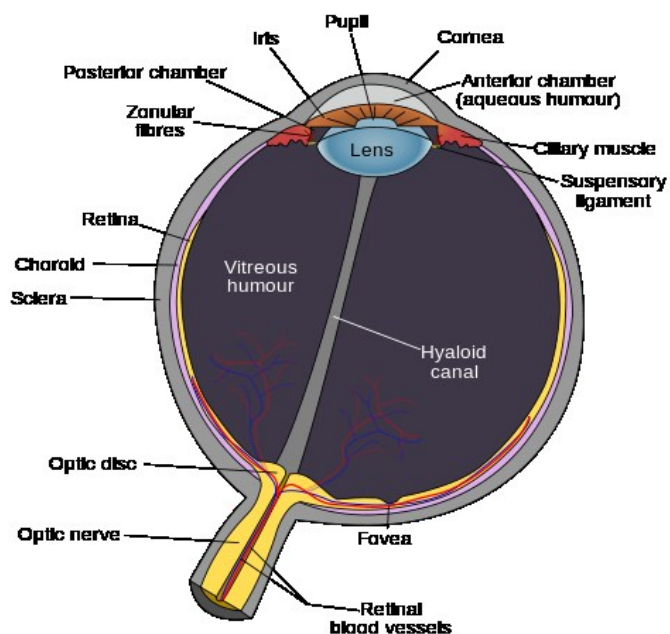
Figure 1.3 Schematic diagram of the human eye.

Water makes up about 78% of normal human cornea. Disorder of the cornea drainage functions may result in corneal edema. Moreover, water accumulated in cornea will decrease the transparency of the cornea due to scattering of penetrating light. Water content in cornea is important information clinically when patients receive laser refractive surgery. Imprecise instrument setting might increase the risk of overtreatment or undertreatment. Therefore, some researchers have focused on using a noninvasive diagnostic tool for measurement of water content in ocular tissues(Mizuno, Toshima et al. 1990). Siew et al. applied micro-Raman spectroscopy to study the total water content in organ-cultured cornea(Siew, Clover et al. 1995). Erckens et al. studied biomolecules in ocular tissues and aqueous humour solutions(Erckens, Motamedi et al. 1997). Bauer and co-workers investigated the water content of cornea by analyzing the ratio of Raman intensities of the OH-bond (approximately 3400cm-1) and the CH-bond(approximately 2940 cm-1)(Bauer, Wicksted et al. 1998). The

reported the sensitivity of using Raman spectra for water content analysis was higher by approximately 0.1mg H2O/mg drt-wt. Other noninvasive investigation and assessment of corneal hydration based on a confocal Raman spectroscopic technique was achieved in vivo by the same group(Bauer, Hendrikse et al. 1999). The mechanism for cataract formation is an interesting topic for ophthalmologists and vision scientists. State of cataract transformation may be related to the change of proteins and lipids compositions in lens directly (Siebinga, Vrensen et al. 1992; Lin, Li et al. 1998; Chen, Cheng et al. 2005). Molecular fingerprint information from Raman spectra can be assigned to the specific proteins. The changes in spectral intensity may be related to the differences in concentration. Age-related macular degeneration (AMD) is a leading cause of irreversible blindness in the elderly ($\geq$65 years old). Macular pigment (MP) in the human retina is composed of three carotenoids, lutein, zeaxanthin and meso-zeaxanthin(Sharifzadeh, Zhao et al. 2008). These carotenoids are concentrated within the macula luteal region of the retina, as well as the retinal depression called the fovea. MPs are potent antioxidants and are thought to protect the retina against oxidative stress in response to AMD. A variety of methods have been used to assess MP in the human retina, of which resonance Raman imaging (RRI) is a developed *in vivo* method(Bernstein, Yoshida et al. 1998; Gellermann and Bernstein 2004). MP carotenoids are stereoisomers, each containing long conjugated polyene chains, thereby giving rise to a prominent C=C stretching Stokes Raman band around 1524 cm^{-1}, which can be used to measure MP concentrations in human retina and has been validated against chromatographic methods using model systems, such as excised human donor eyecups(Sharifzadeh, Zhao et al. 2008).

Glaucoma is a chronic neurodegenerative disease characterized by apoptosis of retinal ganglion cells (RGCs) and subsequent loss of visual function. Several factors can put you at increased risk for developing glaucoma, like elevated eye pressure, age, ethnic background, family history and certain medical conditions. The two main types of glaucoma are open-angle and angle-closure, which describe fluid drainage angles between the eye's cornea and iris. As a disease of progressive nature, glaucoma is not curable. The treatment of glaucoma, which reduce intraocular pressure by improving outflow of eye fluid or/and reducing its production, could only slow down the process. Early detection of glaucoma is critical for the prevention of permanent structural damage and irreversible vision loss. A series of eye exams are required to perform to diagnose glaucoma, like intraocular pressure measurement with "Tonometry", optic nerve damage test, visual field test, optic nerve imaging with optical coherence tomography(OCT), Heidelberg retinal tomography and so on. Unfortunately, a significant loss of RGCs can occur before any of the current tests show an abnormality. Namely, between 25 to 35% of the RGCs could be lost before any visual field defect is detectable(Kerrigan–Baumrind, Quigley et al. 2000). Although OCT, a modern promising noncontact and noninvasive tool for the accurate and objective anatomic diagnosis of glaucoma using low-coherence interferometry to provide high-resolution cross-sectional image, has the potential to detect optic nerve damage and atrophy much earlier than other used technology, it works for optically transparent tissues with diminished penetration through retinal/subretinal hemorrhage and pupil diameter larger than 4 mm. As a result, the detection and monitoring of progressive changes in glaucoma is demanding at its early stages, before vision loss occurs.

Raman spectroscopy, which measures the inelastic scattering of laser light by biomolecules in the tissue samples to predict the general biochemical composition of biological samples, can be used to provide rapid characterization of healthy versus diseased tissues in a nondestructive and noninvasive fashion. Tim C. Lei and his co-workers at University of Colorado Denver image the human trabecular meshwork (TM) using non-invasive, non-destructive coherent anti-stokes Raman scattering(CARS) without the application of exogenous label(Lei, Ammar et al. 2011). The CARS technique uses two laser frequencies to specifically excite carbon-hydrogen bonds, allowing the visualization of lipid-rich cell membranes. It was shown that CARS techniques were successful in imaging live TM cells in freshly isolated human TM samples, which represents a new avenue for exploring details of aqueous outflow and TM cell physiology. This technique may be used to help elucidate mechanisms of aqueous outflow through the conventional outflow system of the eye and to quantify the effects of TM cell number and distribution on the glaucomatous disease process. CARS is one of Raman spectroscopy technique, but unlike spontaneous Raman spectroscopy, it employs multiple photons to address the molecular vibrations, and produces a signal in which the emitted waves are coherent with one another. As a result, although CARS is orders of magnitude stronger than spontaneous Raman emission, nonresonant background and autofluorescence from the sample may overwhelm the CARS signal.

By now, the important concerns on future clinical application of Raman spectroscopy for glaucoma early diagnosis include: 1. Can Raman spectroscopy be used for early detection of molecular changes in glaucomatous retina tissue? 2. How to improve the spectra quality under the laser safety standards for *in vivo* measurement, like increasing the Raman signal

and reducing strong fluorescence background. 3. How to develop a working Raman imaging system with fiber optic probe that allows *in vivo* and remote Raman imaging of the retina in whole eye which is also a complex optical system.

1.1.2.4 General application in agriculture systems

Agricultural products and foods are essential to life and are also important to the world economy. With the increasing demand for a high quality life, quality and safety control of agricultural and food products are gaining the attention of the public as well as researchers. Variety of techniques has been employed for the characterization of the agricultural products and food. Traditional methods such as Gas Chromatography (GC)(Plutowska, Chmiel et al. 2011), High-Performance Liquid Chromatography (HPLC)(Zhang, Wong et al. 2011; Sun, Chen et al. 2012), and Gas Chromatography-Mass Spectrometry (GC-MS)(Kim, Ha et al. 2011) are all powerful tools for ingredient quantification and composition determination, but they are time consuming, and require skilled operators to carry out the analysis. Near-infrared spectroscopy (NIR) (Todorova, Atanassova et al. 2011; Hernández-Hierro, Valverde et al. 2012; Mulbry, Reeves et al. 2012) is another method widely used to monitor and assess composition and quality of products in food industry. But it shows low spectral resolution and is susceptible to interference from water due to the very strong infrared absorption of water molecules. Fluorescence spectroscopy is a very sensitive tool to provide information about molecules and their environment in food samples (Sahar, Boubellouta et al. 2011); however, it is limited to fluorescent samples. In contrast, due to its narrow and highly resolved bands, Raman spectroscopy allows for nondestructive extraction of chemical and molecular structural information about samples, and can be applied in rapid on-line analysis without any special sample preparation. Raman spectroscopy has been gaining popularity as

an analytical tool for agricultural products. Applications of Raman spectroscopy have been explored in various fields of agricultural products and food, including fruits (Liu and Liu 2011; Esser, Schnorr et al. 2012), vegetables(Nikbakht, Hashjin et al. 2011), crops(Shih, Lupoi et al. 2011; Schulmerich, Walsh et al. 2012), meat(Wang, Lonergan et al. 2012), dairy products(Meisel, Stöckel et al. 2011), coffee(El-Abassy, Donfack et al. 2011), oil(Samyn, Van Nieuwkerke et al. 2012), as well as beverages(Delfino, Camerlingo et al. 2011). In a recent study, Raman spectroscopy has been utilized in analysis of low concentration organic contaminants, like pesticide residue, on apples' surface(Li, Sun et al. 2012).

1.1.2.5 Application in muscle food quality evaluation and its limitation

Raman spectroscopy has been employed for detailed characterization of the microstructure of animal tissues, including applications relating lipid deposition in tissue to human health and linking protein structure to texture and tenderness. Predictions drawn from spectroscopic data have been compared to that from different traditional assays for protein solubility, apparent viscosity water holding capacity, dimethyl amine content, peroxide values and fatty acid composition, as well as instrumental texture methods commonly used to determine quality in fish and meat muscle treated under different conditions of handling, processing and storage (Herrero 2008). It has been shown that Raman spectroscopic data could be used to evaluate muscle food quality. In addition, Raman spectroscopy offers structural information about complex solid systems such as muscle food proteins and lipids (Yang and Ying 2011), which could be applied to study changes in the protein structure during the elaboration of muscle food products(Herrero 2008; Wang, Lonergan et al. 2012).

But just as with every technique, Raman has its limitations. One is that it is a relatively weak phenomenon because the effect is based on inelastic scattering of photons. On average about one out of one million scattered photons is inelastic Raman photon. Because the Raman effect is many orders of magnitude less intense than fluorescence, fluorescence from even trace impurities will overwhelm the Raman signal. To reduce fluorescence background, near IR excitation lasers have often been used for Raman spectroscopic measurements of biological samples. Near IR excitation photons can minimize both sample damage and fluorescence background, combining it with the use of a sensitive CCD camera; it is possible to obtain dispersive Raman spectra of most biological analytes with high sensitivity. Furthermore, spectra pre-processing techniques are necessary to reduce the effect of spectral artifacts such as varying background noises and intensity fluctuations(Schulze, Jirasek et al. 2005; Beier and Berger 2009). Data mining is sometimes necessary to be implemented to find delicate differences between groups, and to realize the full potential of Raman technique(Wang, Grozdanic et al. 2011).

1.1.3   Raman spectra pre-processing

1.1.3.1 Baseline correction

One of the challenges of using Raman spectroscopy for biological applications is the inherent fluorescence generated by many biological molecules that underlies the measured spectra. This fluorescence can sometimes be several orders of magnitude more intense than the weak Raman scatter, and its presence must be minimized in order to resolve and analyze the Raman spectrum. Using near infrared excitation (e.g., 785nm) can significantly reduce sample fluorescence (i.e., auto-fluorescence). However, most biological samples still exhibit some fluorescence, even with 785nm excitation. Furthermore, NIR excitation (longer λ) is

not always desirable, since the Raman intensity is proportional to $1/\lambda^4$. With NIR excitation, the Raman intensity of a given sample is much lower than what is achievable with shorter wavelength excitation lasers. As a result, subtracting background fluorescence from the raw spectrum is necessary to obtain a more interpretable signal. Traditionally, baseline correction is done manually. However, for high throughput Raman examination or Raman imaging, it is easy to end up with tens of thousands of Raman spectra. Due to the ultra large volume of data, manual baseline correction is simply not feasible. What is required is an automated baseline correction algorithm.

There are several available baseline correction approaches with different theoretical underpinnings(Lieber and Mahadevan-Jansen 2003; Schulze, Jirasek et al. 2005), such as wavelength shifting(Barclay, Bonner et al. 1997; Cai, Zhang et al. 2001), frequency-domain filtering(Mosier-Boss, Lieberman et al. 1995), first- and second- order derivatives(Zhang and Ben-Amotz 2000; O'Grady, Dennis et al. 2001), and simple curve sifting of the broadband variation with a high-order polynomial(Brennan, Wang et al. 1997; Mahadevan-Jansen, Mitchell et al. 1998; Vickers, Wambles et al. 2001). Though each of these methods has been shown to be useful in certain situations, they are not without limitations. Differentiation is an unbiased and efficient method for fluorescence subtraction, yet this method severely distorts Raman line shapes and relies on complex mathematical fitting algorithms to reproduce a traditional spectral form(Mosier-Boss, Lieberman et al. 1995). Frequency-based techniques can under- or over-filter, or cause artifacts to be generated in the processed spectra if the frequency elements of the Raman and noise features are not well separated(Mosier-Boss, Lieberman et al. 1995). Wavelet trans-formation is highly dependent on the decomposition method used and the shape of the fluorescence background(Barclay, Bonner et al. 1997).

Of these, polynomial curve-fitting has a distinct advantage over other fluorescence reduction techniques in its ability to retain the spectral contours and intensities of the input Raman spectra, yet most published records rely on sample-dependent user intervention for assignment of "non-Raman" locations on which to fit the curve. Unfortunately, this subjective user-selected intervention is time-consuming and is prone to variability. To address these limitations, the modified polyfit method for fluorescence subtraction was developed in this study. This method smoothes the spectrum in such a way that Raman peaks are automatically eliminated, leaving only the baseline fluorescence intact, to be subtracted from the raw spectrum (Figure 1.4). The basis for this method is a least-squares-based polynomial curve-fitting function. However, to eliminate the Raman bands from the fit, this function is modified such that all data points in the generated curve that have an intensity value higher than their respective pixel value in the input spectrum are automatically reassigned to the original intensity. This process (curve fitting and subsequent reassignment) is repeated to gradually eliminate the higher-frequency Raman peaks from the underlying baseline fluorescence. The filtering process ceases when there are no longer any data points in the fit curve that require reassignment(all values equal to or less than respective smoothed spectrum intensities). The processed baseline spectrum is then subtracted from the raw spectrum to yield the Raman bands on a near-null baseline(Lieber and Mahadevan-Jansen 2003).
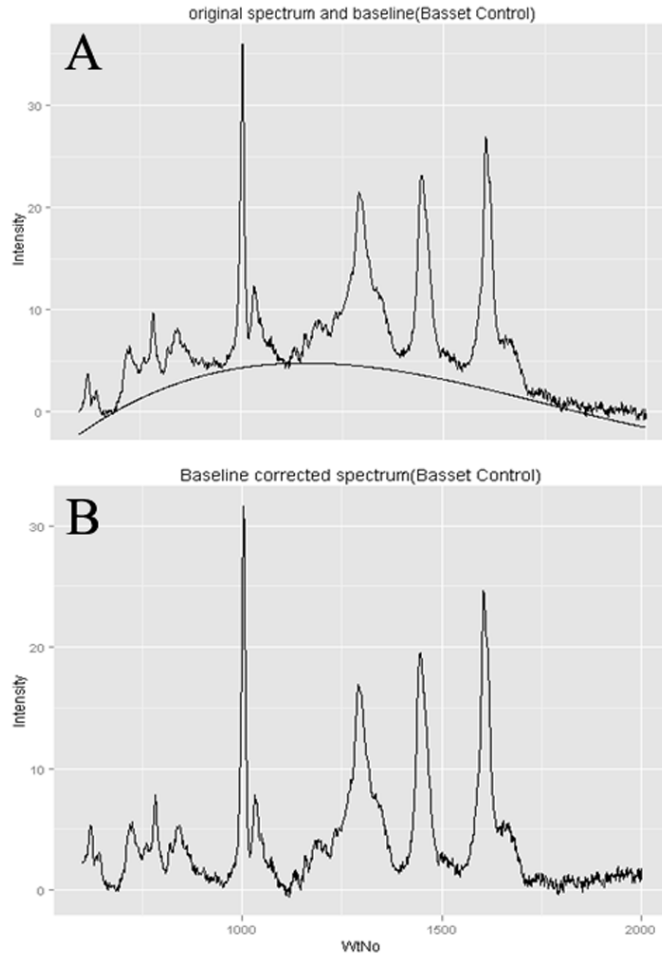
Figure 1.4 Baseline corrected spectrum

(A)Original spectrum which is measured from eye tissue section of a healthy basset hound and its final polynomial fitted baseline; (B) Its baseline corrected spectrum.

1.1.3.2 Smoothing

Another challenge in pre-processing is to capture important patterns in the spectra while removing noise or other fine-scale structures(Bocklitz, Walter et al. 2011). The usual approach is to smooth the spectral data. Various mathematical manipulation schemes are available to smooth the spectral data. Whatever smoothing technique is employed, the aim is to reduce the effects of random variations superimposed on the analytically useful signal. This transform can be simply expressed as: Spectrum (smoothed) = Spectrum (raw)-noise.

One of the most common algorithms for smoothing is the "moving average" which is used to analyze a sequence of data points by creating a series of averages of different subsets of the full data. Given a spectrum and a fixed odd subset size (wavenumber points), the moving average can be obtained by first taking the average of the first subset. The fixed subset size is then shifted forward, creating a new subset of numbers, which is averaged. This process is repeated over the entire data series to get a smoothed spectrum (Figure 1.5). As is shown in equation

$$SY_i = \frac{y_{(i-\frac{n}{2})} + \cdots + y_{(i-1)} + y_i + y_{(i+1)} + \cdots + y_{(i+\frac{n}{2})}}{n+1}$$

(n+1) is the subset size (number of the points), SY_i is i^{th} Raman intensity after smoothing. y_i is i^{th} raw Raman intensity. The center point in the window of a fixed odd number (n+1) of points is thereafter replaced by that calculated average. The primary factor controlling the extent of smoothing is the size of the window used for averaging. In general, the greater the size of the window is, the smoother the result is. Smoothing needs to be performed with caution. On one hand we want to smooth out noises to highlight the important Raman signatures, on the other hand we must avoid over-smoothing that may lead to loss of information.
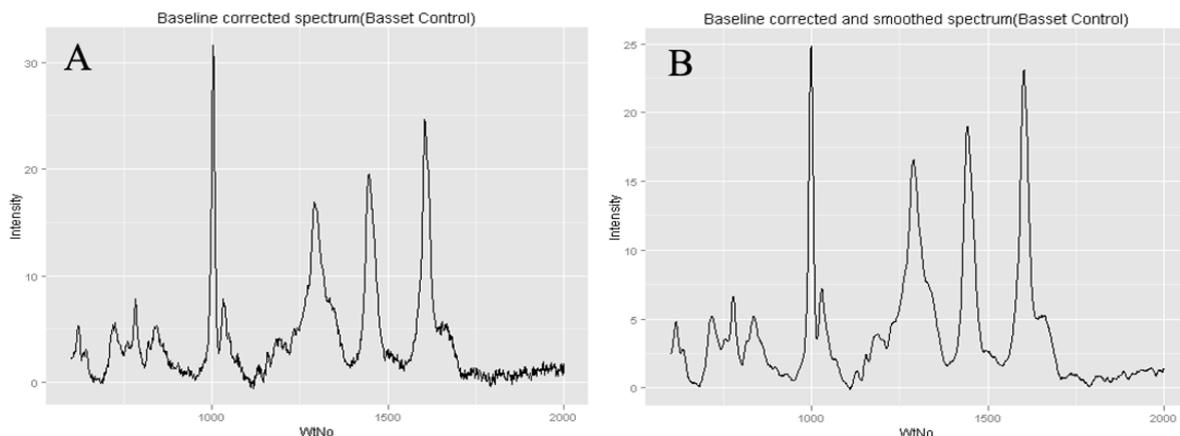
Figure 1.5 Smoothed spectrum.
(A)Baseline corrected spectrum; (B) Smoothed spectrum by moving average method. Both of them are based on a spectrum measured from eye tissue section of a healthy basset hound.

1.1.3.3 Normalization

Another widely used pre-processing method is normalization, in which intensity values are rescaled for consistency(Bocklitz, Walter et al. 2011). It is frequently used as a pre-processing step in preparing reference spectra for a qualitative identification library. Standard spectra of analytes with different concentrations or composition can be generated to confirm characteristic Raman shifts and peak intensities or areas for quantitative evaluation. Available algorithms include maximum intensity normalization, spectra area normalization and specific peak area normalization (Figure 1.6):

(1) The peak height can be used to accurately quantify analyte concentration(Lin and Dence 1992) once it is confirmed to be proportional to analyte concentration. For the max intensity normalization method, the maximum intensity value of each spectrum is identified and then the whole spectrum is divided by the maximum value (Figure 1.6A), as is shown in equation

$$NY_i = \frac{y_i}{\max(\vec{y})},$$

NY_i is i[th] normalized Raman intensity, y_i is i[th] raw Raman intensity, $\vec{y}$ is the vector of all Raman intensity for that spectrum.

 (2) Peak area normalization is generally preferred because background noise can be averaged throughout the width of the peak; thus, the noise has less impact on the data. For specific peak area normalization, only the area of peaks in the specific range is calculated, for example the Amide I region 1550-1650cm[-1](Figure 1.6B), and then the whole spectrum is divided by that area and recalibrate by multiplying its range of the wavenumber, as is shown in equation

$$NY_i = \frac{y_i \times (\max(\vec{x}) - \min(\vec{x}))}{\iint_{k=1550}^{1650} dy_k dx_k}.$$

 (3) For the spectra area normalization method, the content of all chemicals are considered as the same and their composition could be examined after the entire spectral area is normalized. All Raman intensities in the entire spectrum is divided by the area of all peaks in that spectrum and recalibrated by multiplying its range of the wave number (Figure 1.6C), as is shown in equation

$$NY_i = \frac{y_i \times (\max(\vec{x}) - \min(\vec{x}))}{\iint_{k=1}^{\infty} dy_k dx_k},$$

$\vec{x}$ is the vector of all wavenumber for that spectrum.
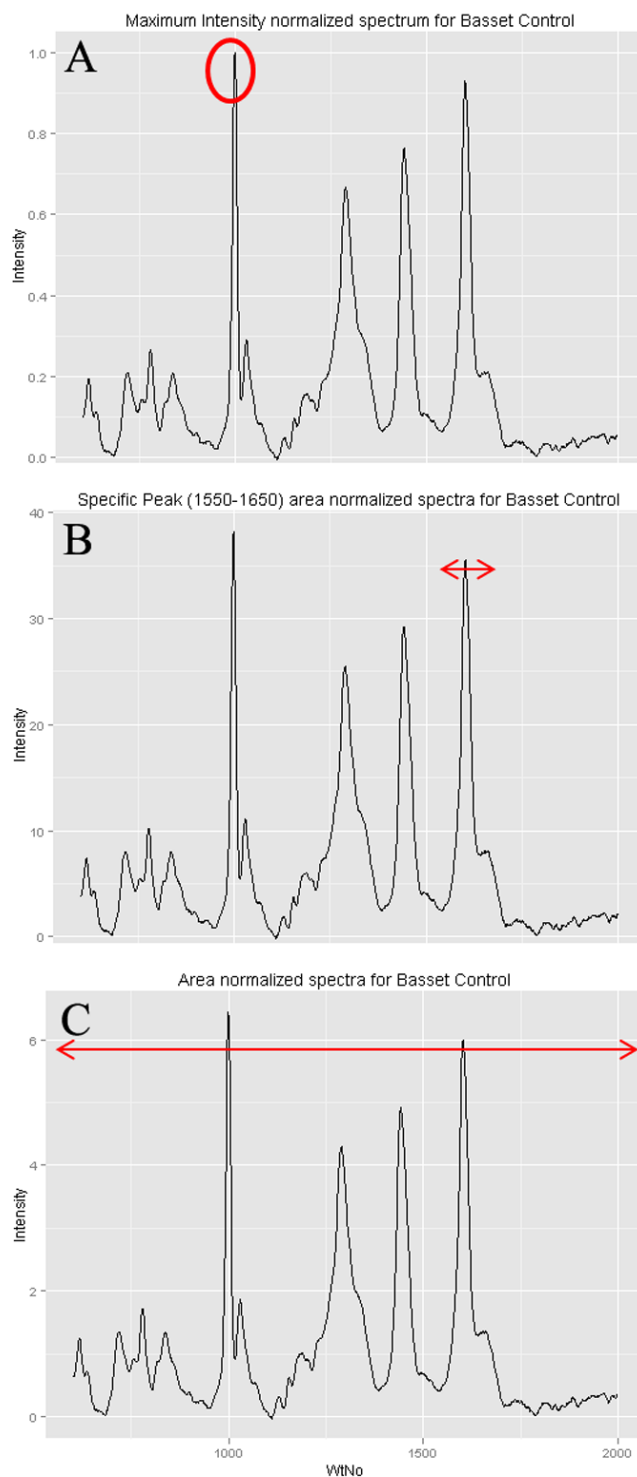
Figure 1.6 Normalization strategies.

(A)Maximum intensity normalized spectrum; (B) Specific peak area (1550-1650cm^{-1}) normalized spectrum; (C) Area normalized spectrum. All of them are based on one same spectrum measured from eye tissue section of a healthy basset hound.

1.1.3.4 Statistic spectra

Statistic spectra can be generated for extracting or displaying useful information from a group of spectra (Figure 1.7). An average spectrum is a spectrum in which Raman intensity at each wavenumber is averaged from Raman intensities of all the spectra in a category (for example, one group or replicated measurements for one sample) at the same wavenumber. The average spectrum of a sample could keep the most important characteristic features unique to this sample (Figure 1.7A). A range spectrum tells that the difference between the highest and the lowest intensity at any given wavenumber in the group (Figure 1.7B). A standard deviation spectrum shows how much variation or "dispersion" there is from the average spectrum in the group (Figure 1.7C).

A difference spectrum is a spectrum that is the result of subtracting all the signal channels of one spectrum from another, usually calculated from average spectra of different groups (Figure 1.7D). Differences can be defined from specific Raman bands that change, or from a fitting of biochemical components to the spectra. These changes can potentially be used as markers for classifying different groups.
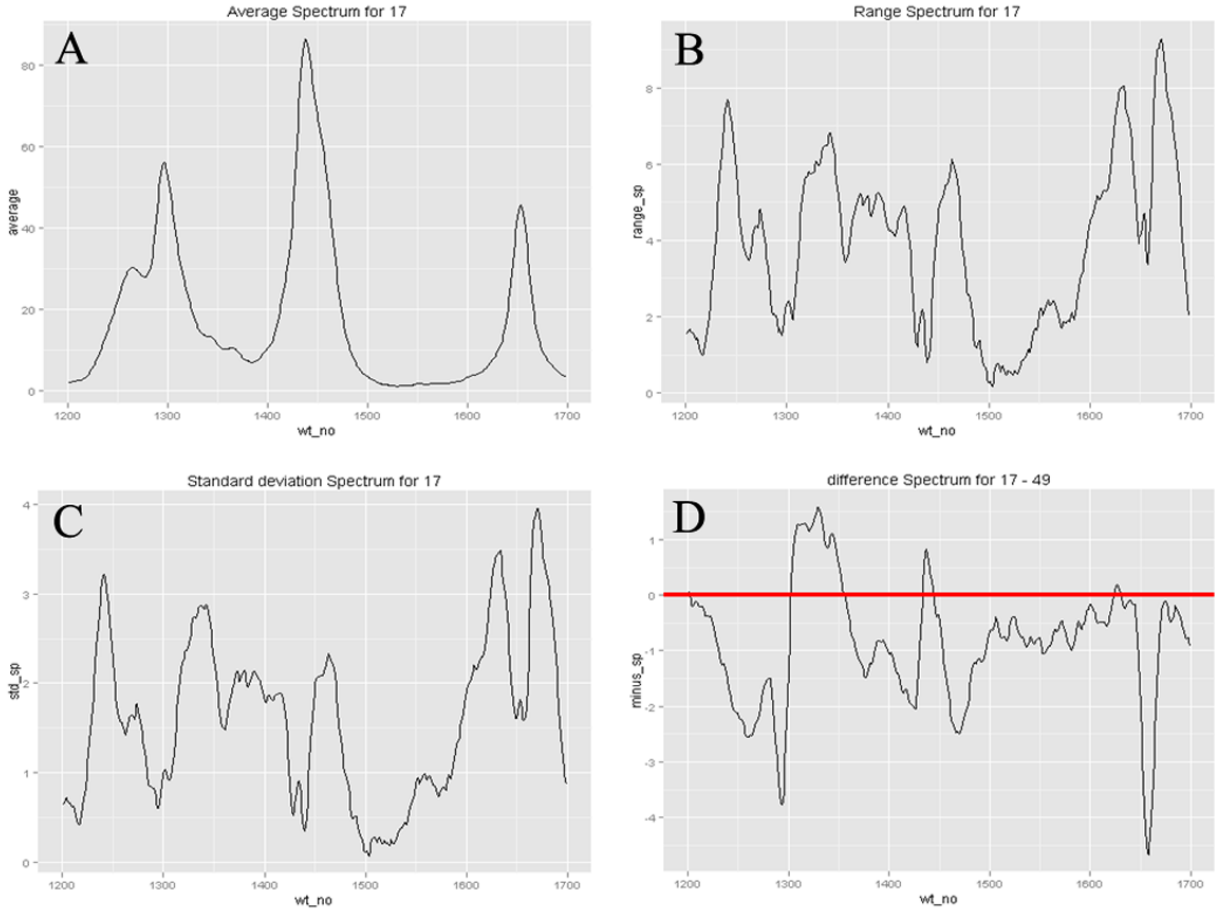
Figure 1.7 Statistic spectra.

All the statistic spectra are calculated from 10 measurements for pork fat sample "17" or/and "49". (A) Average spectrum; (B) Range spectrum; (C) Standard deviation spectrum; (D) Difference spectrum between average spectrum of pork fat "17" and "49".

1.1.3.5 Outlier removal

Spectra outlier diagnosis is a very important step to identify system faults in building reliable dataset. Proper procedures for elimination of outliers are valuable tools for improving the quality of spectral fitting. Outlying measurements with large systematic errors can be selectively eliminated, while those containing large random errors are retained during fitting. There is no rigid mathematical definition of what constitutes an outlier. Determining whether or not an observation is an outlier is ultimately a subjective exercise. Outliers, being

the most extreme observations, may include the sample maximum, or sample minimum, or both, depending on whether they are extremely high or low. However, the sample maximum and minimum are not always outliers because they may not be unusually far from other observations. At each wavenumber, the Raman intensities for all spectra could be considered as a vector, Usually at each wavenumber, if the Raman intensity is differ by three times the standard deviation or more from the mean, it will be considered as a outlier. After classifying measurements as outliers, these spectra are removed and the steps are reiterated with lower estimates of standard deviations as longs as outliers are found.

Also, interquartile range based method is used to detect spectral outliers in this study. This method is simple and easy to use, conceptually clear, and numerically stable. It is routinely used for the detection of multiple outliers in multivariate spectra data. The criteria for removing outliers are the spectra that had extreme observation and are applied to both calibration and prediction sets. If Q_1 and Q_3 are the lower and upper quartiles respectively at each wavenumber, then one could define an outlier outside the range $[Q_1-k(Q_3-Q_1), Q_3+k(Q_3-Q_1)]$ for some chosen constant k, which is selected through an optimization process.

1.1.3.6 Derivative spectrum

The concept of derivative spectral data was first introduced in the 1950s and became generally practicable in the late 1970s due to the introduction of microcomputers. In spectroscopic data processing, first and second derivatives are routinely calculated to remove slowly varying background noises which otherwise would contribute non-essential variances to the subsequent qualitative analysis or for quantification. Furthermore, first and second derivatives may vary with greater amplitude than the primary spectral data. The more distinguishable derivatives are especially useful for separating out peaks of overlapping

bands. The significant disadvantage to the derivative technique is that the singal to noise ratio (SNR) becomes worse at progressively higher derivative orders. It yields good SNR only if the difference of noise levels at the endpoints of the interval is small enough to yield a noise equivalent calculation much smaller than the signal.

For Raman spectra, the derivative technique is becoming increasingly popular in analytical spectroscopy as a resolution enhancement technique, to facilitate the detection and location of wavenumbers of poorly resolved components of a complex spectrum, and as a background correction technique to reduce the effect of spectral background interferences in quantitative analysis. First derivative spectra $\frac{d\vec{y}}{d\vec{x}}$ avoid contributions from fluctuations in spectral background, but are still sensitive to Raman intensity fluctuations (Figure 1.8B). The signs of second derivative spectra $\frac{d^2\vec{y}}{d^2\vec{x}}$ which indicate the locations of peaks and valleys are found to be extremely robust in identifying features with minimal variability in replicated measurements (Figure 1.8C). In this work, derivative spectra are obtained by applying a derivative transformation using Savitzky-golay algorithm(Savitzky and Golay 1964) to the data of the original spectrum.

With derivative spectra, the unique Raman signatures that distinguish a sample from others can be amplified. Therefore, derivative spectra are often utilized in differentiation analysis.
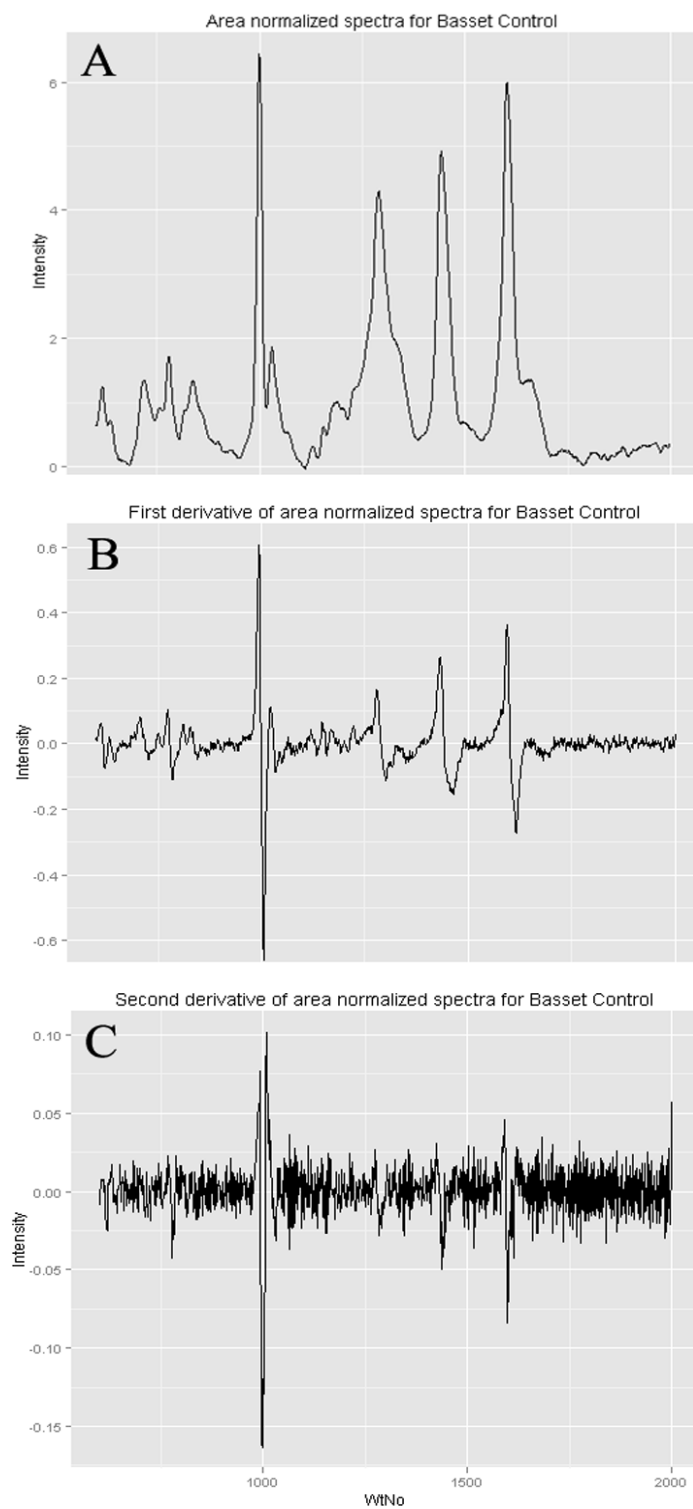
Figure 1.8 Derivative spectra.

(A)Baseline corrected, smoothed and area normalized spectrum from eye tissue section of a healthy basset hound; (B) First derivative spectrum; (C) Second derivative spectrum.

1.1.3.7 Binary spectrum

Raman peaks are represented by their wavenumber (Raman shift) and intensity. The peak intensities are dependent on many factors that may vary from sample to sample (i.e., sample size, exposure time, etc.), but their Raman shifts remain identical as long as the molecular makeup is the same. In analysis of biological samples, usually the most important spectral signatures are the fingerprinting Raman peaks that represent the biochemical landscape of the sample. Therefore, the binary bar-codes calculated from signs of second derivatives are developed to further remove the redundant information in the intensity fluctuation due to all the sources of intensity. The binary bar-code approach was originally proposed by Ziegler et al. to differentiate microorganisms based on their Raman spectroscopic signatures(Patel, Premasiri et al. 2008). The binary bar-codes were generated based on the second derivative spectra (Figure 1.9A), a binary value (0 or 1) was assigned to each second derivative spectral data point primarily based on the value of the second derivative, i.e., 1 for the absolute value lager than the threshold 0.05 of maximum absolute value of second derivative at this wavenumber and 0 for others (Figure 1.9B). As is shown in equation

$$BY_i = \begin{cases} 1 & abs(y_i) > threshold \times \max(abs(\vec{y})) \\ 0 & otherwise \end{cases},$$

BY_i is the ith intensity value in binary spectrum, $abs(y_i)$ is the ith absolute intensity value in raw spectrum.

Contribution to the measured spectra from low level background noises was thus removed by assigning 0 to it. Remaining 1s represent contributions to the measured spectra from relevant characteristic components. The selection of a threshold is determined through

28

investigation of the optimal threshold value that would yield the best classification accuracy. This threshold value helps to discriminate against residual noise components.
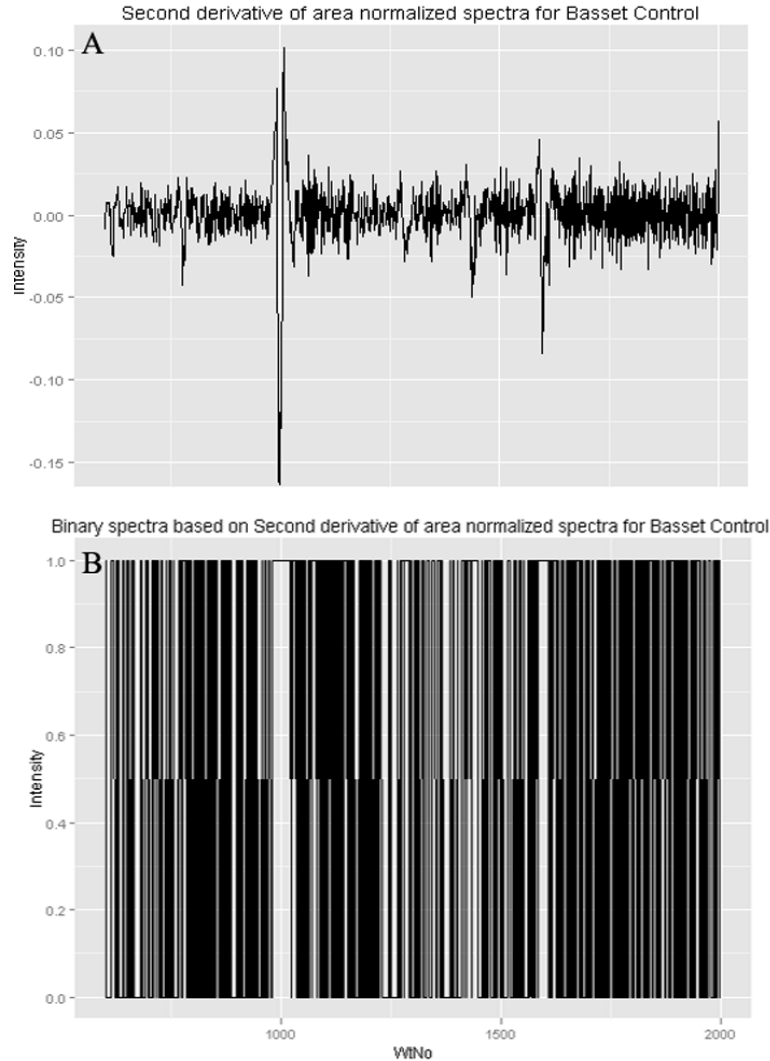
Figure 1.9 Binary spectrum.

(A)Second derivative from a baseline corrected, smoothed and area normalized spectrum from eye tissue section of a healthy basset hound; (B) Binary spectrum calculated from the second derivative spectrum with threshold 0.05 of the maximum value.

1.1.3.8 Standardized residual spectrum

A standardized residual spectrum (SRS) is sometimes calculated from the original spectral data to highlight the variations in spectral data measured from the same type of

samples (i.e., control versus diseased) (Figure 1.10B). The calculation of SRS includes mean centering and variance scaling. Mean centering is simply the subtraction of the mean Raman intensity at each Raman shift from each spectrum, which shifts the origin of coordinate system to the center of the dataset. The main reason for centering data is to prevent data points that are farther from the origin form exerting an undue amount of leverage over the points that are closer to the origin(Kramer 1998). Variance scaling is an adjustment to a data set that equalizes the variance of each variable(Kramer 1998). As is shown in equation

$$SRS(Raman\ shift\colon i\ ) = \frac{X(Raman\ shift\colon i) - \bar{X}(Raman\ shift\colon i)}{s.d.(Raman\ shift\colon i)},$$

SRS(Raman shift: i) is the standardized residual spectral intensity at Raman shift wavenumber i, X(Raman shift: i) is the Raman intensity of that spectrum at the same Raman shift i, $\bar{X}$ (Raman shift: i) is the mean Raman intensity of all spectra from the same data set (i.e., diseased or control) at the same Raman shift i, and s.d.(Raman shift) is the standard deviation of the Raman intensity within the data set at the same Raman shift i.

From the analytical chemistry point of view, variance scaling maps the data set into an abstract space whose axes no longer have any external physical or chemical significance. It also can reduce the influence of variables where the signal variation (and hence analytically useful information content) is large while increasing the influence of variables that contain mostly noise.
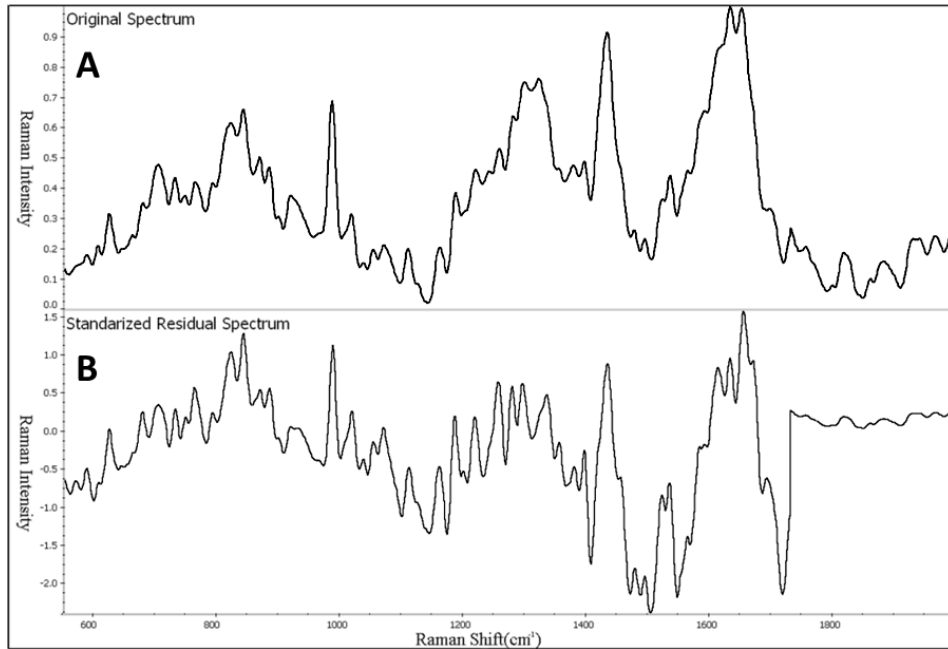
Figure 1.10 Standardized residual spectrum.

(A)One original spectrum for eye section of glaucomatous basset hound; (B) Its corresponding standardized residual spectrum for group glaucomatous basset hound.

1.1.4 Classification of samples based on spectral signatures

1.1.4.1 Data compression

From a mathematical standpoint, each wavenumber of a Raman spectrum represents a dimension or variable. Commonly, one Raman spectrum contains thousands of dimensions, which brings a great challenge for following statistical analysis. For discriminant analysis, as the dimensions of the data set become large, the limitation on the capability of detecting distinguishable classes becomes severe. Due to the fact that most statistical methods are based on optimization criteria, it is advisable to reduce the dimension of the problem. This dimension reduction results in decreasing computational costs and increasing probability of finding the best model representing the data. For this purpose, it is a common practice that Principal Component Analysis (PCA)(Rencher and Christensen 2012) is utilized to optimally

reduce the dimensionality of the data set without degrading it and with the added benefit of removing some noise.

PCA is mathematically defined as an orthogonal linear transformation that transforms the data to a new coordinate system such that the great variance by any projection of the data comes to lie on the first coordinate (called the first principal component), the second greatest variance on the second coordinate, and so on(Shaw 2003). As is shown in the equation $X = L \times S^T$, PCA summarizes the original X (the matrix of spectra, Raman intensities) into much fewer more informative variables called scores, S (score matrix). These new variables (or scores) are linearly weighted combination of the original X. The weighting profiles are called loadings L (matrix of loadings). For each score variable in S, the influence (weight) of the original spectra X is found in its corresponding loading profile L.

PCA is also the simplest of the true eigenvector-based multivariate analyses. Often, its operation can be thought of as revealing the internal structure of the data in a way that best explains the variance in the data(Jolliffe 2005). The objective of principal component analysis is to retain as much variation as possible while reducing the dimensionality of the dataset. This may identify new meaningful underlying variables that are linear combinations of the original variables. There are two methods to choose the number of components which are based on relations between the eigenvalues. The first is to plot the eigenvalues of the matrix XX^T, which are proportional to the portion of the variance. If the points on the graph tend to level out, these eigenvalues are usually close enough to zero that they can be ignored. The second method is to limit the number of components to that number that accounts for a certain fraction of the total variance, for example, 0.99. In this work, 10-50 PCs (account for

at least 99% of the total variance in the data) were usually selected from thousands dimensional spectral data as inputs for multivariate discriminant classification model.

1.1.4.2 Supervised machine learning

The world is overwhelmed with data. As the volume of data increases, inevitably, the proportion of what people understand decreases. Laying hidden in all these data is information, potentially useful information that is rarely made explicit or taken advantage of. This is also the situation for Raman spectral data, the nature of which is highly overlapped signals from different chemical features combined with a lot of correlated information. These features and the information can be difficult to extract using simplistic univariate statistical methods.

Supervised machine learning, which forms the core of what we call data mining, is the machine learning task of inferring a function from supervised (labeled) training data. The methods originated in statistics in the early nineteenth century. In 1936, Fisher's linear discriminant (Fisher 1936) determines a linear combination of the variables that separates two classes by comparing the differences between class means with the variance of values within each class. An increase in the number and size of databases in the late twentieth century has inspired a growing desire to extract knowledge from data, which has contributed to a recent burst of research on new methods, especially on algorithm development.

In supervised machine learning, each observation in training data is a pair consisting of an input object (typically a vector of variables) and a desired output value (also called the supervisory signal)(Figure 1.11). A supervised machine learning algorithm analyzes the training data and produces an inferred function, which is called a classifier (if the output is

discrete, i.e. group name, it is also called classification) or a regression function (if the output is continuous, called regression). The inferred function should predict the correct output value for any valid input object. This requires the learning algorithm to generalize from the training data to unseen situations in a "reasonable" way. The choice of specific learning algorithm is a critical step (Figure 1.11). Classical approaches and algorithms include linear discriminant analysis, quadratic discriminant analysis, artificial neural network, decision tree learning, random forests, Support Vector Machines (SVM), Bayesian networks, etc. Generally, SVMs and neural networks tend to perform better when dealing with multi-dimensional, continuous features(Kotsiantis, Zaharakis et al. 2007). The classifier's evaluation is most often based on prediction accuracy (the percentage of correct prediction divided by the total number of predictions). If the error rate evaluation is unsatisfactory, a previous stage of the supervised machine learning process needs to be returned to (Figure 1.11).
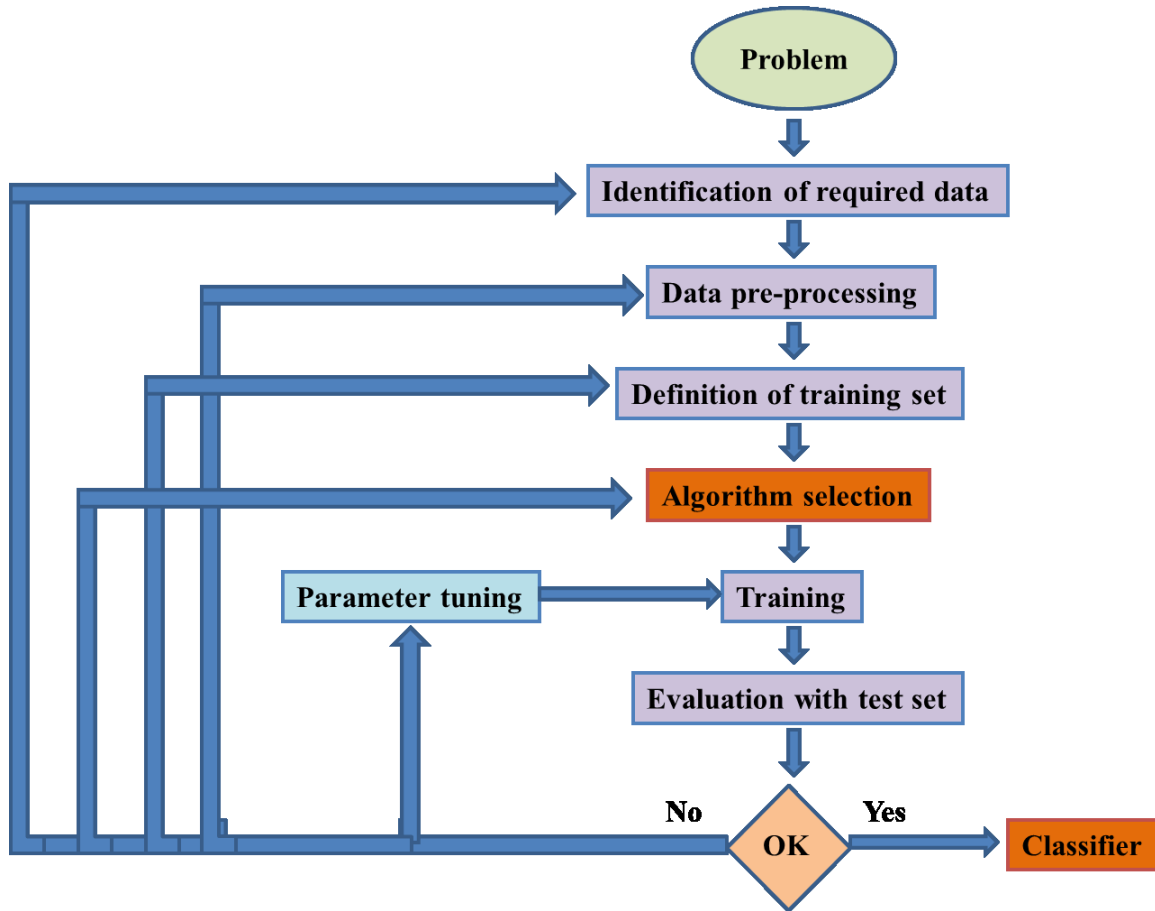
Figure 1.11 The process of supervised machine learning.

1.1.4.3 Support vector machines

Support vector machine (SVM) (Steinwart and Christmann 2008) belongs to a new generation of machine learning algorithm, originally introduced by Vapnik and co-workers(Boser, Guyon et al. 1992; Cortes and Vapnik 1995) and successively extended by recent advances in statistical learning theory for classification or regression. SVMs are currently among the best performers for classification and is an extension to nonlinear models of the generalized portrait algorithm developed by Vladimir Vapnik(Ben-Hur, Horn et al. 2002). Their remarkably robust performance with respect to sparse and noisy data is making them the system of choice in spectral analysis.

As a binary classification method, Support Vector Machine is particularly suitable to separate two distinguishable groups. In SVM, input labeled data from two classes are viewed as two sets of vectors in an n-dimensional space and the output are a model for classifying new unlabeled data into one of those two classes. SVM can generate linear and non-linear models. In the linear case, SVM algorithm will construct a separating hyper plane in that space, which maximizes the margin between the two data sets, the smallest distance between the decision boundary and any of the samples. Intuitively, a good separation is achieved by the hyper plane that has the largest distance to the neighboring data points of both classes, since in general larger the margin, better the classification. The SVM algorithm also assigns a weight to each input point, but most of these weighs are equal to zero. The points having non-zero weight are called support vectors and they can be bounded support vectors (if they take a maximum possible value C) or unbounded support vectors (if their absolute value is smaller than C). The separating hyper plane is defined as a weighted sum of supported vectors.

Application of linear decision boundaries is severely limited. Noisy training data often makes the training set non-separable in the feature space. Since 1995, significant improvements have been made to SVMs, especially when the kernel trick was incorporated in order to allow non-linear hyper planes. The general idea is that the original feature space can always be mapped to some higher-dimensional feature spaces where the training set is separable with non-linear transformation. The kernel is a function that returns the value of the dot product between the images of the two arguments, such as $k(x_i, x_j) = \varphi(x_i) \cdot \varphi(x_j)$. Choosing kernel probably is the trickiest part of using SVM. The kernel function should maximize the similarity among instances within a class while accentuating the differences

between classes. A variety of kernels have been proposed for different types of data. Examples of commonly used kernel functions are polynomial kernel, Gaussian or Radial-Basis Function (RBF) kernel and sigmoid kernel. In practice, a low degree polynomial kernel or RBF kernel with a reasonable width is a good initial try for data that live in a fixed dimensional input space.

1.1.4.4 Partial least square regression

Partial-least-squares regression (PLSR)(Abdi 2003) is a commonly used quantitative multivariate statistical tool that allows for the analysis of data with strong correlations and with noise(Wold, Sjöström et al. 2001) to model a response variable when there are a large number of predictor variables, known as PLS components, as linear combinations of the original predictor variables. Contrary to more general multiple linear regression model, PLSR can also handle data sets with more variables than samples. Hence, it is especially useful for Raman spectroscopic datasets that contain values at hundreds to thousands of wavenumbers. While originally developed for the field of chemometrics, PLSR has been applied to a number of spectroscopic studies in diverse applications fields such as vegetation studies(Asner and Martin 2008), soil mechanics(Yitagesu, van der Meer et al. 2009).

Partial-least-squares modeling can be applied as classification model or as multivariate calibration model. In this work, PLSR models were developed to link the Raman spectra to pork sensory data and used as a calibration tool. The PLSR creates a regression model that uses a set of predictor variables X (in this case the Raman spectra) to predict the occurrence and concentration of a set of response variables Y (in this case the pork sensory data). It calculates a linear relationship between two matrices which is shown in $Y = Q \times X + P$, where the matrices Q and P are the regression coefficients. If Y has only one column,

it can be interpreted as calculating the linear spectral response. Similar to a principal component analysis, the high dimensional X matrix is reduced to a few factors or latent variables by a projection to an orthogonal system of smaller dimensionality. The main difference being that in a PCA, the variance in X is maximized while in a PLSR the covariance between X and Y is maximized(Esbensen, Guyot et al. 2006). This causes the first few factors to contain the spectral content that is most representative and predictive of the Y values while higher number factors contain spectral content that is either not related to the particular predicted Y or contains noise.

In a first step, a PLSR model is built, using a training set of samples for which the spectral information as well as the response is known. In the second step, the resulting PLSR model is applied to new samples for which only spectra are available and the responses (like values of beef sensory parameters) are modeled from the corresponding Raman spectra, afterward the differences between the predicted values and the true values are calculated. The quality of a PLSR model is often measured by the mean-squared-error-of-prediction (MSEP) as the indicator for predictive power of the model, which is the mean over all squared value differences and reflects the averaged error rate.

1.1.4.5 Cross-validation and independent validation

Cross-validation is a common technique in modern multivariate statistics for assessing how the results of an analysis will generalize to an independent dataset(Browne 2000). One round of cross-validation involves partitioning a sample of data into complementary subsets, performing the analysis on one subset (called the training set), and validating the analysis on the other subset (called the validation set or testing set)(Figure 1.12A). To reduce variability and avoid overfitting of the models, multiple rounds of cross-

validation are performed using different partitions, and the validation results are averaged over the rounds(Witten, Frank et al. 2011). Averaging results over all cross-validation runs is useful and has an important influence over the error estimates (Figure 1.12A).

One inherent drawback of cross-validation comes from the fact that the validation set and the training set are indeed spectra measured from the same batch of samples (e.g., retinal tissues of the same dog). The high prediction accuracy reported from cross-validated discriminant models can be biased. In this study, to further confirm that Raman spectroscopic data can yield enough information that distinguishes diseased tissues from normal ones, even at an early stage of the disease, we tested the discriminant model by independent validation (Figure 1.12B). In this approach, the validation set only contains spectral data that were acquired from an independent set of samples (e.g., a different group of dogs) (Figure 1.12B), with no overlap with the sample pool from which the spectral data for the training of the discriminant model were acquired.
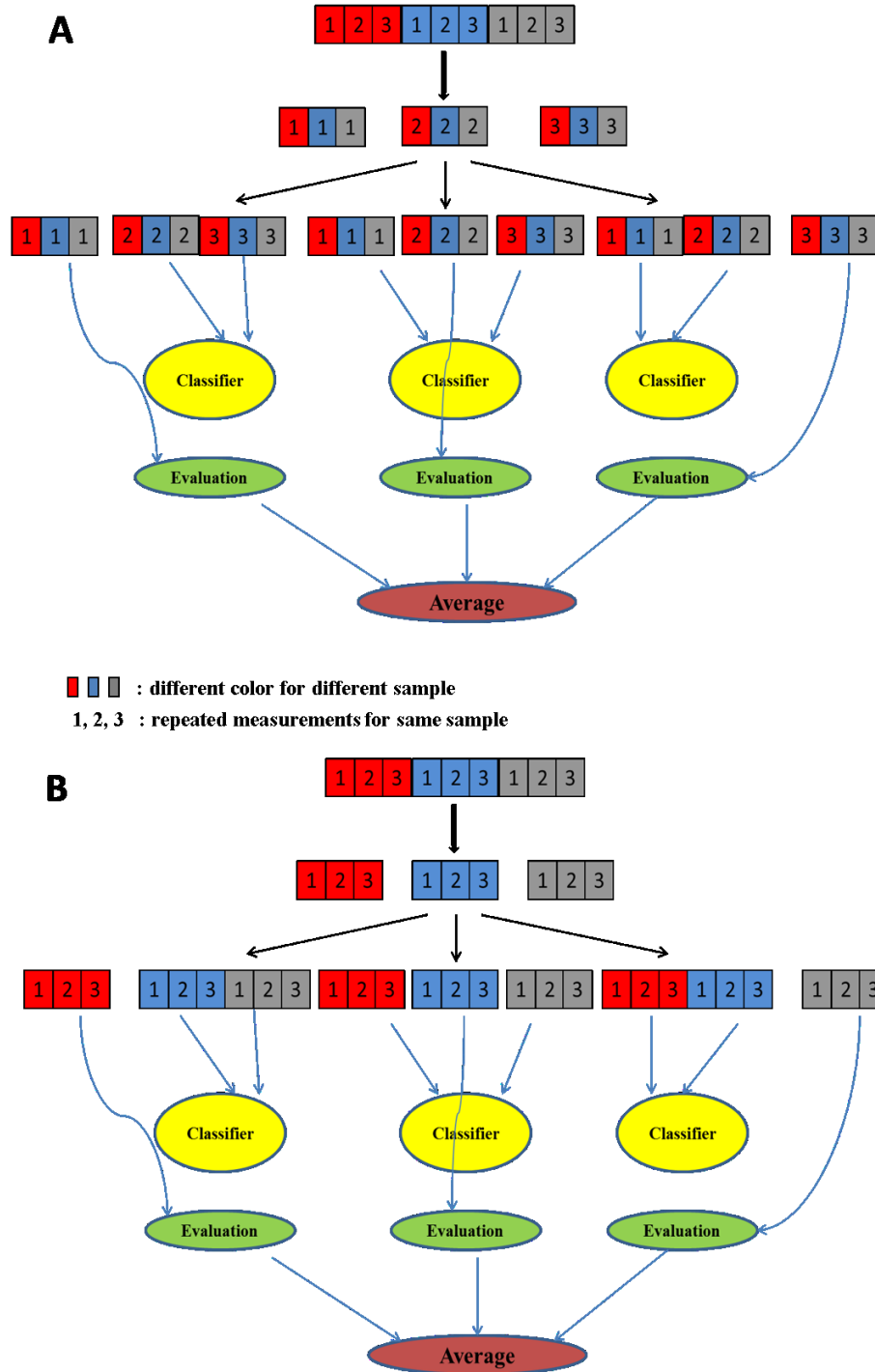
Figure 1.12 Cross-validation and independent validation.

Different color red, blue and grey blocks mean different samples. The number "1", "2", "3" stand for replicate measurements for same sample. (A) Cross-validation; (B) Independent validation.

1.1.4.6 "RSpec" package

  The "RSpec" package implements basic and classical Raman spectral pre-processing methods for raw spectra in R, such as polynomial baseline correction, maximum intensity normalization, area normalization, specific peak normalization, spectra statistics, outlier detection, moving average points smoothing, first and second derivative spectra calculation, binary spectra calculation, standardized residual spectra calculation. In addition, data analysis methods, such as principal component analysis, support vector machine, artificial neutral network, random forest and partial least squares regression, are included in this package (Figure 1.13). I developed the "RSpec" package primarily for this research. Nevertheless the RSpec package will be freely available from the Comprehensive R Archive Network (CRAN), licensed under the GNU General Public License (GPL).
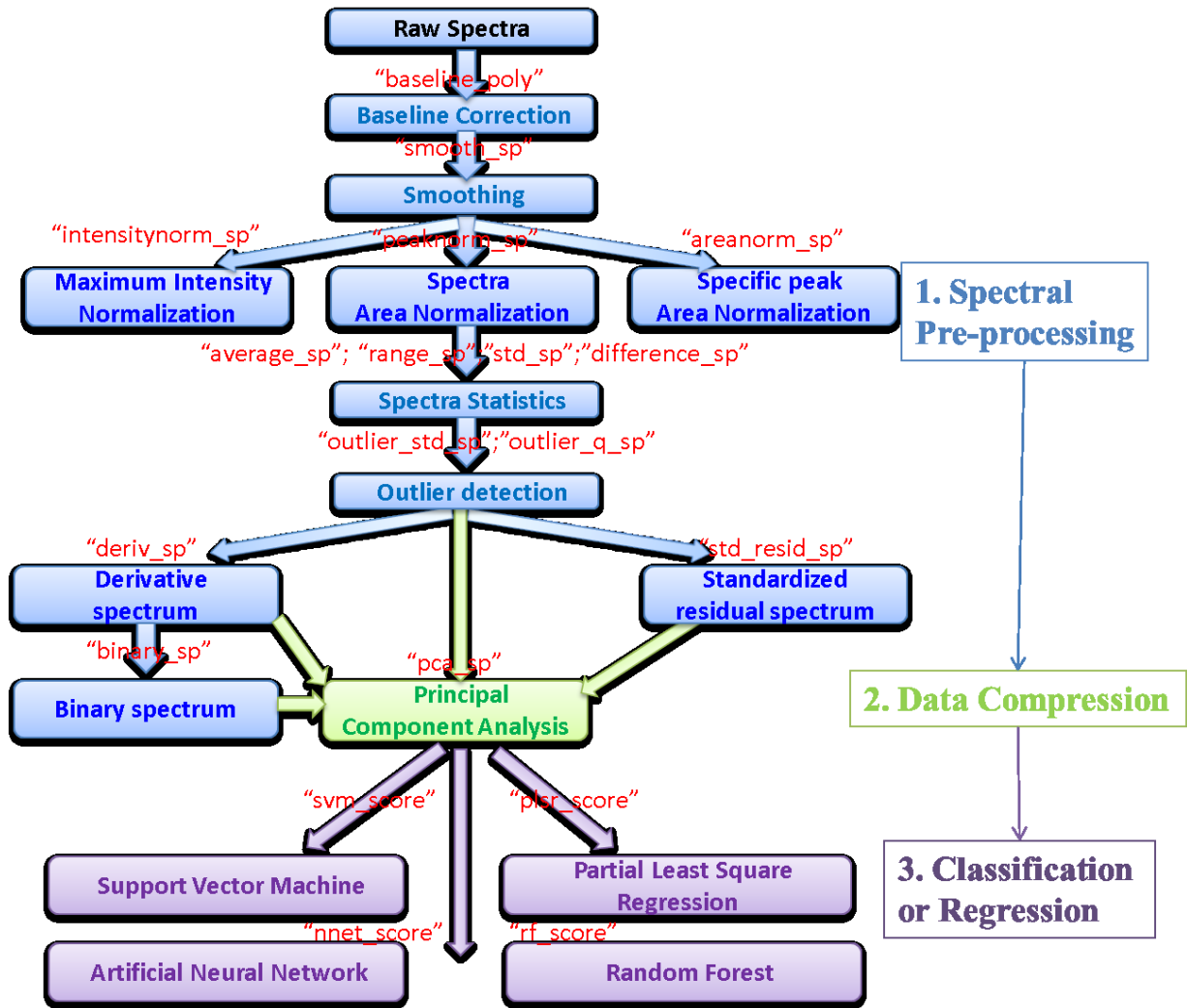
Figure 1.13 Flow chart of "RSpec"

1.2 Research Objectives

Research related to Raman spectroscopy has grown rapidly in the past decade due to the decreasing cost of Raman instruments, and the ever-expanding scope of Raman applications. Raman spectroscopy has many advantages compared to other analytical and detection techniques that make it quite appealing as a method of choice for biological samples. The overall objective of this research was to develop innovative applications of Raman spectroscopy to address important problems related to biomedical and agriculture systems. The specific objectives for each project are as follows:

1) To evaluate whether Raman spectroscopy can be used for detection of molecular changes in glaucomatous retinal tissues at different stages of the disease, with the ultimate goal of developing imaging routines which can detect early onset and progression of glaucoma based on changes in tissue biochemical composition.

2) To evaluate and predict tenderness, juiciness and chewiness of fresh, uncooked pork loins based on their Raman spectral features, and to develop a rapid objective assay of pork sensory attributes for practical applications in pork industry.

3) To evaluate the potential of Raman spectroscopy as an innovative rapid method for in-field/onsite evaluation of boar taint in male pig carcasses in slaughterhouses.

1.3 Dissertation Overview

This dissertation contains two main parts: exploring Raman spectroscopy in evaluation of glaucomatous and glaucoma-like retinal changes (Chapter 2, 3) and rapid pork sensory quality determination and boar taint evaluation using Raman spectroscopy (Chapter 4, 5). In chapter 1, a general introduction to the research is presented. In chapter 2, Raman spectroscopy was applied to differentiate and classify differences between glaucomatous and healthy (control) retinal ganglion cells (RGCs) of canine retinal tissues. Chapter 3 shows that Raman spectroscopic screening can potentially become a powerful tool for detection and characterization of early stages of the disease, in which independent cross-validation is utilized to provide more reliable results. In chapter 4, partial least square regression models were developed to predicate the value of sensory tenderness, chewiness and juiciness based on Raman spectroscopic characteristics of pork loins. A new Raman spectroscopic binary barcoding model was created to classify pork loins into grades by sensory tenderness and chewiness. Raman spectroscopy was found to have the potential to become a rapid objective

assay for tenderness and chewiness of pork products that may find practical applications in pork industry. In chapter 5, high classification accuracies, above 90% for raw pork fat and above 95% based on methanol extraction method, demonstrated that Raman spectroscopy offers a rapid, efficient and relatively accurate detection method for boar taint (i.e., androstenone and skatole). In the last chapter, chapter 6, a general conclusion of the research work is presented and recommendations for future work are suggested.

1.4 References

Abdi, H. (2003). Encyclopedia for Research Methods for the Social Sciences: Partial Least Squares Regression (PLS-Regression). Thousand Oaks, CA, USA, Sage Press.

Asner, G. P. and R. E. Martin (2008). "Spectral and chemical analysis of tropical forests: Scaling from leaf to canopy levels." Remote Sensing of Environment 112(10): 3958-3970.

Barclay, V. J., R. F. Bonner, et al. (1997). "Application of wavelet transforms to experimental spectra: Smoothing, denoising, and data set compression." Analytical Chemistry 69(1): 78-90.

Bauer, N., J. P. Wicksted, et al. (1998). "Noninvasive assessment of the hydration gradient across the cornea using confocal Raman spectroscopy." Investigative Ophthalmology & Visual Science 39(5): 831-835.

Bauer, N. J. C., F. Hendrikse, et al. (1999). "In vivo confocal Raman spectroscopy of the human cornea." Cornea 18(4): 483-488.

Beier, B. D. and A. J. Berger (2009). "Method for automated background subtraction from Raman spectra containing known contaminants." Analyst 134(6): 1198-1202.

Bellot-Gurlet, L., S. Pagès-Camagna, et al. (2006). "Raman spectroscopy in art and archaeology." Journal of Raman Spectroscopy 37(10): 962-965.

Ben-Hur, A., D. Horn, et al. (2002). "Support vector clustering." The Journal of Machine Learning Research 2: 125-137.

Bernstein, P. S., M. D. Yoshida, et al. (1998). "Raman detection of macular carotenoid pigments in intact human retina." Investigative Ophthalmology & Visual Science 39(11): 2003-2011.

Bocklitz, T., A. Walter, et al. (2011). "How to pre-process Raman spectra for reliable and stable models?" Analytica Chimica Acta 704(1-2): 47-56.

Boser, B. E., I. M. Guyon, et al. (1992). <u>A Training Algorithm for Optimal Margin Classifiers</u>. ACM, Mont Saint-Michel, France.

Braiman, M. S. (2006). <u>Vibrational Spectroscopy of Biological and Polymeric Materials</u>. Boca Raton, FL, USA, CRC Press.

Brennan, J. F., Y. Wang, et al. (1997). "Near-Infrared Raman spectrometer systems for human tissue studies." <u>Applied Spectroscopy</u> **51**(2): 201-208.

Browne, M. W. (2000). "Cross-validation methods." <u>Journal of Mathematical Psychology</u> **44**(1): 108-132.

Brożek-Płuska, B., I. Placek, et al. (2008). "Breast cancer diagnostics by Raman spectroscopy." <u>Journal of Molecular Liquids</u> **141**(3): 145-148.

Cai, T. T., D. Zhang, et al. (2001). "Enhanced chemical classification of Raman images using multiresolution wavelet transformation." <u>Applied Spectroscopy</u> **55**(9): 1124-1130.

Chen, K. H., W. T. Cheng, et al. (2005). "Calcification of senile cataractous lens determined by Fourier Transform Infrared (FTIR) and Raman Microspectroscopies." <u>Journal of Microscopy</u> **219**(1): 36-41.

Chowdary, M., K. K. Kumar, et al. (2006). "Discrimination of normal, benign, and malignant breast tissues by Raman spectroscopy." <u>Biopolymers</u> **83**(5): 556-569.

Cortes, C. and V. Vapnik (1995). "Support-vector networks." <u>Machine Learning</u> **20**(3): 273-297.

De Gelder, J., K. De Gussem, et al. (2007). "Reference database of Raman spectra of biological molecules." <u>Journal of Raman Spectroscopy</u> **38**(9): 1133-1147.

De Jong, B. W. D., T. C. B. Schut, et al. (2006). "Discrimination between nontumor bladder tissue and tumor by Raman spectroscopy." <u>Analytical Chemistry</u> **78**(22): 7761-7769.

Delfino, I., C. Camerlingo, et al. (2011). "Visible micro-Raman spectroscopy for determining glucose content in beverage industry." <u>Food Chemistry</u> **127**(2): 735-742.

Demtröder, W. (2003). <u>Laser Spectroscopy: Basic Concepts and Instrumentation</u>. New York, NY, USA, Springer Verlag.

El-Abassy, R. M., P. Donfack, et al. (2011). "Discrimination between Arabica and Robusta green coffee using visible micro Raman spectroscopy and chemometric analysis." <u>Food Chemistry</u> **126**(3): 1443-1448.

Erckens, R., F. Jongsma, et al. (2001). "Raman spectroscopy in ophthalmology: From experimental tool to applications *in vivo*." <u>Lasers in Medical Science</u> **16**(4): 236-252.

Erckens, R. J., M. Motamedi, et al. (1997). "Raman spectroscopy for non-invasive characterization of ocular tissue: Potential for detection of biological molecules." Journal of Raman Spectroscopy **28**(5): 293-299.

Esbensen, K. H., D. Guyot, et al. (2006). Multivariate Data Analysis In Practice: An Introduction to Multivariate Data Analysis and Experimental Design. Camo, Oslo.

Esser, B., J. M. Schnorr, et al. (2012). "Selective detection of ethylene gas using carbon nanotube based devices: Utility in determination of fruit ripeness." Angewandte Chemie International Edition **51**(23): 5752-5756.

Fisher, R. (1936). "Linear discriminant analysis." Annals of Eugenics **7**: 179-188.

Frank, C. J., R. L. McCreery, et al. (1995). "Raman spectroscopy of normal and diseased human breast tissues." Analytical Chemistry **67**(5): 777-783.

Frost, R. L., R. A. Wills, et al. (2005). "Comparison of the Raman spectra of natural and synthetic K⁻ and Na⁻ jarosites at 298 and 77 K." Journal of Raman Spectroscopy **36**(5): 435-444.

Gellermann, W. and P. S. Bernstein (2004). "Noninvasive detection of macular pigments in the human eye." Journal of Biomedical Optics **9**(1): 75-85.

Haka, A. S., K. E. Shafer-Peltier, et al. (2005). "Diagnosing breast cancer by using Raman spectroscopy." Proceedings of the National Academy of Sciences of the United States of America **102**(35): 12371.

Hata, T. R., T. A. Scholz, et al. (2000). "Non-invasive Raman spectroscopic detection of carotenoids in human skin." Journal of Investigative Dermatology **115**(3): 441-448.

Hernández-Hierro, J. M., J. Valverde, et al. (2012). "Feasibility study on the use of visible-near Infrared spectroscopy for the screening of individual and total glucosinolate contents in broccoli." Journal of Agricultural and Food Chemistry **60**(30): 7352-7358.

Herrero, A. M. (2008). "Raman spectroscopy a promising technique for quality assessment of meat and fish: A review." Food Chemistry **107**(4): 1642-1651.

Herrero, A. M. (2008). "Raman spectroscopy for monitoring protein structure in muscle food systems." Critical Reviews in Food Science and Nutrition **48**(6): 512-523.

Ingle Jr, J. D. and S. R. Crouch (1988). Spectrochemical Analysis. Old Tappan, NJ, USA, Prentice Hall College Book Division.

Jolliffe, I. (2005). Principal component analysis, Wiley Online Library.

Katz, A., E. F. Kruger, et al. (2003). "Detection of glutamate in the eye by Raman spectroscopy." Journal of Biomedical Optics **8**(2): 167.

Kendall, C., N. Stone, et al. (2003). "Raman spectroscopy: A potential tool for the objective identification and classification of neoplasia in Barrett's oesophagus." The Journal of Pathology **200**(5): 602-609.

Kerrigan–Baumrind, L. A., H. A. Quigley, et al. (2000). "Number of ganglion cells in glaucoma eyes compared with threshold visual field tests in the same persons." Investigative Ophthalmology & Visual Science **41**(3): 741-748.

Kiefer, W. (2007). "Recent advances in linear and nonlinear Raman spectroscopy I." Journal of Raman Spectroscopy **38**(12): 1538-1553.

Kim, J. K., S. H. Ha, et al. (2011). "Determination of lipophilic compounds in genetically modified rice using Gas Chromatography time of flight Mass spectrometry." Journal of Food Composition and Analysis **25**(1): 31-38.

Ko, A. C. T., M. Hewko, et al. (2005). "Ex vivo detection and characterization of early dental caries by optical coherence tomography and Raman spectroscopy." Journal of Biomedical Optics **10**(3): 031118.

Koljenovi, S. cacute, et al. (2002). "Discriminating vital tumor from necrotic tissue in human glioblastoma tissue samples by Raman spectroscopy." Laboratory Investigation **82**(10): 1265-1277.

Kotsiantis, S., I. Zaharakis, et al. (2007). Emerging Artificial Intelligence Applications in Computer Engineering: Supervised Machine Learning: A review of Classification Techniques. Lansdale, PA, USA, IOS Press.

Krafft, C. and V. Sergo (2006). "Biomedical applications of Raman and infrared spectroscopy to diagnose tissues." Spectroscopy **20**(5): 195-218.

Kramer, R. (1998). Chemometric Techniques For Quantitative Analysis. Boca Raton, FL, USA, CRC.

Kwac, K. and M. Cho (2005). "Hydrogen bonding dynamics and two-dimensional vibrational spectroscopy: N-methylacetamide in liquid methanol." Journal of Raman Spectroscopy **36**(4): 326-336.

Lei, T. C., D. A. Ammar, et al. (2011). "Label-free imaging of trabecular meshwork cells using Coherent Anti-Stokes Raman Scattering (CARS) microscopy." Molecular Vision **17**: 2628.

Li, Y. Y., Y. Y. Sun, et al. (2012). Rapid Detection of Pesticide Residue in Apple Based on Raman Spectroscopy. Bellingham, WA, USA, Spie-Int Soc Optical Engineering.

Lieber, C. A. and A. Mahadevan-Jansen (2003). "Automated method for subtraction of fluorescence from biological Raman spectra." Applied Spectroscopy **57**(11): 1363-1367.

Lin, S. Y. and C. W. Dence (1992). <u>Methods in Lignin Chemistry</u>. New York, NY, USA, Springer.

Lin, S. Y., M. J. Li, et al. (1998). "Non-destructive analysis of the conformational changes in human lens lipid and protein structures of the immature cataracts associated with glaucoma." <u>Spectrochimica Acta Part A: Molecular and Biomolecular Spectroscopy</u> **54**(10): 1509-1517.

Liu, Y. and T. Liu (2011). "Determination of pesticide residues on the surface of fruits using micro-Raman spectroscopy." <u>Computer and Computing Technologies in Agriculture IV</u> **347**: 427-434.

Long, D. A. (2002). <u>The Raman Effect: A Unified Treatment of the Theory of Raman Scattering by Molecules</u>. Hoboken, NJ, USA, John Wiley & Sons Inc.

Mahadevan-Jansen, A., M. F. Mitchell, et al. (1998). "Near-Infrared Raman spectroscopy for in vitro detection of cervical precancers." <u>Photochemistry and Photobiology</u> **68**(1): 123-132.

Meisel, S., S. Stöckel, et al. (2011). "Assessment of two isolation techniques for bacteria in milk towards their compatibility with Raman spectroscopy." <u>Analyst</u> **136**(23): 4997-5005.

Miura, T. and G. Thomas Jr (1995). <u>Introduction to Biophysical Methods for Protein and Nucleic Acid Research: Optical and Vibrational Spectroscopic Methods</u>. Waltham, MA, USA, Academic Press, Inc.

Mizuno, A., S. Toshima, et al. (1990). "Confirmation of lens hydration by Raman spectroscopy." <u>Experimental Eye Research</u> **50**(6): 647-649.

Mosier-Boss, P. A., S. H. Lieberman, et al. (1995). "Fluorescence rejection in Raman spectroscopy by shifted-spectra, edge detection, and FFT filtering techniques." <u>Applied Spectroscopy</u> **49**(5): 630-638.

Mukhopadhyay, R. (2007). "Raman flexes its muscles." <u>Analytical Chemistry</u> **79**(9): 3265-3270.

Mulbry, W., J. B. Reeves, et al. (2012). "Use of Mid-and Near-Infrared spectroscopy to track degradation of bio-based eating utensils during composting." <u>Bioresource Technology</u> **109**: 93-97.

Nijssen, A., T. C. B. Schut, et al. (2002). "Discriminating basal cell carcinoma from its surrounding tissue by Raman spectroscopy." <u>Journal of Investigative Dermatology</u> **119**(1): 64-69.

Nikbakht, A., T. T. Hashjin, et al. (2011). "Nondestructive determination of tomato fruit quality parameters using Raman spectroscopy." <u>Journal of Agricultural Science and Technology</u> **13**(4): 517-526.

Notingher, I. (2007). "Raman spectroscopy cell-based biosensors." Sensors **7**(8): 1343-1358.

O'Grady, A., A. C. Dennis, et al. (2001). "Quantitative Raman spectroscopy of highly fluorescent samples using pseudosecond derivatives and multivariate analysis." Analytical Chemistry **73**(9): 2058-2065.

Panza, J. L. and J. S. Maier (2007). Raman Spectroscopy and Raman Chemical Imaging of Apoptotic Cells. Society of Photo-Optical Instrumentation, Pittsburgh, PA.

Pappas, D., B. W. Smith, et al. (2000). "Raman spectroscopy in bioanalysis." Talanta **51**(1): 131-144.

Patel, I., W. Premasiri, et al. (2008). "Barcoding bacterial cells: A SERS based methodology for pathogen identification." Journal of Raman Spectroscopy **39**(11): 1660-1672.

Plutowska, B., T. Chmiel, et al. (2011). "A headspace solid-phase microextraction method development and its application in the determination of volatiles in honeys by gas chromatography." Food Chemistry **126**(3): 1288-1298.

Raman, C. V. and K. Krishnan (1928). "A new type of secondary radiation." Nature **121**(3048): 501-502.

Rencher, A. C. and W. F. Christensen (2012). Methods of Multivariate Analysis: Principal Component Analysis. Hoboken, NJ, USA, Wiley.

Sahar, A., T. Boubellouta, et al. (2011). "Synchronous front-face fluorescence spectroscopy as a promising tool for the rapid determination of spoilage bacteria on chicken breast fillet." Food Research International **44**(1): 471-480.

Samyn, P., D. Van Nieuwkerke, et al. (2012). "Quality and statistical classification of Brazilian vegetable oils Using mid-Infrared and Raman spectroscopy." Applied Spectroscopy **66**(5): 552-565.

Savitzky, A. and M. J. E. Golay (1964). "Smoothing and differentiation of data by simplified least squares procedures." Analytical Chemistry **36**(8): 1627-1639.

Schmitt, M. and J. Popp (2006). "Raman spectroscopy at the beginning of the twenty - first century." Journal of Raman Spectroscopy **37**(1-3): 20-28.

Schulmerich, M. V., M. J. Walsh, et al. (2012). "Protein and oil composition predictions of single soybeans by transmission Raman spectroscopy." Journal of Agricultural and Food Chemistry **60**(33): 8097-8102.

Schulze, G., A. Jirasek, et al. (2005). "Investigation of selected baseline removal techniques as candidates for automated implementation." Applied Spectroscopy **59**(5): 545-574.

Schweitzer-Stenner, R. (2005). "Structure and dynamics of biomolecules probed by Raman spectroscopy." Journal of Raman Spectroscopy **36**(4): 276-278.

Sharifzadeh, M., D. Y. Zhao, et al. (2008). "Resonance Raman imaging of macular pigment distributions in the human retina." The Journal of the Optical Society of America A **25**(4): 947-957.

Shaw, P. J. A. (2003). Multivariate Statistics for the Environmental Sciences. Chichester, West Sussex.

Shih, C. J., J. S. Lupoi, et al. (2011). "Raman spectroscopy measurements of glucose and xylose in hydrolysate: Role of corn stover pretreatment and enzyme composition." Bioresource Technology **102**(8): 5169-5176.

Siebinga, I., G. F. J. M. Vrensen, et al. (1992). "Ageing and changes in protein conformation in the human lens: a Raman microspectroscopic study." Experimental Eye Research **54**(5): 759-767.

Siew, D. C. W., G. M. Clover, et al. (1995). "Micro-Raman spectroscopic study of organ cultured corneae." Journal of Raman Spectroscopy **26**(1): 3-8.

Steinwart, I. and A. Christmann (2008). Support Vector Machines. New York, NY, USA, Springer Verlag.

Stone, N. and P. Matousek (2008). "Advanced transmission Raman spectroscopy: A promising tool for breast disease diagnosis." Cancer Research **68**(11): 4424.

Sun, L., C. Yu, et al. (2007). "Surface - Enhanced Raman scattering based nonfluorescent probe for multiplex DNA detection." Analytical Chemistry **79**(11): 3981-3988.

Sun, X., P. Chen, et al. (2012). "Classification of cultivation locations of Panax quinquefolius L samples using high performance liquid chromatography - electrospray ionization mass spectrometry and chemometric analysis." Analytical Chemistry-Columbus **84**(8): 3628.

Szymanski, H. A. (1967). Raman Spectroscopy: Theory and Practice. New York, NY, USA, Plenum Press.

Todorova, M., S. Atanassova, et al. (2011). "Estimation of total N, total P, pH and electrical conductivity in soil by near-Infrared reflectance spectroscopy." Agricultural Science and Technology **3**(1): 50-54.

Tuttolomondo, M., A. Navarro, et al. (2005). "Infrared and Raman spectra of ethyl trifluoromethanesulfonate, $CF_3SO_2OCH_2CH_3$: An experimental and theoretical study." Journal of Raman Spectroscopy **36**(5): 427-434.

Vickers, T. J., R. E. Wambles, et al. (2001). "Curve fitting and linearity: Data processing in Raman spectroscopy." Applied Spectroscopy **55**(4): 389-393.

Wang, Q., S. D. Grozdanic, et al. (2011). "Exploring Raman spectroscopy for the evaluation of glaucomatous retinal changes." Journal of Biomedical Optics **16**(10): 107006.

Wang, Q., S. M. Lonergan, et al. (2012). "Rapid determination of pork sensory quality using Raman spectroscopy." Meat Science **91**(3): 232-239.

Witten, I. H., E. Frank, et al. (2011). Data Mining: Practical Machine Learning Tools and Techniques. Burlington, MA, USA, Morgan Kaufmann.

Wold, S., M. Sjöström, et al. (2001). "PLS-regression: a basic tool of chemometrics." Chemometrics and Intelligent Laboratory Systems **58**(2): 109-130.

Xu, H., J. Aizpurua, et al. (2000). "Electromagnetic contributions to single-molecule sensitivity in surface-enhanced Raman scattering." Physical Review E **62**(3): 4318.

Yang, D. and Y. Ying (2011). "Applications of Raman spectroscopy in agricultural products and food analysis: A review." Applied Spectroscopy Reviews **46**(7): 539-560.

Yitagesu, F. A., F. van der Meer, et al. (2009). "Quantifying engineering parameters of expansive soils from their reflectance spectra." Engineering Geology **105**(3): 151-160.

Yu, C., E. Gestl, et al. (2006). "Characterization of human breast epithelial cells by confocal Raman microspectroscopy." Cancer Detection and Prevention **30**(6): 515-522.

Yu, C. and J. Irudayaraj (2007). "Multiplex biosensor using gold nanorods." Analytical Chemistry **79**(2): 572-579.

Yu, C., L. Varghese, et al. (2007). "Surface modification of cetyltrimethylammonium bromide - capped gold nanorods to make molecular probes." Langmuir **23**(17): 9114-9119.

Zhang, D. and D. Ben-Amotz (2000). "Enhanced chemical classification of Raman images in the presence of strong fluorescence interference." Applied Spectroscopy **54**(9): 1379-1383.

Zhang, K., J. W. Wong, et al. (2011). "Multiresidue pesticide analysis of agricultural commodities using acetonitrile salt-out extraction, dispersive solid-phase sample clean-up and high-performance liquid chromatography-tandem mass spectrometry." Journal of Agricultural and Food Chemistry **59**(14): 7636-7646.

Chapter 2.   EXPLORING RAMAN SPECTROSCOPY FOR THE EVALUATION OF GLAUCOMATOUS RETINAL CHANGES

Qi Wang[1], Sinisa D. Grozdanic[2], Matthew M. Harper[2], Nicolas Hamouche[3], Helga Kecova[2], Tatjana Lazic[2], and Chenxu Yu[1]

[1] Department of Agricultural and Biosystems Engineering, Iowa State University, Ames, Iowa, 50011
[2] U.S. Department of Veterans Affairs Center for Prevention and Treatment of Visual Loss, 601 HWY 6 West, Iowa City, Iowa, 52246
[3] McFarland Clinic Eye Center, 1128 Duff Avenue, Ames, Iowa, 50011

2.1 Abstract

Glaucoma is a chronic neurodegenerative disease characterized by apoptosis of retinal ganglion cells and subsequent loss of visual function. Early detection of glaucoma is critical for the prevention of permanent structural damage and irreversible vision loss. Raman spectroscopy is a technique that provides rapid biochemical characterization of tissues in a nondestructive and noninvasive fashion. In this study, we explored the potential of using Raman spectroscopy for detection of glaucomatous changes *in vitro*. Raman spectroscopic imaging was conducted on retinal tissues of dogs with hereditary glaucoma and healthy control dogs. The Raman spectra were subjected to multivariate discriminant analysis with a support vector machine algorithm, and a classification model was developed to differentiate disease tissues versus healthy tissues. Spectroscopic analysis of 105 retinal ganglion cells (RGCs) from glaucomatous dogs and 267 RGCs from healthy dogs revealed spectroscopic markers that differentiated glaucomatous specimens from healthy controls. Furthermore, the multivariate discriminant model differentiated healthy samples and glaucomatous samples with good accuracy [healthy 89.5% and glaucomatous 97.6% for the same breed (basset

hounds); and healthy 85.0% and glaucomatous 85.5% for different breeds (beagles versus basset hounds)]. Raman spectroscopic screening can be used for *in vitro* detection of glaucomatous changes in retinal tissue with a high specificity.

2.2 Introduction

Glaucoma is an optic neuropathy which is characterized by a progressive optic nerve head cupping and ultimately vision loss. It is the second leading cause of blindness worldwide according to the World Health Organization(Quigley 1999). Glaucoma is characterized by a progressive death of retinal ganglion cells (RGCs), which ultimately results in the loss of visual function. Elevated intraocular pressure (IOP) is considered a primary risk factor for the progression of glaucomatous neuropathy(Quigley 1999; Morrison 2005). In many patients, despite the adequate control of the IOP, the loss of vision continues to progress, which necessitates further identification of molecular mechanisms responsible for the glaucomatous neurodegeneration and development of novel diagnostic modalities, which can detect glaucomatous changes even in patients where IOP is considered normal(Tielsch, Sommer et al. 1991; Levin 1999; Osborne, Chidlow et al. 1999; Morrison 2005).

Raman spectroscopy is a technique that provides rapid characterization of tissue and bodily fluids in a nondestructive and noninvasive fashion. This methodology relies on inelastic scattering of monochromatic light by macro biomolecules in the tissue, usually from a laser in the visible or near-infrared range(Long 1977). Raman spectroscopy is one of the ideal tools to obtain the general biochemical landscape of biological samples. In recent years a marked upsurge in the use of Raman spectroscopy as a noninvasive probing technique has occurred in biomedical research. The diverse applications have included characterization of

different cancers by obtaining biochemical information from an in situ sample such as lung cancer(Huang, McWilliams et al. 2003; Huang, Lui et al. 2005; Taleb, Diamond et al. 2006), vitamin distribution in tissues(Beattie, Maguire et al. 2007; Pudney, Mélot et al. 2007) and the investigation of bone properties(Carden, Rajachar et al. 2003). Once the Raman spectra of a tissue sample are acquired, mathematical classification techniques are utilized to differentiate the spectral signatures of diseased and normal tissues.

In order to better understand glaucomatous changes that occur in the retina and optic nerve and develop effective diagnostic and therapeutic modalities for human disease, it is essential to use animal models that recapitulate the silent and slow development of the disease characterized by a progressive loss of a RGC function. Numerous inducible animal models of glaucoma have been used successfully to test different therapeutic strategies and to evaluate molecular mechanisms of RGC damage resulting from chronic elevation of IOP (Levkovitch-Verbin 2004; Morrison 2005; Rasmussen and Kaufman 2005). Due to the similar size to the human eye, spontaneously occurring large animal models (hereditary canine glaucoma) offer a unique opportunity to obtain functional, structural, and molecular data using instrumentation identical to that used in human patients(Grozdanic, Kecova et al. 2010).

The primary purpose of this study was to explore the potential of using Raman spectroscopy for characterization of glaucomatous molecular signatures. We compared the Raman spectral differences between canine glaucomatous eyes and healthy (control) eyes. The overall objective was to identify spectroscopic markers associated with glaucomatous changes in retinal ganglion cells, and to develop a classification methodology which

potentially could be effectively used to develop *in vivo* imaging modalities for early glaucoma detection using Raman spectroscopy.

2.3 Materials and Methods

2.3.1 Animals and tissue collection

All animal studies were conducted in accordance with the ARVO Statement for Use of Animals in Ophthalmic and Vision Research, and procedures were approved by the Iowa State University Committee on Animal Care (IACUC Grant Nos. 11-09-6827-K and 9-05-5968-K). Eyes were collected from eight basset hounds with hereditary progressive angle closure glaucoma from our colony(Grozdanic, Kecova et al. 2010), and retinal sections were used for Raman spectroscopic investigation. Additionally, eyes from 12 adult healthy beagles and 3 healthy basset hounds were used to serve as a control tissue. All control animals underwent ocular examination (slit lamp biomicroscopy, intraocular pressure evaluation, indirect ophthalmoscopy, gonioscopy), to rule out the possible presence of ocular disease before inclusion in the study.

Eyes were surgically removed from glaucomatous basset hounds once their IOP reached the 35 to 45 mmHg range. At the time of removal, eyes did not have vision, but had positive photopic blink response and pupil light reflex responses. Eyes from control healthy beagles and healthy basset hounds were collected after euthanasia for reasons not related to this study. Eyes were fixed in the 10% buffered paraformaldehyde for 24 h and then rinsed and paraffin imbedded. Twenty micrometer thick central retinal sections containing optic nerve head profile were made and placed on gold-aluminum coated histology slides for the purposes of Raman imaging. Raman spectra were acquired from the fixed tissue sections using a Raman microscope with 4×, 10×, and 100× objectives.

2.3.2   Acquisition of Raman spectrum from retinal tissues

Raman measurements were performed using a DXR Dispersive Raman Microscope (Thermo Scientific, Inc., Madison, Wisconsin) with 780 nm, 14 mW excitation laser with 50 μm pinhole at ambient temperature. Raman spectra were collected with various exposure times (15, 20, 30, 60, 99 s) from 550 and to 2000 cm^{-1} at a resolution of 1 cm^{-1}.

With the 100× objective, individual RGCs can be resolved at subcellular spatial resolution (1 to 1.5 μm), and potential characterization of spectroscopic subcellular compartmentation within individual RGC can be achieved. However, this study focused on differentiation of healthy and glaucomatous tissues as whole units, and subcellular compartmentation was not investigated. Five spectra were collected from each individual cell at different spots and an average spectrum was then calculated (to minimize the variation due to subcellular compartmentation) for that cell to be used as one RGC spectrum in subsequent analysis (105 RGC spectra from glaucomatous basset hound tissues, 105 RGC spectra from healthy basset hound tissues, and 162 RGC spectra from healthy beagle tissues, respectively). With 4× and 10× objectives, spectra were collected from the entire RGC region as a whole (215 spectra from glaucomatous basset hound tissues, 220 spectra from healthy basset hound tissues, and 205 spectra from healthy beagle tissues, respectively). The intensity of the Raman spectrum acquired with low magnification objectives (4× and 10×) was stronger than that of an individual RGC cell due to the larger amount of Raman photons being collected. Nonetheless, their spectroscopic characteristics (i.e., peak wave numbers and peak profiles) were almost identical. Lower magnification objectives delivered the laser power to a much larger area on the tissue samples (~1 mm^2 at 4×), and resulted in a much smaller laser energy density at the tissue surface. After normalization, all spectra from the same type of samples

were pooled together for the development and testing of the discriminant model generated using a support vector machine (SVM). The total spectra for each type of samples were: 320 from glaucomatous basset hound tissues, 325 from healthy basset hound tissues, and 367 from healthy beagle tissues.

2.3.3 Spectral data processing

All spectra were baseline corrected and smoothed using a 21-point averaging algorithm to reduce the baseline variability and background noises at the region between 550 and 2000 cm^{-1}. All spectra were then normalized by setting the intensity of the strongest Raman peak (amide I) to unity. All data processing was conducted using Omnic professional Software Suite (Thermo Scientific, Inc., Madison, Wisconsin).

A standardized residual spectrum (SRS) was then calculated from the original spectral data using equation as follows:

$$SRS(raman\ shift) = \frac{X(raman\ shift) - \bar{X}(raman\ shift)}{s.d.(raman\ shift)}$$

where SRS is the standardized residual spectral intensity at each Raman shift wavenumber, X is the Raman intensity of each individual spectrum at the same Raman shift, $\bar{X}$ is the mean Raman intensity of all spectra from the same data set (i.e., diseased or control) at the same Raman shift, and s.d. is the standard deviation of the Raman intensity within the data set at the same Raman shift. The SRS highlights the variations in spectral data measured from the same type of samples (i.e., control versus diseased), and they were used in a subsequent discriminant analysis.

It should be noted that the chemical fixation with paraformaldehyde alters the chemical makeup of the tissues and changes the Raman spectroscopic characteristics of the tissue samples. However, it has been demonstrated that fixation with paraformaldehyde produces spectral content that is closest to that of living cells(Meade, Clarke et al. 2010). Using hierarchical cluster analysis and principal components analysis (PCA) on individual Raman spectra randomly selected form the nuclear regions of single cancer cells, Draux and co-workers have shown that formalin-fixation and cyto-centrifugation are sample preparation methods that have little impact on the biochemical information as compared to living conditions(Draux, Gobinet et al. 2010). Although the chemical fixation is a possible confounding variable in the differentiation and classification analysis of the spectra acquired from the normal and diseased eye samples, its impact on the analysis is limited in nature since all samples were processed under identical conditions.

2.3.4 PCA and data compression for SVM discriminant modeling

For discriminant analysis, as the dimensions of the data set (i.e., each wave number in the spectral data represents an independent dimension) become large, the limitation on the capability of detecting distinguishable classes becomes severe(Jimenez and Landgrebe 2002). PCA was used in this study for the dimensionality reduction. The data sets (SRS) were compressed into PC scores, and 10 to 50 PC scores (accounted for 94% to 99% of the total variance in the data sets, as shown in Figure 2.6) were selected from 1506 dimensional hyperspectral data as inputs for multivariate discriminant classification model generated using a Support Vector Machine(Steinwart and Christmann 2008) implemented with MATLAB SVM toolbox (The Mathworks, Inc., Natick, Massachusetts) using polynomial kernel function(Gunn 1998). Training sets (110 spectra from each group, 330 in total) and

testing sets (100 spectra/tests) were randomly chosen from the measured spectra [from glaucomatous basset hounds (diseased), healthy basset hounds (control 1), and healthy beagles (control 2)]. Average classification accuracy was calculated from 10 random replications of the discriminant process.

2.4 Results

2.4.1 Spectroscopic characterization of retinal ganglion cells from the retinal tissues

The optical images of the retinal tissue sections of glaucomatous basset hound, healthy hasset hound, and healthy beagle are shown in Figure 2.1. The layers of RGCs were identified under the microscope, as shown in the figures.
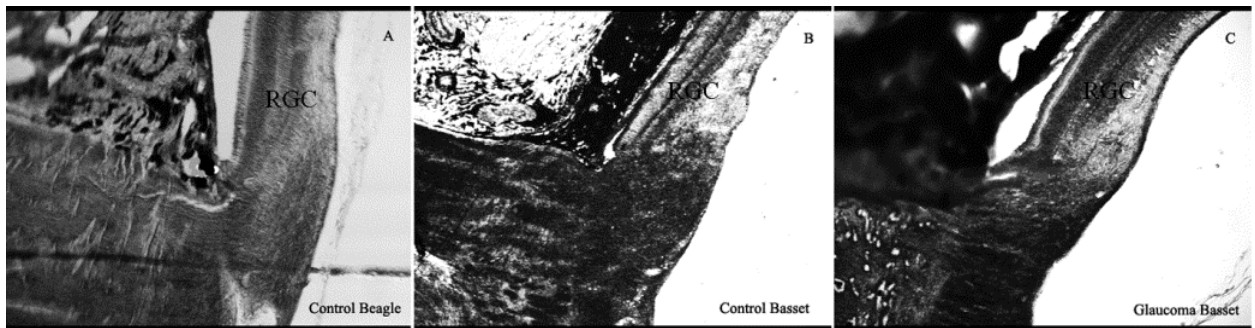
Figure 2.1 Optic images of retinal tissue sections.
They are from a healthy beagle (a), a healthy basset hound (b), and glaucomatous basset hounds (c) on gold coated slides (RGC–retinal ganglion cell layer).

Raman peaks are represented by their wave number (Raman shift) and intensity. The peak intensities are dependent on many factors that may vary from sample to sample (i.e., sample size, exposure time, etc.), but their Raman shift remains identical as long as the molecular makeup is the same. A typical Raman spectra and SRS measured from glaucomatous basset hound RGCs are shown in Figure 2.2 in the 550 to 2000 cm^{-1} range. From the spectra, we could identify contributions from functional groups of the major macromolecules presented in the cells. Proteins (i.e., amide I and III peaks, phenylalanine

peaks, tryptophan peaks, tyrosine peaks) and DNAs (i.e., adenine peak, thymine peaks) can both be characterized with specific Raman bands. The differences shown by these Raman signature bands can be used to differentiate diseased tissues from healthy ones.
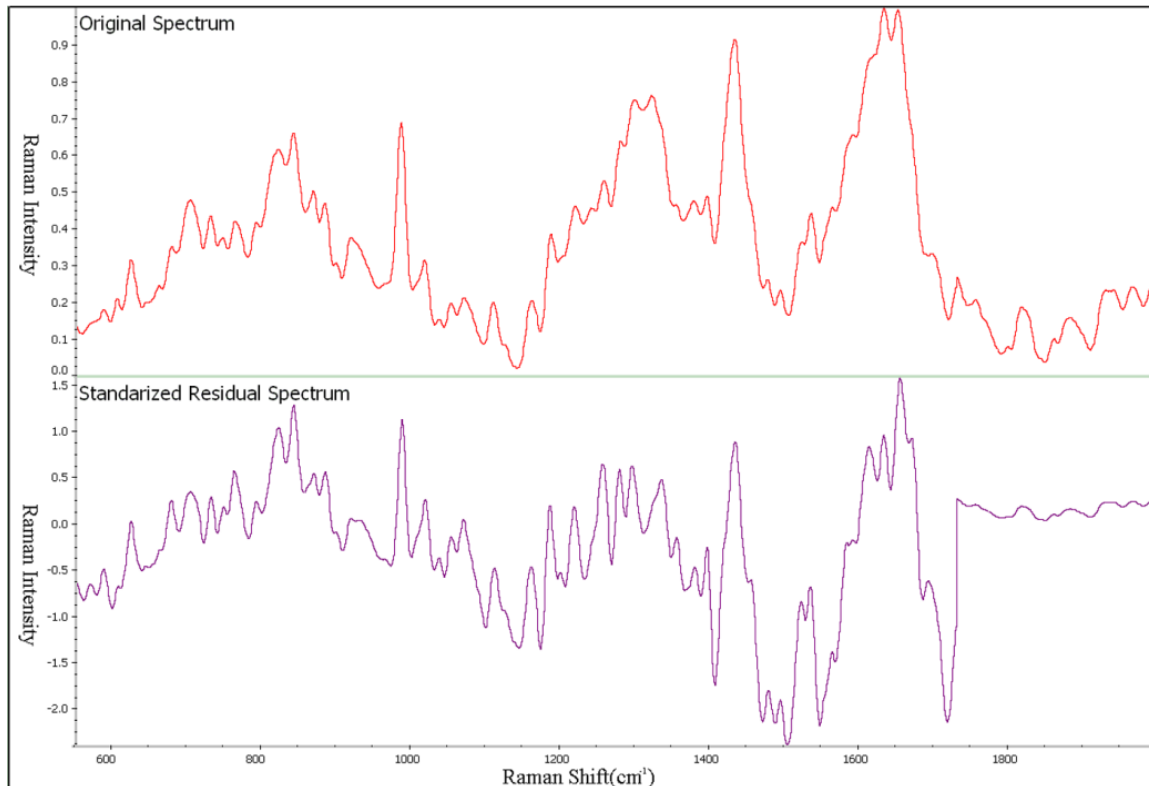
Figure 2.2 Typical Raman spectrum and SRS of RGCs from glaucomatous basset hounds.

To compare the biochemical changes between RGCs of glaucomatous basset hounds and healthy dogs (beagles and basset hounds), represented by their Raman spectroscopic signatures, we measured Raman spectra from 105 RGCs from 8 glaucomatous basset hounds, 105 RGCs from 3 healthy basset hounds, and 162 RGCs from 12 healthy beagles with normal vision. The average and difference spectra between healthy and glaucomatous dogs are shown in Figure 2.3. The difference spectrum was acquired by subtracting the control (healthy beagle and healthy basset hound) from the diseased (glaucomatous basset hound) spectra, respectively. The wave number and intensity changes in those Raman bands of

biological importance were indicative of changes in the secondary structure and variations in local environments of intracellular proteins as well as DNAs, which may determine the characteristics of glaucomatous tissues. Differences at amide III peaks illustrate the changes in the overall concentration of total proteins(Herrero 2008), the composition of proteins also shows some significant differences, as evidenced by Raman bands of various amino acids, at 800 to 1200 cm^{-1}. These changes can potentially be used as spectroscopic markers for the detection of glaucoma.
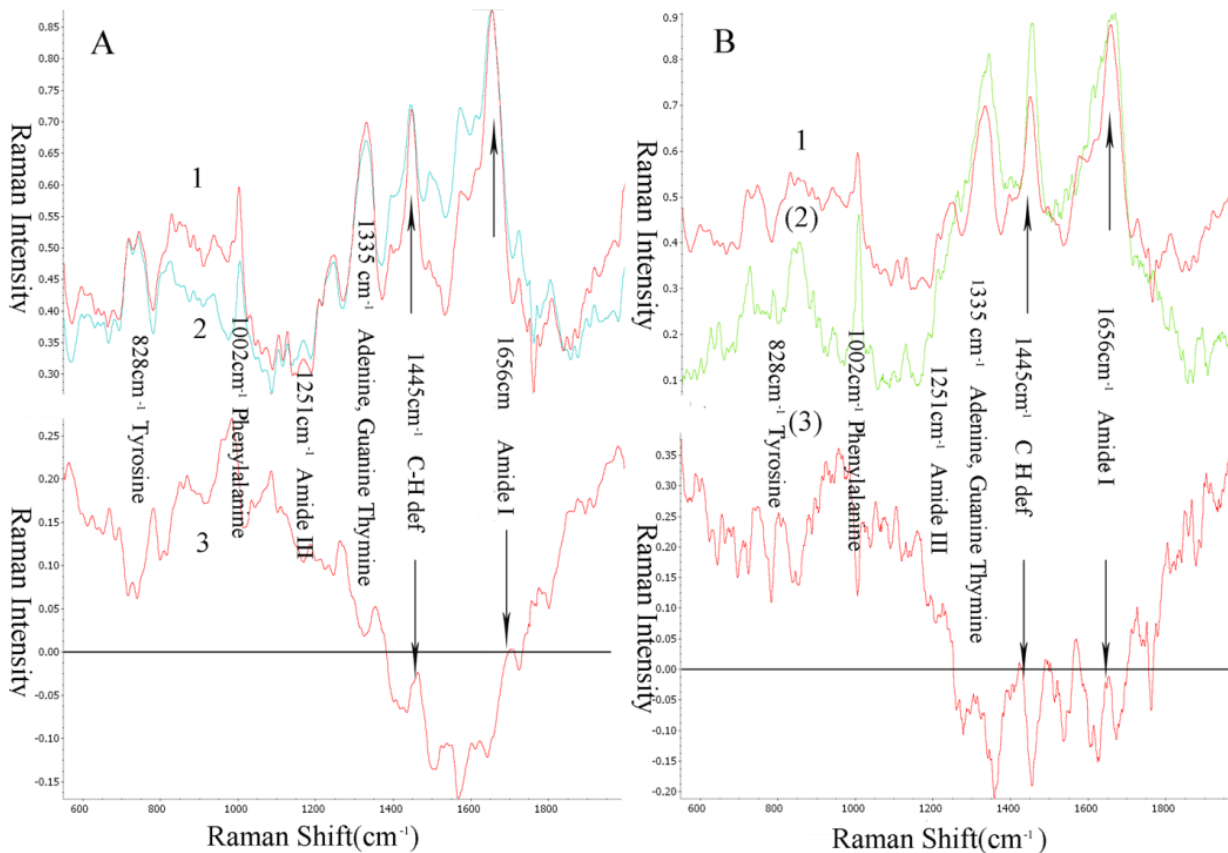
Figure 2.3 Average Raman spectra and difference spectra between glaucomatous and normal RGCs. (A) Healthy basset hounds versus glaucomatous basset hounds; (B) Healthy beagles versus glaucomatous basset hounds. 1. Glaucomatous basset hound; 2. Healthy basset hound; 3. Difference spectrum; (2). Healthy beagle; (3). Difference spectrum.

2.4.2 **Discriminant classification of glaucomatous versus healthy spectra using support vector machine**

A SVM was utilized to generate discriminant classification models to classify a measured spectrum from a retinal tissue sample into the two categories (glaucomatous and normal). One hundred and ten spectra measured from the control group (healthy beagles and healthy basset hounds) and 110 spectra measured from the glaucomatous group (glaucomatous basset hounds) were used as the training data sets to create the SVM discriminant models. After compressing the original spectral data using PCA, the resulted PC scores were used to calculate hyperdimensional classifier. The classification model generated with 10 PC scores (10 D hyperdimensional classifier) is illustrated in Figure 2.4. The support vectors defined a hyperplane that divided the 10 D hyperspace into two domains: normal and glaucomatous. The classification model was then validated through random testing of 10 testing data sets, each containing 100 spectra measured from the control and glaucomatous retinal tissues, respectively. The average classification accuracy was then calculated to evaluate the performance of the classification models.
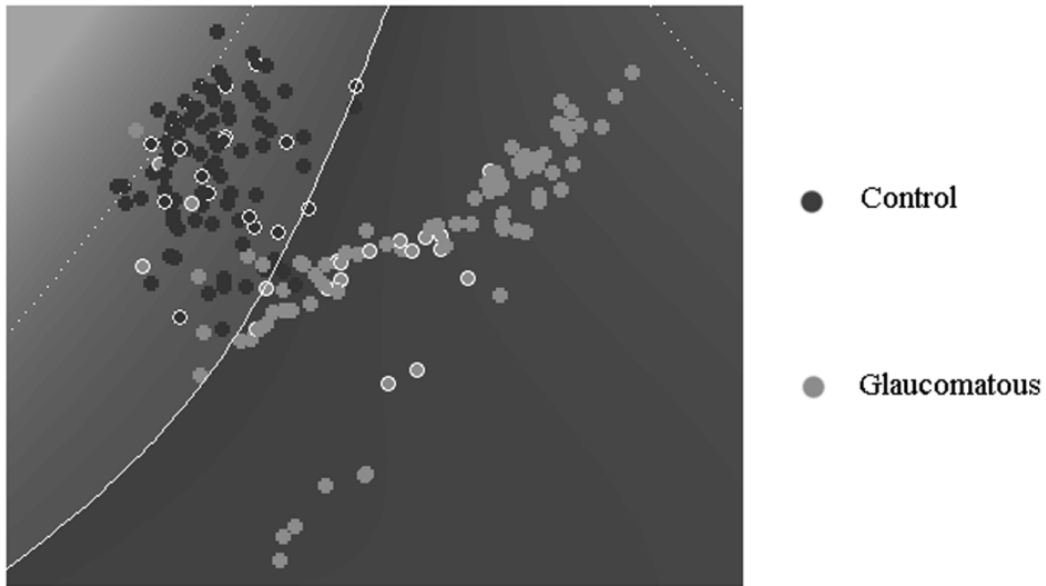
Figure 2.4 An example of the trained classifier by the support vector machine.
The trained classifier between the spectra from RGCs from control healthy basset hounds (black) and glaucomatous basset hounds (gray) is shown. It should be noticed that this is a two-dimensional projection of a 10-D hyperplane separation, thus some overlapping was observed between the two groups while in 10-D space they were well separated. The SVM separating function divided the space into two areas represented by different colors (black and gray). The "circled" dots are support vectors.

2.4.3 Effect of spectral data processing for the classification accuracy

Using PCA, the dimensionality of the spectral data was greatly reduced. With 50 PCs, over 99% of the total variance within spectral data measured for each type of sample could be explained. Ten PCs accounted for 94% of the total variance for each type of samples. Figure 2.5 shows the impact of the number of PCs used in the SVM discriminant model on the classification accuracy for healthy basset hounds (control) and glaucomatous basset hounds (diseased). Consistently, classification accuracy for glaucomatous RGCs was better than that for normal RGCs. We hypothesize that biochemical changes caused by glaucoma may introduce characteristic spectroscopic signatures that lead to more coherently intercorrelated clustering of the data representing glaucomatous RGCs in the hyperspace of the SVM classifier, which results in the better classification accuracy.
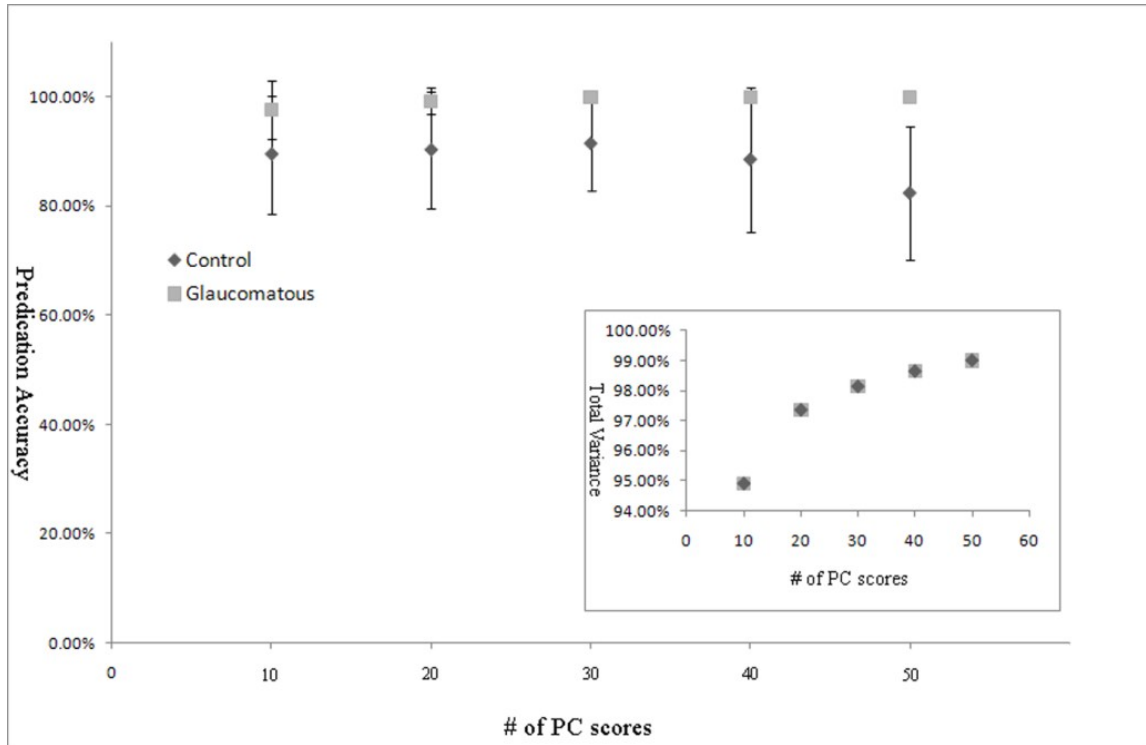
Figure 2.5 The influence of the number of PC scores used in SVM discriminant models on the differentiation accuracy of classifying tissues into healthy and glaucomatous categories. Each error bar indicates the standard deviation of classification accuracy from 10 replications of different training and testing data sets. The inlet shows the total variance accounted for by the number of different PC scores.

As the number of PCs increased from 10 to 30, the classification accuracy for a glaucomatous basset hound reached 100%. Since the number of spectra used in training the discriminant model (220) is far larger than the number of PC scores (<50), it is reasonable to believe that the high classification accuracy is not caused by overfitting(Kemsley 1998). Given the fact that the glaucomatous basset hounds investigated in this study were at the late stage of the disease and have lost almost 100% vision loss, it could be reasoned that severe physiological changes have occurred in their RGCs, which may result from significant biochemical alterations to the cells that are captured in their Raman spectral data. Interestingly, the classification accuracy for healthy basset hounds peaked at 30 PCs (~91%) and slightly declined with more PCs being used in the discriminant model, suggesting that

further optimization is possible by identifying the PCs that are the most responsible for differentiating the diseased group from the healthy group.

2.4.4   Classification differences between different breeds of dogs

Hereditary glaucoma is a genetic disorder affecting RGCs. It is reasonable to hypothesize that the biochemical makeup of the RGCs in diseased basset hounds differs from that of healthy basset hounds. As demonstrated by the high accuracy of the classification results reported before, these intrinsic biochemical differences were captured by their Raman spectroscopic characteristics.

It was previously demonstrated that the gene and protein expression in the retina of glaucomatous and healthy dogs are not breed related, but it rather depends on the stage of glaucoma(Jiang, Harper et al. 2010). Therefore, a valid question to ask is whether or not the spectroscopic differences between healthy and glaucomatous retinal tissue exist regardless of the breeds of the dogs. To answer this question, we have compared Raman spectroscopic data between spectral specimens of two healthy control populations (healthy basset hounds and healthy beagles).

The classification results to differentiate glaucomatous basset hounds and healthy beagles are shown in Figure 2.6 and Table 2.1. A slight reduction in classification accuracy was observed. With 10 PCs, 85.0% of RGCs were correctly classified for the healthy (control) group, and 85.5% RGCs were correctly classified for the glaucomatous group. When classification accuracy was compared within the same breed (control healthy basset hounds and glaucomatous basset hounds), 89.5% RGCs were correctly classified for the healthy group, and 97.6% were correctly classified for the glaucomatous group.
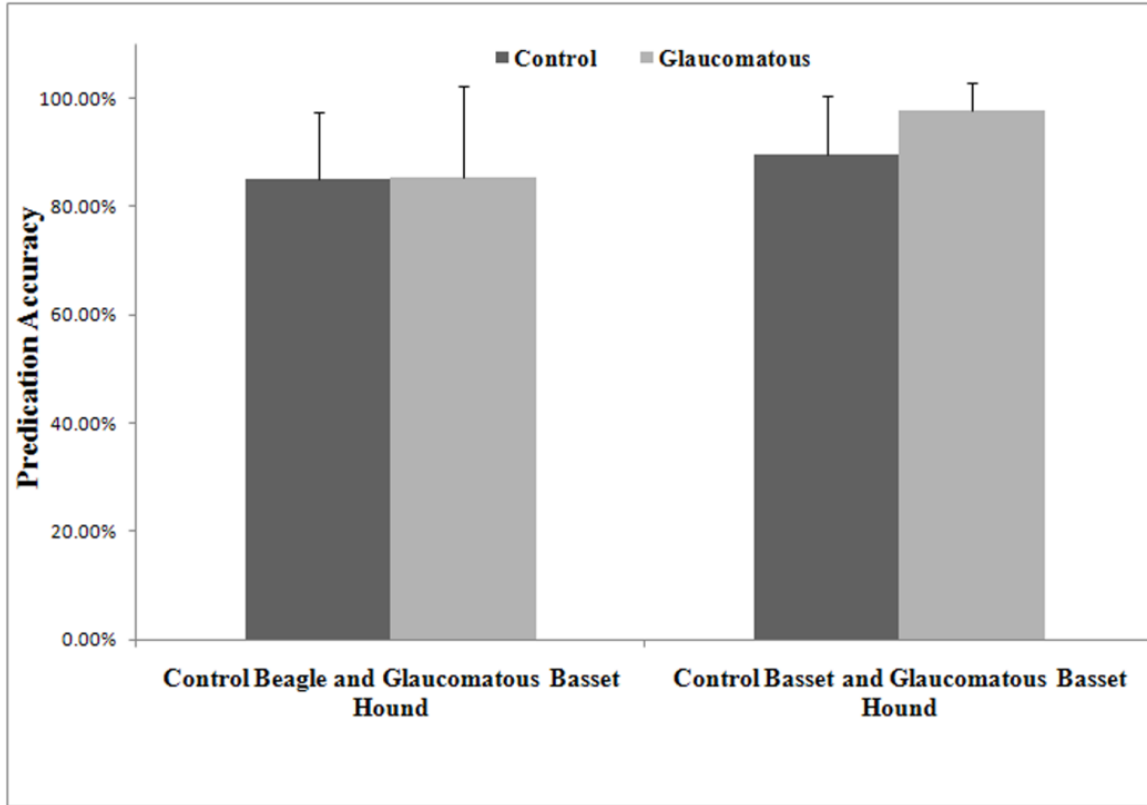
Figure 2.6 Classification performance of the SVM model to differentiate healthy tissues from glaucomatous tissues.

Each error bar indicates the standard deviation of classification accuracy from 10 replications with different training and testing data sets.

Table 2.1 The average classification accuracies for retinal ganglion cells between control and diseased tissues using 10 PCs in SVM discriminant analysis.

	Healthy basset hounds versus glaucomatous basset hounds		Healthy beagle versus glaucomatous basset hounds	
	Normal RGCs	Glaucomatous RGCs	Normal RGCs	Glaucomatous RGCs
Classified as Normal	89.5%	2.4%	85.0%	14.5%
Classified as Glaucomatous	10.5%	97.6%	15.0%	85.5%

These results strongly suggest that there are significant biochemical differences between the retinal ganglion cells of glaucomatous and healthy dogs that can be identified from their Raman spectra, even between different breeds of dogs. The slight reduction in classification accuracy between different breeds may be related to the interbreed genetic

discrepancy, which may result in a greater spread of the data points, and may lead to the mild reduction in the classification accuracy.

The hereditary glaucoma in basset hounds is most likely a result of genetic mutation(s) in the ocular tissues, and potentially all cells in the body. The classification results using the Raman spectra of fibroblast cells and retinal ganglion cells extracted from the control (healthy beagles) and glaucomatous animals (basset hounds) are shown in Figure 2.7 and Table 2.2. A dramatic reduction in classification accuracy was observed. Only 69.2% of fibroblasts were correctly classified for the healthy group, and only 46% of fibroblasts were correctly classified for the glaucomatous group. These observations suggested that the spectroscopic differences between healthy and glaucomatous animals are probably tissue type specific: they could only be observed with high certainty in RGCs, but not in fibroblast cells. The possible explanation for observed changes is that the biochemical footprints associated with glaucoma could be the result of the possible genetic abnormality resulting in a disease phenotype only in ocular tissues. However, it cannot be excluded that the presence of more aggressive disease phenotype in affected eyes (elevated intraocular pressure, neuroinflammatory changes, neuronal(Myers, Trevisani et al. 1998; Katz, Kruger et al. 2003) death, etc.) resulted in more prominent biochemical changes providing a distinct spectroscopic pattern.
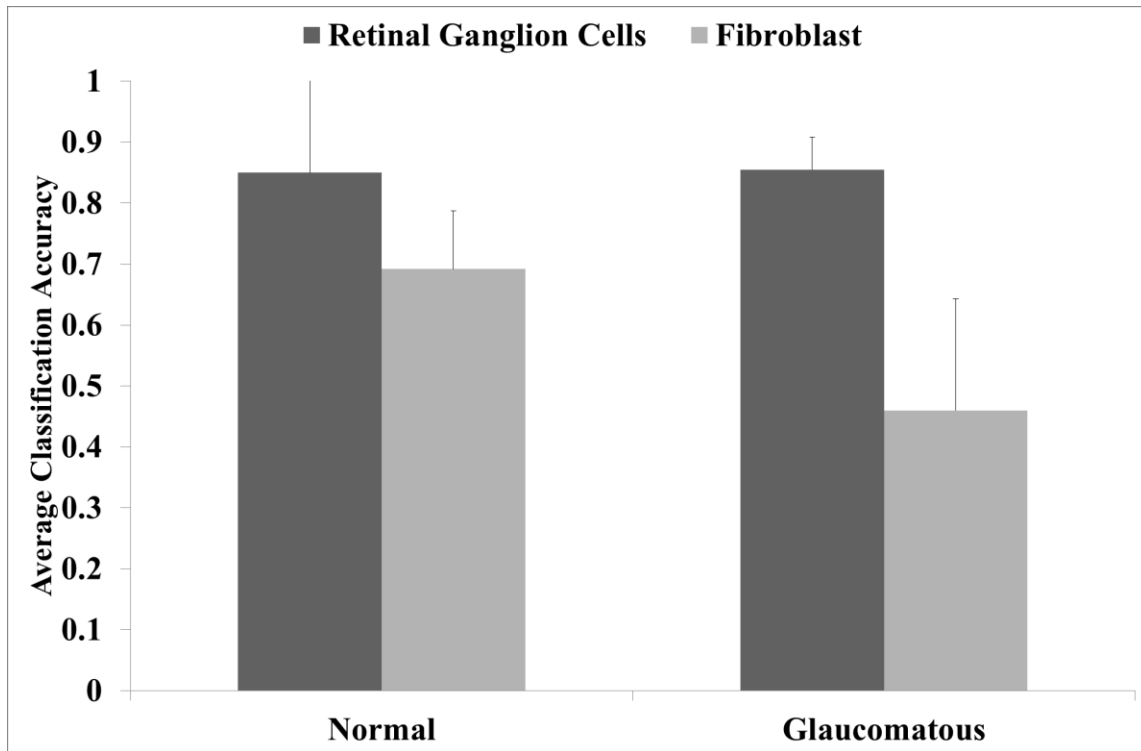
Figure 2.7 Classification accuracy for RGCs and fibroblast cells from glaucomatous basset hounds (glaucomatous) and healthy beagles (normal).

Table 2.2 The average classification accuracies for retinal ganglion cells and fibroblast cells between normal beagle and glaucomatous basset hounds using 10 PCs in SVM discriminant analysis.

	RGCs		Skin fibroblasts	
	Normal (Beagles)	Glaucomatous (Basset hounds)	Normal (Beagles)	Glaucomatous (Basset hounds)
Classified as Normal	85.0%	14.5%	69.2%	54.0%
Classified as Glaucomatous	15.0%	85.5%	30.8%	46.0%

2.5 Conclusions

Glaucoma is a disease which affects millions of patients worldwide, and frequently is diagnosed only when significant optic nerve damage has already developed. For the purposes of this study we have intentionally used tissues from animals with the advanced hereditary glaucoma to make sure that observed spectroscopic changes present in glaucomatous eyes can be detected. For this technology to become a viable clinical tool, it is obvious that testing

needs to be done in animals at a very early stage of the disease, which would be more representative of the condition seen in early glaucoma human patients and glaucoma disease suspects who are in the strongest need of accurate and early diagnosis.

In this study, support vector machine discriminant classification modeling was incorporated with Raman spectroscopy to differentiate and classify differences between glaucomatous and healthy (control) RGCs. It was demonstrated that Raman imaging of RGC chemical profiles results in the high recognition accuracy of the tissue status (91% of healthy RGCs and 100% of glaucomatous RGCs were classified correctly by a predictive model which was trained using defined glaucomatous and healthy control samples). Furthermore, Raman spectroscopic signatures associated with changes in intracellular protein compositions were identified, which potentially can be used as spectroscopic biomarkers for glaucoma diagnosis *in vivo* in the future. To date, Raman spectroscopy has not been fully explored to detect molecular changes in eye tissues associated with glaucoma.

For the 780 nm diode laser that was used in this study, the threshold limit value (TLV) can be calculated as follows(Myers, Trevisani et al. 1998; Katz, Kruger et al. 2003).

$$TLV = 1.8 \times 10^{0.002 \times (\lambda - 700)} \times t^{-1/4} mw/cm^2$$

The TLV determines the maximum permissible energy exposure to the retina in an *in vivo* measurement. In the current study, with 15 and 99 s exposure time, the TLV is 1.32 and 0.82 mW/cm^2, respectively. The laser spot-size on the sample was ~1 mm^2 with 4× objective, and ~10% laser power (1.4 mW) was delivered on the sample. The resulting power density on the sample was 140 mW/cm^2, significantly higher than the TLV. To utilize Raman

spectroscopy for *in vivo* imaging, the laser power density on the retina has to be greatly reduced.

Raman scattering is a weak phenomenon in comparison to autofluorescence coming mostly from protein molecules(Barth and Zscherp 2002), Raman spectral fingerprints can be overwhelmed by stronger fluorescence background when *in vivo* imaging is conducted. Earlier reports utilizing Raman spectroscopy for ophthalmological investigation focused on detection of human macular pigment and glutamate in the eyes, in which the excitation laser wavelength was selected to resonate with the vibrational modes of the pigment/glutamate molecules, and an enhanced Raman signal was achieved(Erckens, Jongsma et al. 2001; Katz, Kruger et al. 2003). To acquire a Raman signal directly from the RGC cells without the resonance enhancement effects, the autofluorescence background has to be removed before the analysis of the vibrational bands takes place. The most common methods for background removal, as the one currently used in this study, are based on digital signal subtraction utilizing the common feature of fluorescent backgrounds—a smooth function of the emission wavelength(Lieber and Mahadevan-Jansen 2003; Schulze, Jirasek et al. 2005). Assuming the fluorescence signal contributes F photons to the recorded signal, while Raman signal adds an additional R photons (for a typical experimental setting R << F), the shot noise introduced by the signal in this case was calculated as $N = (F + R)^{1/2} \approx F^{1/2}$, resulting in a signal-to-noise ratio (SNR) equal to $R/F^{1/2}$ after the fluorescent background has been digitally subtracted from the data. This level of noise is still worse than the ideal SNR in the absence of the fluorescent background, which can be defined as $SNR_{ideal} = R^{1/2}$. From the above equations, it is evident that the SNR degrades by a factor of $(F/R)^{1/2}$, and in order to compensate for it, the data acquisition times of roughly equal to or longer than F/R are required. In other words, if

the fluorescent background is somehow reduced by a factor of 1000, the acquisition times to achieve the same SNR Raman spectra should also be cut by approximately a factor of 1000 (assuming that the shot noise is a predominant source of the data noise). If the acquisition time (exposure time) can be significantly reduced, the higher laser power can be potentially used to obtain a higher-quality spectral signal without reaching the safety limit.

One possible solution to overcome excessive retinal exposure to the high levels of laser energy is to utilize pulse laser with extreme short time-gated detection (10^{-12} s). With such short exposure and detection time, background fluorescence is eliminated (shorter than the fluorescence lifetime so that fluorescence is not developed), and the signal-to-noise ratio of the Raman spectral measurement can be significantly improved, allowing much weaker Raman signals to be detectable(Tahara and Hamaguchi 1993; Matousek, Towrie et al. 1999). An extremely short detection time also allows a much higher laser power to be applied without increasing the overall retinal laser energy exposure. Simple calculation reveals that at 10^{-12} exposure time, the TLV is 2601 mW/cm^2, which is much higher compared to the energy levels used in this study.

In this study, we have demonstrated that Raman imaging can be effectively used for the classification of neuronal changes associated with glaucoma. Further refinement of Raman imaging instrumentation and detection algorithms may provide an exciting opportunity for development of the novel and sensitive diagnostic modalities for the early detection of glaucoma.

2.6 Acknowledgments

2.7 References

Barth, A. and C. Zscherp (2002). "What vibrations tell about proteins." Quarterly Reviews of Biophysics **35**(04): 369-430.

Beattie, J., C. Maguire, et al. (2007). "The use of Raman microscopy to determine and localize vitamin E in biological samples." The FASEB Journal **21**(3): 766.

Carden, A., R. Rajachar, et al. (2003). "Ultrastructural changes accompanying the mechanical deformation of bone tissue: A Raman imaging study." Calcified Tissue International **72**(2): 166-175.

Draux, F., C. Gobinet, et al. (2010). "Raman spectral imaging of single cancer cells: Probing the impact of sample fixation methods." Analytical and Bioanalytical Chemistry **397**(7): 2727-2737.

Erckens, R., F. Jongsma, et al. (2001). "Raman spectroscopy in ophthalmology: From experimental tool to applications *in vivo*." Lasers in Medical Science **16**(4): 236-252.

Grozdanic, S., H. Kecova, et al. (2010). "Functional and structural changes in a canine model of hereditary primary angle-closure glaucoma." Investigative Ophthalmology & Visual Science **51**(1): 255.

Gunn, S. (1998). Support vector machines for classification and regression. ISIS Technical Report.

Herrero, A. (2008). "Raman spectroscopy for monitoring protein structure in muscle food systems." Critical Reviews in Food Science and Nutrition **48**(6): 512-523.

Huang, Z., H. Lui, et al. (2005). "Raman spectroscopy in combination with background near infrared autofluorescence enhances the *in vivo* assessment of malignant tissues." Photochemistry and Photobiology **81**(5): 1219-1226.

Huang, Z., A. McWilliams, et al. (2003). "Near infrared Raman spectroscopy for optical diagnosis of lung cancer." International Journal of Cancer **107**(6): 1047-1052.

Jiang, B., M. M. Harper, et al. (2010). "Neuroinflammation in advanced canine glaucoma." Molecular Vision **16**: 2092.

Jimenez, L. and D. Landgrebe (2002). "Supervised classification in high-dimensional space: Geometrical, statistical, and asymptotical properties of multivariate data." Systems,

Man, and Cybernetics, Part C: Applications and Reviews, IEEE Transactions **28**(1): 39-54.

Katz, A., E. Kruger, et al. (2003). "Detection of glutamate in the eye by Raman spectroscopy." Journal of Biomedical Optics **8**(2): 167-172.

Kemsley, E. K. (1998). Discriminant Analysis and Class Modelling of Spectroscopic Data. Hoboken, NJ, USA, Wiley.

Levin, L. (1999). "Direct and indirect approaches to neuroprotective therapy of glaucomatous optic neuropathy." Survey of Ophthalmology **43**: S98-S101.

Levkovitch-Verbin, H. (2004). "Animal models of optic nerve diseases." Eye **18**(11): 1066-1074.

Lieber, C. A. and A. Mahadevan-Jansen (2003). "Automated method for subtraction of fluorescence from biological Raman spectra." Applied Spectroscopy **57**(11): 1363-1367.

Long, D. (1977). Raman Spectroscopy. New York, NY, USA, McGraw-Hill.

Matousek, P., M. Towrie, et al. (1999). "Efficient rejection of fluorescence from Raman spectra using picosecond Kerr gating." Ratio **1**: 1.

Meade, A. D., C. Clarke, et al. (2010). "Studies of chemical fixation effects in human cell lines using Raman microspectroscopy." Analytical and Bioanalytical Chemistry **396**(5): 1781-1791.

Morrison, J. (2005). "Elevated intraocular pressure and optic nerve injury models in the rat." Journal of Glaucoma **14**(4): 315.

Myers, J., M. Trevisani, et al. (1998). "Laser energy reaching the posterior pole during transscleral cyclophotocoagulation." Archives of Ophthalmology **116**(4): 488.

Osborne, N., G. Chidlow, et al. (1999). "The potential of neuroprotection in glaucoma treatment." Current Opinion in Ophthalmology **10**(2): 82.

Pudney, P., M. Mélot, et al. (2007). "An *in vivo* confocal Raman study of the delivery of trans retinol to the skin." Applied Spectroscopy **61**(8): 804-811.

Quigley, H. (1999). "Neuronal death in glaucoma." Progress in Retinal and Eye Research **18**(1): 39-57.

Rasmussen, C. and P. Kaufman (2005). "Primate glaucoma models." Journal of Glaucoma **14**(4): 311.

Schulze, G., A. Jirasek, et al. (2005). "Investigation of selected baseline removal techniques as candidates for automated implementation." Applied Spectroscopy **59**(5): 545-574.

Steinwart, I. and A. Christmann (2008). <u>Support Vector Machines</u>. New York, NY, USA, Springer Verlag.

Tahara, T. and H. Hamaguchi (1993). "Picosecond Raman spectroscopy using a streak camera." <u>Applied Spectroscopy</u> **47**(4): 391-398.

Taleb, A., J. Diamond, et al. (2006). "Raman microscopy for the chemometric analysis of tumor cells." <u>Journal of Physical Chemistry B</u> **110**(39): 19625-19631.

Tielsch, J., A. Sommer, et al. (1991). "Racial variations in the prevalence of primary open-angle glaucoma: The Baltimore eye survey." <u>Jama</u> **266**(3): 369.

Chapter 3.   DETECTION AND CHARACTERIZATION OF GLAUCOMA-LIKE CANINE RETINAL TISSUES USING RAMAN SPECTROSCOPY

Modified from a paper submitted to "Journal of Biomedical Optics"

Qi Wang[1], Sinisa D. Grozdanic[2], Matthew M. Harper[2], Nicolas Hamouche[3], Helga Kecova[2], Tatjana Lazic[2], and Chenxu Yu[1]

[1] Department of Agricultural and Biosystems Engineering, Iowa State University, Ames, Iowa, 50011
[2] U.S. Department of Veterans Affairs Center for Prevention and Treatment of Visual Loss, 601 HWY 6 West, Iowa City, Iowa, 52246
[3] McFarland Clinic Eye Center, 1128 Duff Avenue, Ames, Iowa, 50011

3.1 Abstract

Early detection of pathological changes and progression in glaucoma and other neuroretinal diseases remains a great challenge and is critical to reduce permanent structural and functional retina and optic nerve damage. Raman spectroscopy is a sensitive technique that provides rapid biochemical characterization of tissues in a nondestructive and noninvasive fashion. In this study, spectroscopic analysis was conducted on the retinal tissues of seven beagles with acute elevation of intraocular pressure (AEIOP), six beagles with compressive optic neuropathy (CON) and five healthy beagles. Spectroscopic markers were identified associated with the different neuropathic conditions. Furthermore, the Raman spectra were subjected to multivariate discriminate analysis to classify independent tissue samples into diseased/healthy categories. The multivariate discriminant model yielded an average optimal classification accuracy of 72.6% for AEIOP and 63.4% for CON with 20 principal components being used that accounted for 87% of the total variance in the data set. A strong correlation ($R^2>0.92$) was observed between pERG characteristics of AEIOP dog and Raman separation distance that measures the separation of spectra of diseased tissues from normal tissues, however the underlining mechanism of this correlation remains to be

understood. Since AEIOP mimics the pathological symptoms of acute/early stage glaucoma, it was demonstrated in this study that Raman spectroscopic screening has the potential to become a powerful tool for the detection and characterization of early stage disease.

3.2 Introduction

Glaucoma is a slowly progressive chronic optic neuropathy that is characterized by retinal ganglion cell (RGC) death with subsequent loss of optic nerve axons and decrements in visual function. Glaucoma is diagnosed clinically by means of functional and structural analysis of the retina and optic nerve. After an initial diagnosis, these tests need to be repeated at regular intervals to assess the progress of the disease and any treatment effect. Unfortunately, a significant loss of retinal cells can occur before any of the current tests show an abnormality. Namely, between 25 to 35% of the RGCs could be lost before any visual field defect is detectable(Kerrigan–Baumrind, Quigley et al. 2000). The detection of progressive changes in glaucoma can also be demanding, requiring multiple testing sessions over a prolonged period of time. Hence, a critical gap exists to develop clinical tests that could aid in the earlier diagnosis and monitoring of glaucoma.

Raman spectroscopy measures the inelastic scattering of laser light by biomolecules in the tissue samples and can be used to predict the general biochemical composition of biological samples(Wang, Grozdanic et al. 2011). As such, it can be used to provide rapid characterization of healthy versus diseased tissues in a nondestructive and noninvasive fashion. In recent years, the technique has been applied to characterize various biological samples, including mineralized tissue such as bone and teeth (Boskey and Mendelsohn 2005; Ko, Choo-Smith et al. 2006), skin(Knudsen, Johansson et al. 2002), brain(Koljenovi , Schut et al. 2005), the gastrointestinal tract(Shim, Wong Kee Song et al. 2000), mouth(Schut,

Witjes et al. 2000; Huang, Lui et al. 2005), blood vessels(Van de Poll, Kastelijn et al. 2003) and breast(Shafer Peltier, Haka et al. 2002). In ophthalmology, Raman spectroscopy has been used to determine carotenoid pigment levels in human retina (Gellermann 2002; Bernstein, Zhao et al. 2004), altered vitreous molecules such as glycated collagen in diabetic vitreoretinopathy (Sebag 2004), the distribution of cholesterol in a rat eye lens (Sijtsema, Duindam et al. 1996) as well as to detect glutamate in the vitreous of porcine eyes in an ex vivo experiment (Kruger, Minko et al. 2003).

Raman spectroscopy provides rapid characterization of the chemical composition and molecular structures in cells and tissues. Diseases and other pathological anomalies lead to chemical and structural changes at the molecular level in tissues that are reflected in their Raman spectra before the appearance of clinical symptoms. These spectral changes can be used as sensitive, phenotypic markers disease (Krafft and Sergo 2006) and could potentially lead to early disease diagnosis before clinical symptoms are apparent. Once Raman spectra are acquired, mathematical classification techniques are utilized to differentiate the spectral signatures of diseased and normal tissues. In our previous study, Raman spectroscopic screening was utilized to detect glaucomatous changes in retinal tissue with a high specificity (Wang, Grozdanic et al. 2011). The specimens analyzed in that study were obtained from canine retinas with severe vision loss due to advanced hereditary angle-closure glaucoma. The physiological and biochemical retinal changes were quite significant in comparison to the healthy controls. It remains to be seen whether Raman spectroscopic screening can be used to detect glaucomatous changes at earlier stages of the disease in an animal model lacking any genetic predisposition for ocular pathology.

In order to better understand glaucomatous changes that occur at an early stage of glaucoma, it is essential to use animal models that recapitulate the development of the disease that is characterized by a progressive loss of RGC function. Elevated intraocular pressure (IOP) is considered a primary risk factor for the progression of glaucomatous neuropathy(Quigley 1999; Morrison 2005) and remains the etiological factor toward which all current therapeutic efforts are directed. Acute elevation of intraocular pressure (AEIOP) induces deformation of the lamina cribrosa and anterior scleral canal wall and underlies the onset of optic nerve head (ONH) surface hyper-compliance that is typically associated with early stage of glaucoma(Bellezza, Rintalan et al. 2003). Compressive optic neuropathy (CON) occurs when lesions appear along the optic nerve, which induces damage to the optic nerve and a progressive loss of visual function and structure (Girkin 2005). Due to the similar size of the human and canine eye, functional and structural data can be acquired using instrumentation identical to that which is used in human patients (Gelatt 1977; Grozdanic, Kecova et al. 2010). In this study retinal tissues from canine models of AEIOP and CON were compared to healthy control samples using Raman spectroscopy.

The primary purpose of this study was to explore the potential of using Raman spectroscopy for characterization of glaucoma-like spectroscopic signatures at an early stage of retinal damage to identify spectroscopic markers in the eyes and to classify methods to effectively differentiate early stage glaucoma-like tissues and healthy tissues.

3.3 Materials and Methods

3.3.1 Acute elevation of the intraocular pressure in beagles

Laboratory beagles were anesthetized with 2.5% halothane and a mixture of nitrous oxide and oxygen (30 : 70 ratio). Body temperature was maintained using a heating pad. The

pupils were dilated with topical 10% phenylephrine hydrochloride (Ak-dilate™, Akorn Inc.,

Buffalo Grove, IL, USA) and 1% tropicamide (Tropicamide, Falcon Pharmaceuticals, Fort

Worth, TX, USA). Prior to anterior chamber cannulation the eye was surgically prepped and

a drop of 0.5% propracaine hydrochloride (Falcon Pharmaceuticals, Fort Worth, TX, USA)

was instilled. The anterior chamber was then cannulated with a 25-gauge needle connected to

a reservoir containing 0.9% NaCl. The intraocular pressure in experimental eyes was

controlled by adjusting the height of the reservoir to maintain a level of systolic blood

pressure for 60 min. The systolic blood pressure was evaluated with an ultrasonic Doppler

flow detector (Model 811-L, Parks Medical Electronics Inc., Las Vegas, NV, USA) every

5 min. The average elevation of intraocular pressure was between 100 and 160 mmHg. After

60 min, the bottle was lowered and the needle was subsequently removed from the anterior

chamber and topical antibiotic ointment (Vetropolycin, Pharmaderm Inc., Melville, NY,

USA) was applied on the cornea. Postoperative treatment included one dose of

hydromorphone HCl (0.1 mg/kg, Dilaudid, Abbott Laboratories, Lake Forest, IL, USA)

subcutaneously and application of topical antibiotic ointment to the operated eye twice daily

for 2 days (Grozdanic, Matic et al. 2007).

3.3.2   Dog model for compressive optic neuropathy

Compressive optic neuropathy was induced in laboratory beagles by surgical

implantation of custom-made silicone reservoir (Nagor LTD, Isle of Man, UK) into the left

orbit. Animals were pre-medicated with intramuscular hydromorphone hydrochloride

(0.1mg/kg; Dilaudid®, Hospira, Inc., IL, USA) and acepromazine maleate (0.01mg/kg,

Vedco, USA). Anesthesia was induced with intravenous administration of propofol (3-

5mg/kg, Schering Plough Animal Health, USA) and maintained with 1.5-2.5% halothane

(Halocarbon Laboratories, USA) in a mixture of 1:1 oxygen and nitrous oxide. Body temperature was maintained using a heating pad (T/Pump® Professional, Gaymar Industries Inc., NY, USA) and a heating blanket (Bair Hugger®, Arizant Healthcare Inc., MN, USA). Systolic, mean and diastolic blood pressures were recorded with oscillometric arterial blood pressure monitor (Cardell Veterinary Monitor, Model 9401, Paragon Medical Supply, FL, USA) every 5 minutes and maintained in physiological levels with constant intravenous drip of lactated ringer's solution (10 ml/kg for the first hour, 5 ml/kg after) during the orbital implant surgery and subsequent recordings. Heart rate, hemoglobin saturation, respiratory rate, expired CO_2, end-tidal CO_2 and end-tidal concentration of halothane were constantly monitored (Datascope Multinex Plus anesthesia monitor, Absolute Medical Equipment, NY, USA). After induction of anesthesia, the area around the left orbit and left side of the head was clipped and prepared for aseptic surgical procedure. Intravenous cefazolin (22 mg/kg; Cefazolin, Sandoz Inc., NJ, USA) was administered on a prophylactic basis and the same dose was repeated every 2 hours throughout the procedure.

With the animals in sternal recumbence, a skin incision was made above the left eye, in the area of orbital ligament. The palpebral nerve was identified and where necessary, retracted with sterile umbilical tape to avoid its damage during the procedure. The orbital ligament was incised lengthwise to enable access to the retrobulbar space. A Gelpi retractor was inserted into the incision to enable good visualization of the surgical site and a custom-made inflatable silicone implant (Nagor LTD, Isle of Man, UK) was introduced into the orbit, directly behind the eye. The injection port of the implant was passed through the incision in the orbital ligament and under the skin of the forehead into the occipital area, where it was fixed to the muscle fascia with absorbable monofilament suture (PDS 3-0, Ethicon, USA).

Surgical incisions were closed routinely. Post-operative analgesia and inflammation control was maintained with hydromorphone hydrochloride (0.1mg/kg BW) every 6-8 hours (as needed) for 3 days and carprofen (4.4 mg/kg BW) once daily for 7 days. The implant was inflated to a pressure that gave a complete optic nerve perfusion deficit as measured using fluorescein angiography. The device was then deflated until fluorescein was observed in the retina.

3.3.3   Animals and tissue collection

All animal studies were conducted in accordance with the ARVO Statement for Use of Animals in Ophthalmic and Vision Research, and procedures were approved by the Iowa State University Committee on Animal Care. Eyes were collected from seven beagles with acute elevation of intraocular pressure (AEIOP), six beagles with compressive optic neuropathy for 24 hours (CON) were used for Raman spectroscopic investigation. Additionally, eyes from five adult healthy beagles of 6 months of age were used as controls. All control animals underwent ocular examination (slit lamp biomicroscopy, intraocular pressure evaluation, indirect ophthalmoscopy and gonioscopy) to rule out the possible presence of ocular disease before inclusion in the study. Eyes were surgically removed from the beagles after euthanasia. They were fixed in 10% buffered paraformaldehyde for 24 hours, rinsed and paraffin embedded. Twenty micron thick retinal sections were made and placed on gold-aluminum coated histology slides for the purposes of Raman imaging. Raman spectra were acquired from the fixed tissue sections using a Raman microscope with 10× objective, with a laser spot size of ~50 μm diameter.

3.3.4 Acquisition of Raman spectrum from retinal tissues

In this study, Raman measurements were performed using a DXR Dispersive Raman Microscope (Thermo Scientific, Inc., Madison, WI) with 780nm, 14mW excitation laser with a charge coupled device (CCD) camera and 50 μm pinhole in ambient temperature. Raman spectra were collected with 99s exposure time from 600 and to 2000 cm^{-1} at a resolution of 1 cm^{-1} (Full Range Grading).

3.3.5 Spectral data processing

The acquired Raman spectra were pre-processed to remove artifacts caused by background fluorescence and intensity fluctuations (Krafft and Sergo 2006; Zhao, Lui et al. 2007; Bocklitz, Walter et al. 2011). Using near infrared excitation (780nm) radically reduces the observance of sample auto-fluorescence. To further reduce the remaining fluorescence, a polynomial background subtraction method was implemented(Jimenez and Landgrebe 1998). Another challenge in spectral pre-processing is to capture important patterns in the spectra while removing noise or other fine-scale structures. The 11-point moving average method was used in this study to smooth the spectra. Finally all spectra were area-normalized for intensity consistency at the region between 600 cm^{-1} to 2000 cm^{-1}. All data processing was conducted using R, a widely used language and software tool for statistical computing and graphics.

3.3.6 Principal component analysis

In Raman spectra, each wavenumber represents a dimension or variable. Commonly, data in one Raman spectrum contains thousands of dimensions, which makes statistical analysis much more challenging. For discriminant analysis, as the (number of) dimensions of the data becomes large, the limitation on the capability of detecting distinguishable classes

becomes severe(Jimenez and Landgrebe 1998). Due to the fact that most statistical methods are based on optimization criteria, it is advisable to reduce the dimension(s) of the problem, which results in decreasing computational costs and increasing probability of finding the best model representing the data. For this purpose, often a Principal component regression (PCA) is utilized.

$$Y = L \times S^T + E$$

In the equation above, Y is the matrix of spectra, S is the score matrix, L is the matrix of loadings and E is the error matrix. The data are compressed into PC scores.

All spectra were polynomial baseline corrected, smoothed using moving average algorithms and area normalized at the region between 600cm^{-1} to 2000cm^{-1} before principal component regression (PCA) is utilized. 10-40 PCs (account for at least 90% of total variance in the data) were selected from thousands of dimensional hyper-spectral data as inputs for multivariate discriminant classification model.

For each dog in AEIOP and CON groups, the calculated PC spectra form a cluster. The average intra-cluster Euclidean distances in the multi-dimensional PC space (one dimension represents one principal component for our data) are calculated between each diseased dog and the control group (i.e., all spectra from the control dogs). Our hypothesis is that more distinguishable spectroscopic signatures between diseased dog and the control group will translate into a higher separation distance in the multidimensional PC space. Hence, the calculated average distance may serve as a base for a disease score system that predicts the severity of the disease conditions. This hypothesis was checked against AEIOP,

CON and late-stage close angle glaucoma, with mixed results. More work is needed to further refine the disease score system.

3.3.7 Cross-validation, independent validation and discriminant modeling

Cross-validation is a technique for assessing how the results of a statistical analysis will generalize to an independent dataset(Witten and Frank 2005). One round of cross-validation involves partitioning a sample of data into complementary subsets, performing the analysis on one subset (called the training set), and validating the analysis on the other subset (called the validation set or testing set). To reduce variability, multiple rounds of cross-validation are performed using different partitions, and the validation results are averaged over the rounds.

One inherent drawback of cross-validation comes from the fact that the validation set and the training set are indeed spectra measured from the same batch of samples (i.e., dogs). The high prediction accuracy reported from cross-validated discriminant models can be biased. In this study, to further confirm that Raman spectroscopic data can yield enough information that distinguishes diseased tissues from normal ones, even at an early stage of the disease, we tested the discriminant model by independent validation. In this approach, spectra from 2 beagles in each group were randomly selected as validation datasets that were excluded from the training pool used to create the SVM classification models. 10 repetitions were conducted. 20 PCs were used to develop the discriminant model. The validation set only contains spectral data that were acquired from an independent set of samples (i.e., dogs), with no overlap with the sample pool from which the spectral data for the training of the discriminant model were acquired.

In general, all spectra were baseline corrected, smoothed to reduce the baseline variability and normalized using R before classification analysis. Support vector machine (SVM) based on R packages "e1071"(Karatzoglou, Meyer et al. 2005) with folded cross validation was utilized as the discriminant classification modeling technique.

3.3.8 Pattern electroretinography (pERG) characterization of the disease status of AEIOP dogs

The pattern electroretinogram (pERG), which measures the retinal response evoked by viewing a temporally alternating pattern, is important in providing information about retinal ganglion cell function. With appropriate paradigms, pERG is objectively correlated with the overall RGC status (Bach and Hoffmann 2008). The P50 and the N95 component were affected rather similarly by glaucoma in PERGs. In this study, pERG was performed to evaluate the damage induced by elevated IOP to RGCs in the AEIOP dogs. pERGP50-N95 amplitude and P50op/P50ctrl ratio were obtained following ISCEV standard(Holder, Brigell et al. 2007).

3.4 Results

3.4.1 Spectroscopic difference between the RGCs of Acute Elevation of Intraocular Pressure (AEIOP), Compressive Optic Neuropathy (CON) and healthy beagles

The optical images of the retinal tissue sections of Acute Elevation of Intraocular Pressure (AEIOP) beagle, Compressive Optic Neuropathy (CON) beagle, and healthy beagle are shown in Figure 3.1. The layers of RGCs were identified under the microscope, as shown in the figures. To compare the biochemical changes represented by the Raman spectroscopic signatures, we measured Raman spectra from 133 RGCs from five healthy beagles with normal vision, 114 RGCs from seven AEIOP beagles and 160 RGCs from six CON beagles. The difference spectra were acquired by subtracting the average spectrum of control (healthy beagle) from the diseased (AEIOP or CON) average spectra (Figure 3.2).
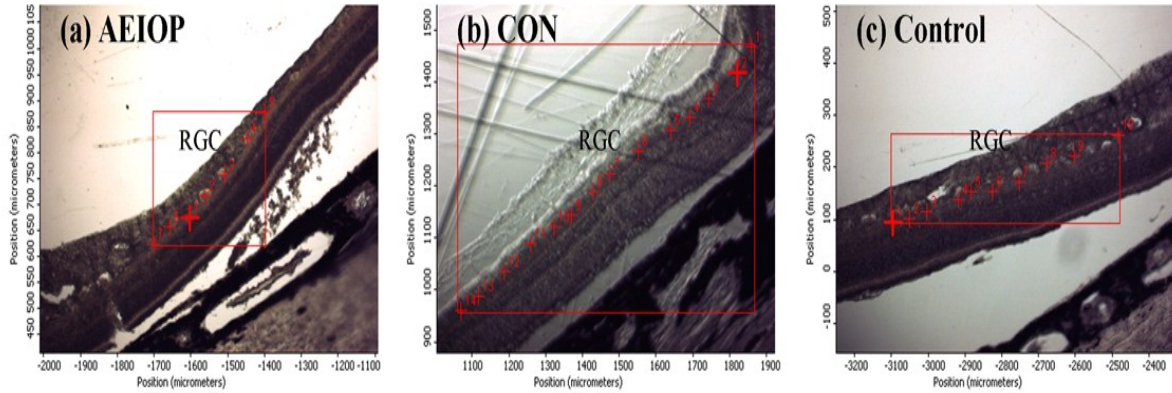
Figure 3.1 Optic images of retinal tissue sections.
An AEIOP beagle (a), a CON beagle (b), and healthy beagle(c) on gold coated slides (RGC-retinal ganglion cell layer).

The wave number and intensity changes in the Raman bands are indicative of changes in the secondary structure and variations of intracellular proteins as well as local cellular environments. Looking at the actual and difference spectral graphs between AEIOP, CON and normal beagles (Figure 3.2), we noted hikes corresponding to the Amide III (1252cm^{-1}) and Amide I (1656cm^{-1}) peaks in both conditions. While the total protein concentration indicated by the Amide III peak(Herrero 2008), seems to be increased in both conditions, suggesting an elevated protein synthesis in the RGCs, there is significant differences in the Raman bands of various amino acids at 800-1200 cm^{-1} in AEIOP/CON RGCs compared to healthy RGCs. This suggests that different genes are being expressed leading to a different protein composition in each of the two conditions. The Amide I peak, on the other hand, may be caused by different concentrations of cholesterol, ceramide and unsaturated fatty acids which have cis C=C Raman bands at 1650cm^{-1}. Also, the difference spectra reveal that, in general, the changes in AEIOP RGCs are more significant than that of CON RGCs. Quantitatively, the difference spectra reveal that, in general, the changes in AEIOP RGCs are

more significant than that of CON RGCs. This is consistent with the fact that AEIOP has a more direct and probably more generalized impact on the RGCs than CONs.
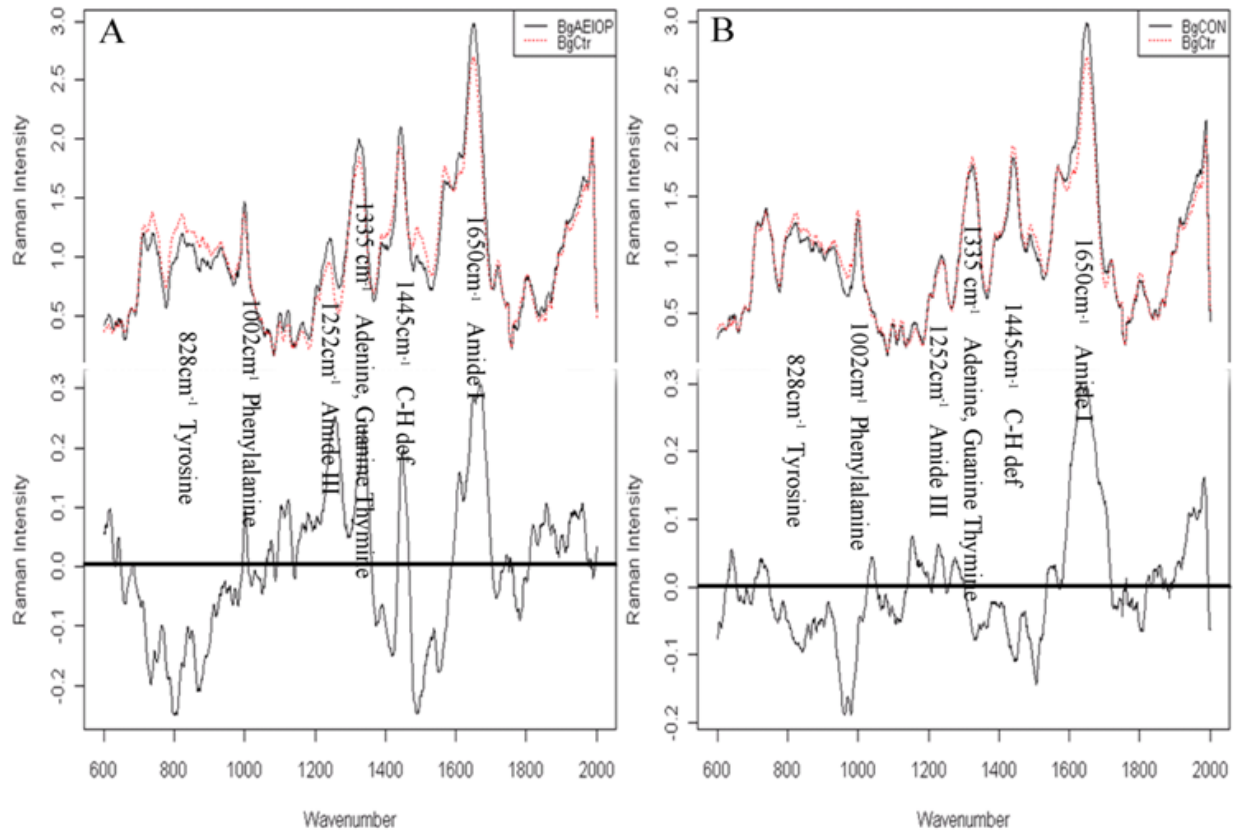
Figure 3.2 Average Raman spectra and difference spectra between glaucomatous and normal RGCs (A). Average spectrum of RGCs from AEIOP beagles and healthy beagles, and the difference spectrum between them; (B). Average spectrum of RGCs from CON beagles and healthy beagles, and the difference spectrum between them. Difference spectra were acquired by subtracting the average spectrum of control (healthy dogs) from the diseased (AEIOP or CON).

3.4.2   Spectroscopic differences between AEIOP/CON beagles and advanced glaucoma in basset hounds

Another interesting comparison is between AEIOP, which mimics acute/early-stage glaucoma, CON, which is a different pathological process although sharing some clinical symptoms with glaucoma, and BaGlau that represents late stage glaucoma in our scenario. The late stage glaucoma spectra were acquired from diseased/control basset hounds reported previously (Wang, Grozdanic et al. 2011). Although the different breeds may introduce

additional variations to the spectral data, it has been shown in our previous work that the diseased/healthy conditions are still the determining factor that dictates the spectral signatures(Wang, Grozdanic et al. 2011).

Figure 3.3 shows the difference spectra of AEIOP, CON and late stage glaucoma (BaGlau). It is clear that the spectroscopic changes in the RGCs associated with late stage glaucoma are more significant than that of the AEIOP/CON RGCs (The intensity changes associated with the disease conditions are three to four times higher in late stage glaucoma comparing to that of AEIOP/CON). At a later stage of disease most RGCs are dead and the remaining RGCs are biochemically different from healthy living RGCs, which may explain the more significant spectroscopic changes. Interestingly, no change is observed for the Amide III peak (1225 cm^{-1}) in late stage glaucoma RGCs, suggesting no significant change in total protein concentration. This suggests that at an early stage of the disease, the RGCs behave differently in terms of protein synthesis. As we know, the spectra reflect the biochemical composition of the cellular milieu at the time of the test. The composition of the milieu depends on the balance between the production and clearance of the "apoptotic" proteins and other molecules. The qualitative differences between the spectra of AEIOP/CON and "late" glaucoma may suggests that in late stage glaucoma there are more significant changes in the protein synthesis pattern and the cumulative accumulation of apoptotic proteins and other molecules in the retina might be the reason for the observed spectroscopic differences. The summation of these changes may potentially be used as spectroscopic markers for the *in vivo* diagnosis of glaucoma.
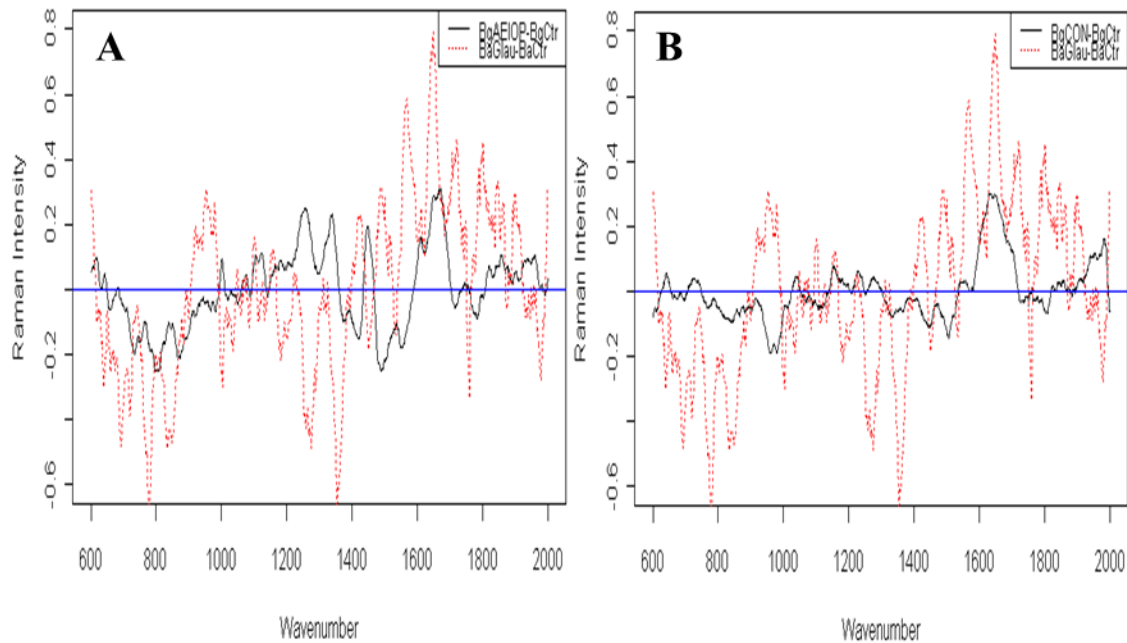
Figure 3.3 Comparison between spectroscopic markers for AEIOP, CON and late-stage close-angle glaucoma.
(A). AEIOP markers vs. Glaucoma markers (B). CON markers vs. Glaucoma markers.

Another interesting observation is the overlap between the AEIOP spectral markers and that of late stage glaucoma in the amino acid fingerprinting regions (700-1200 cm^{-1}), and the lack of such an overlap with the CON spectral markers. Since AEIOP shares many pahtophysiologic features of acute glaucoma, it is reasonable to assume that spectral markers for AEIOP may be good for early stage glaucoma, and function as indicators of risk and susceptibility to the disease.

3.4.3 Discriminant classification using support vector machine

Support Vector Machine (SVM) using Raman spectroscopic features was utilized to generate discriminant classification models to classify a measured spectrum from a retinal tissue sample into groups of two categories (AEIOP and healthy, CON and healthy, AEIOP and CON). 133 spectra measured from the control group (5 healthy beagles), 114 spectra

measured from the 7 AEIOP beagles and 160 spectra measured from 6 CON beagles were used for the discriminant analysis. To construct the discriminant model, the spectra from each category were randomly assigned into ten blocks, and nine blocks were randomly chosen to train the SVM model (the detail of the SVM model was reported elsewhere) (Wang, Grozdanic et al. 2011), while the remaining one blocks were used as validation testing sets. This training-validation cycle was repeated 10 times (10 folded cross-validation). The average classification accuracy was subsequently calculated.

Table 3. 1 shows the classification accuracy for AEIOP/control and CON/control with different numbers of PCs being used in the discriminant models. At 20 PCs, with 87% of the total variance accounted for, the classification accuracy for both AEIOP and CON reached their optimal values (81.2% and 73.3%, respectively). The classification accuracies for the AEIOP samples are consistently better than that for the CON samples, suggesting that the Raman spectral measurements of the RGC cells provided a better characterization of the AEIOP physiological conditions than that of CON cases. To better detect changes associated with CON, different cell types, or a combination of cell types (other than RGCs) in the retinal tissue may need to be characterized.

Table 3.1 Classification accuracy with different PCs used in the discriminant modeling

# of PCs (% of variance)		40(92%)	20(87%)	10(70%)
AEIOP v.s.	AEIOP	74.4%	81.2%	78.7%
Normal	Normal	89.5%	85.9%	60.2%
CON v.s.	CON	71.6%	73.3%	65.5%
Normal	Normal	69.7%	66.4%	61.6%

It is well known that classification models tend to yield high accuracy when the training data and the validation data are acquired from the same sources. For the

spectroscopic screening to become a viable clinical tool, it needs to classify independent samples (not in the training pool) with high accuracy. In this study, we investigated the classification testing with independent validation. The average classification accuracy was then calculated to evaluate the performance of the classification models (Figure 3.4). As expected, the results confirm that an independent validation dataset does lead to a reduction in prediction accuracy. When independent samples (i.e., dogs) are used for the validation tests, individual differences between the validating samples and the samples in the training pool that are not due to diseases would contribute to the discriminant calculation, and result in a less accurate prediction. For AEIOP, the classification accuracy went from 82.1% to 72.6%, and for CON, it went from 73.3% to 63.4%. Since in clinical settings, a new patient will certainly be an "independent" sample that is not currently included in the training pool from which the discriminant model is developed, it is more relevant from a potential application standpoint that the independent validation should be conducted.
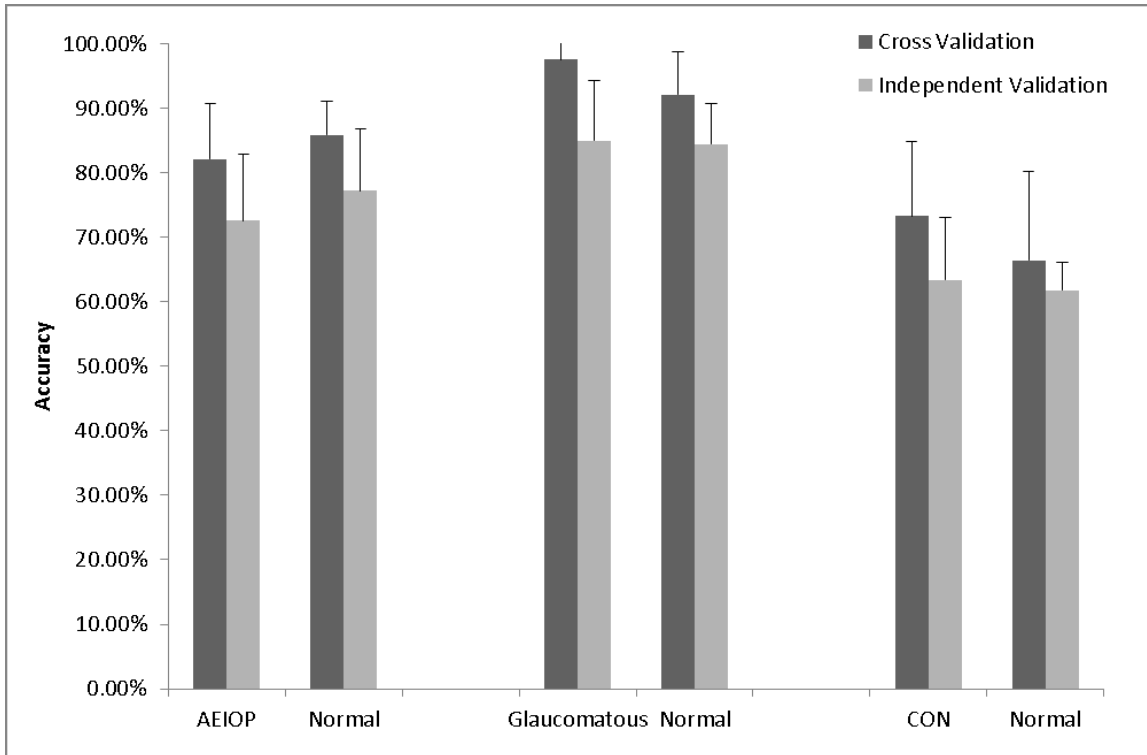
Figure 3.4 Average classification accuracies for RGCs from SVM discriminant model.
to differentiate healthy tissues from AEIOP tissues, CON tissues, and late-stage glaucomatous tissues; validated through cross-validation dataset (training and validation data from same sample pool), and independent validation dataset (training and validation data from same sample pool).

Another observation is that the prediction accuracies for AEIOP and CON are both lower than that for the late stage glaucoma cases (for late stage glaucoma, an average accuracy of 97.6% was reported (Wang, Grozdanic et al. 2011), without taking into account the effect of independent validation. RGCs from retinal tissues of late stage glaucoma dogs are expected to differ more significantly from that of healthy dogs. It was further confirmed by calculating the Euclidean distances for Raman spectra from RGCs between group CON and group control, group AEIOP and group control, group late stage glaucomatous BaGlau and group control in the multidimensional PC space. Longer distance suggests greater separation between the groups. As shown in Figure 3.5, the distance between group late stage glaucomatous and control is the highest, suggesting that most significant differences were

observed between late stage glaucomatous group and the control group. It also shows that the distance between the AEIOP group and the control group is larger than that between the CON group and the control group, which is consistent with the higher classification accuracy for AEIOP samples vs. CON samples (82.1% vs. 73.3%, respectively). The average independent prediction accuracy for AEIOP (72.6%) is a good indicator of the potential prediction accuracy for early-stage glaucoma, which is currently not effectively being diagnosed. In addition, this observation also suggests that AEIOP spectra exhibit more similarity to that of glaucomatous tissues, indicating that AEIOP is a good model to simulate early-stage glaucoma.
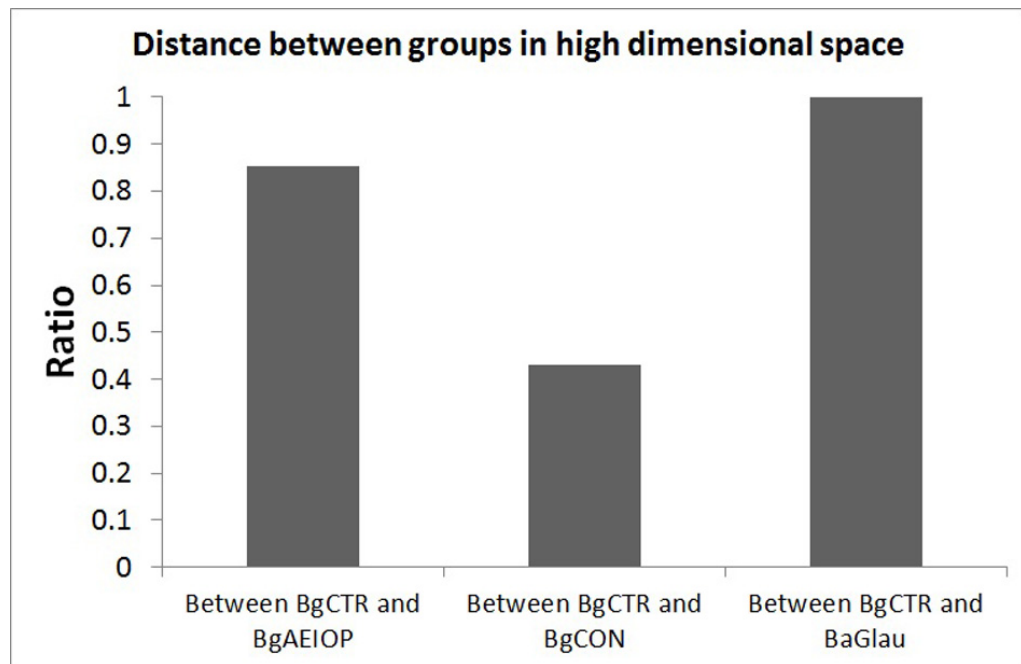
Figure 3.5 Distance between groups in high dimensional space
The Euclidean distances for Raman spectra from RGCs between group CON and group control, group AEIOP and group control, group late stage glaucomatous BaGlau and group control were calculated in 20 dimensional space(1 principal component means one dimension). And the distances were recalibrated by being divided by the distance between group BaGlau and group control.

3.4.4   Limitations and future directions

An interesting observation is the apparent negative correlation between the Raman separation distance of diseased and control groups and the electrophysiological characteristics of the retinal ganglion cells acquired by pattern electroretinography (pERGP). The separation distances between seven AEIOP dogs and the control group (used as Raman predictive score) were calculated. This distance measures the statistical separation between the control group and the AEIOP dogs. However, as shown in Table 3.2 and Figure 3.6, the scores correlate strongly with the pERGP data in a negative fashion. Higher pERG amplitude or ratio suggests healthier RGC cells, hence one would expect a shorter separation between the diseased dog and the control group. However, as shown in Table 3.2 and Figure 3.6, an almost opposite trend is observed. Higher pERG readings are consistent with higher separation distances, with strong correlation indicated by the high R^2 values. Dog #2 has the highest pERG readings, and the largest Raman separation distance in multidimensional PC space as well. Moreover, a strong linear correlation could be established between the Raman separation distances and the pERG ratio between diseased and control dogs, but the pERG amplitude at P50-N95 seems to correlate with the Raman separation distance in a logarithm manner. More study is needed to explain this controversial result. Raman spectra measure the overall chemical compositional characteristics of the RGCs. The PC scores for different dogs with various disease conditions may vary in their contribution to the overall variance. The Raman separation distance in PC space therefore may not be a direct indicator to determine the loss of function in RGCs measured by pERGP. Further characterization of the chemical compositional changes in RGCs associated with the change in pERGP readings is needed for direct identification of Raman spectral peaks that are affected , and vice versa. The pERGP measurements are conducted with living tissues, while the Raman spectra were measured

from fixed tissue samples, which may also complicate the correlations between the pERG readings and the Raman separation distances. Nonetheless, the strong correlation between the pERG readings and the Raman separation distances still suggested that Raman spectra of diseased retinal tissues do capture important signatures that are correlated to the onset and progression of glaucoma-like disease such as AEIOP.

Table 3.2 Pattern electroretinography parameters and calculated Euclidean distance between individual AEIOP beagles to control beagles in 20 PC space

	AEIOP1	AEIOP2	AEIOP3	AEIOP4	AEIOP5	AEIOP6	AEIOP7
pERGP50-N95	2.81	12.4	1.07	2.03	2.51	2.36	0.52
P50op/P50 ctrl (%)	46	89	15.4	44.6	60.19	50.2	15.24
Distance	24.405	50.7	8.235	23.315	31.35	26.28	7.88
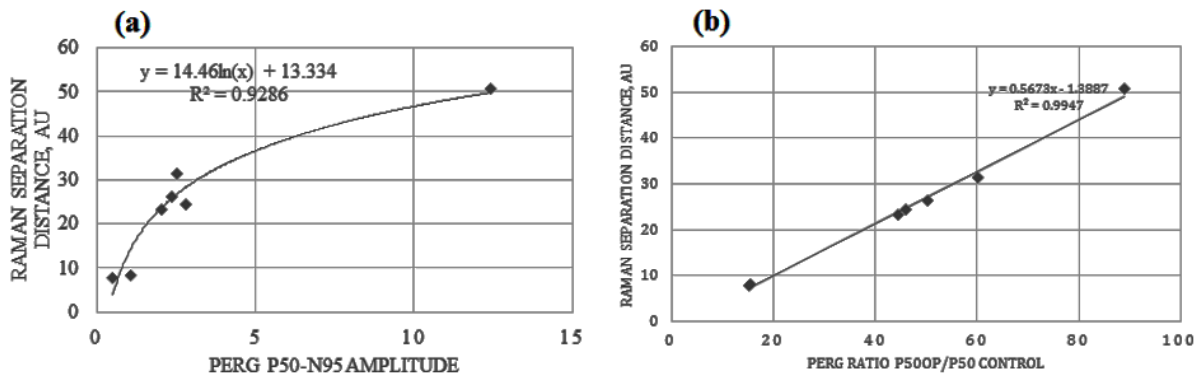
Figure 3.6 Correlations between the pERG data and the Raman separation distance predictor for AEIOP dogs.
(a). Correlation between pERG P50-N95 amplitude and Raman separation distance; (b). Correlation between pERG P50OP/P50 control ratio and Raman separation distance.

In the current study, with the maximum laser exposure time at 99s, the threshold limit value (TLV), which determines the maximum permissible energy exposure to the retina in an in vivo measurement, is 0.82 mW/cm^2. Our power density on sample was 140 mW/cm^2,

significantly higher than the TLV. To utilize Raman spectroscopy for in vivo imaging, the laser power density on the retina has to be greatly reduced without sacrificing the spectral quality. A possible solution would be to utilize pulse laser with extreme short time-gated detection (10^{-12} s). With such short detection time (i.e., laser exposure time), background fluorescence is eliminated (shorter than the fluorescence lifetime so that fluorescence is not developed), and the signal-to-noise ratio of the Raman spectral measurement can be significantly improved, and much weaker Raman signals will become detectable (Tahara and Hamaguchi 1993; Matousek, Towrie et al. 1999). Extremely short detection time also allows a much higher laser power to be applied without increasing the overall laser energy that the retina is exposed to. A simple calculation reveals that at 10^{-12} exposure time, the TLV is 2601 mW/cm^2, well beyond what was being used in this study.

Another limitation of our study is the fact that we are looking at an acute and a substantial loss of retinal tissue, particularly in the AEIOP animals. This is most likely resulting in more severe damage and dysfunctional RGCs in the retinal tissues than in the case of early stage glaucoma. In a more typical clinical scenario in which a Raman system is hoped to help, open angle glaucoma is a more chronic disease with a much smaller number of RGCs being lost at any particular time, leading to a less differentiable Raman spectral signal that needs to be distinguished from that of normal tissues.

3.5 Conclusions

In this study, we explore the potential of using Raman spectroscopy for early detection and characterization of glaucoma-like pathological anomalies. Spectroscopic markers related to changes in intracellular protein compositions associated with glaucoma-like anomalies of retinal ganglion cells were identified. 72.6% classification accuracy was

achieved to identify AEIOP, a close mimic of early-stage/acute glaucomatous damage, from independent canine retinal tissues. Potentially, Raman spectroscopy in combination with time-gated pulsed laser excitation can be utilized for *in vivo* Raman imaging of retina and provide early detection and diagnosis for glaucoma.

3.6 Acknowledgments

3.7 References

Bach, M. and M. B. Hoffmann (2008). "Update on the pattern electroretinogram in glaucoma." Optometry & Vision Science **85**(6): 386-395.

Bellezza, A. J., C. J. Rintalan, et al. (2003). "Deformation of the lamina cribrosa and anterior scleral canal wall in early experimental glaucoma." Investigative Ophthalmology & Visual Science **44**(2): 623.

Bernstein, P. S., D. Y. Zhao, et al. (2004). "Resonance Raman measurement of macular carotenoids in the living human eye." Archives of Biochemistry and Biophysics **430**(2): 163-169.

Bocklitz, T., A. Walter, et al. (2011). "How to pre-process Raman spectra for reliable and stable models?" Analytica Chimica Acta **704**(1-2): 47-56.

Boskey, A. L. and R. Mendelsohn (2005). "Infrared spectroscopic characterization of mineralized tissues." Vibrational Spectroscopy **38**(1-2): 107-114.

Gelatt, K. (1977). "Animal models for glaucoma." Investigative Ophthalmology & Visual Science **16**(7): 592.

Gellermann, W. (2002). "Raman imaging of human macular pigments." Optics Letters **27**(10): 833-835.

Girkin, C. A. (2005). "Compressive optic neuropathy." Neuro-ophthalmology: the practical guide: 217.

Grozdanic, S. D., H. Kecova, et al. (2010). "Functional and structural changes in a canine model of hereditary primary angle-closure glaucoma." Investigative Ophthalmology & Visual Science **51**(1): 255.

Grozdanic, S. D., M. Matic, et al. (2007). "Recovery of canine retina and optic nerve function after acute elevation of intraocular pressure: Implications for canine glaucoma treatment." Veterinary Ophthalmology **10**: 101-107.

Herrero, A. M. (2008). "Raman spectroscopy for monitoring protein structure in muscle food systems." Critical Reviews in Food Science and Nutrition **48**(6): 512-523.

Holder, G. E., M. G. Brigell, et al. (2007). "ISCEV standard for clinical pattern electroretinography—2007 update." Documenta ophthalmologica **114**(3): 111-116.

Huang, Z., H. Lui, et al. (2005). "Raman spectroscopy in combination with background near infrared autofluorescence enhances the *in vivo* assessment of malignant tissues." Photochemistry and Photobiology **81**(5): 1219-1226.

Jimenez, L. O. and D. A. Landgrebe (1998). "Supervised classification in high-dimensional space: Geometrical, statistical, and asymptotical properties of multivariate data." Systems, Man, and Cybernetics, Part C: Applications and Reviews, IEEE Transactions **28**(1): 39-54.

Karatzoglou, A., D. Meyer, et al. (2005). "Support vector machines in R."

Kerrigan–Baumrind, L. A., H. A. Quigley, et al. (2000). "Number of ganglion cells in glaucoma eyes compared with threshold visual field tests in the same persons." Investigative Ophthalmology & Visual Science **41**(3): 741-748.

Knudsen, L., C. Johansson, et al. (2002). "Natural variations and reproducibility of *in vivo* near infrared fourier transform Raman spectroscopy of normal human skin." Journal of Raman Spectroscopy **33**(7): 574-579.

Ko, A. C. T., L. Choo-Smith, et al. (2006). "Detection of early dental caries using polarized Raman spectroscopy." Optics Express **14**(1): 203-215.

Koljenovi , S., T. C. B. Schut, et al. (2005). "Tissue characterization using high wave number Raman spectroscopy." Journal of Biomedical Optics **10**: 031116.

Krafft, C. and V. Sergo (2006). "Biomedical applications of Raman and infrared spectroscopy to diagnose tissues." Spectroscopy **20**(5): 195-218.

Kruger, E. F., G. Minko, et al. (2003). "Detection of glutamate in the eye by Raman spectroscopy." Journal of Biomedical Optics **8**: 167.

Matousek, P., M. Towrie, et al. (1999). "Efficient rejection of fluorescence from Raman spectra using picosecond Kerr gating." Applied Spectroscopy **53**(12): 1485-1489.

Morrison, J. C. (2005). "Elevated intraocular pressure and optic nerve injury models in the rat." Journal of Glaucoma **14**(4): 315.

Quigley, H. A. (1999). "Neuronal death in glaucoma." Progress in Retinal and Eye Research **18**(1): 39-57.

Schut, T. C. B., M. Witjes, et al. (2000). "*In vivo* detection of dysplastic tissue by Raman spectroscopy." Analytical Chemistry **72**(24): 6010-6018.

Sebag, J. (2004). "Seeing the invisible: the challenge of imaging vitreous." Journal of Biomedical Optics **9**: 38.

Shafer Peltier, K. E., A. S. Haka, et al. (2002). "Raman microspectroscopic model of human breast tissue: Implications for breast cancer diagnosis *in vivo*." Journal of Raman Spectroscopy **33**(7): 552-563.

Shim, M. G., L. M. Wong Kee Song, et al. (2000). "*In vivo* near infrared Raman spectroscopy: Demonstration of feasibility during clinical gastrointestinal endoscopy?" Photochemistry and Photobiology **72**(1): 146-150.

Sijtsema, N. M., J. J. Duindam, et al. (1996). "Imaging with extrinsic Raman labels." Applied Spectroscopy **50**(5): 545-551.

Tahara, T. and H. O. Hamaguchi (1993). "Picosecond Raman spectroscopy using a streak camera." Applied Spectroscopy **47**(4): 391-398.

Van de Poll, S., K. Kastelijn, et al. (2003). "On-line detection of cholesterol and calcification by catheter based Raman spectroscopy in human atherosclerotic plaque *ex vivo*." Heart **89**(9): 1078.

Wang, Q., S. D. Grozdanic, et al. (2011). "Exploring Raman spectroscopy for the evaluation of glaucomatous retinal changes." Journal of Biomedical Optics **16**(10): 107006.

Wang, Q., S. D. Grozdanic, et al. (2011). "Exploring Raman spectroscopy for the evaluation of glaucomatous retinal changes." Journal of biomedical optics **16**: 107006.

Witten, I. H. and E. Frank (2005). Data Mining: Practical Machine Learning Tools and Techniques. Burlington, MA, USA, Morgan Kaufmann.

Zhao, J., H. Lui, et al. (2007). "Automated autofluorescence background subtraction algorithm for biomedical Raman spectroscopy." Applied Spectroscopy **61**(11): 1225-1232.

Chapter 4.   RAPID DETERMINATION OF PORK SENSORY QUALITY USING RAMAN SPECTROSCOPY

Qi Wang[1], Steven M. Lonergan[2], Chenxu Yu[1]

[1]Department of Agricultural and Biosystems Engineering, Iowa State University, Ames, Iowa, 50011
[2] Department of Animal Science, Iowa State University, Ames, Iowa, 50011

4.1 Abstract

Existing objective methods to predict sensory attributes of pork in general do not yield satisfactory correlation to panel evaluations, and their applications in meat industry are limited. In this study, a Raman spectroscopic method was developed to evaluate and predict tenderness, juiciness and chewiness of fresh, uncooked pork loins from 169 pigs. Partial Least Square Regression models were developed based on Raman spectroscopic characteristics of the pork loins to predict the values of the sensory attributes. Furthermore, binary barcodes were created based on spectroscopic characteristics of the pork loins, and subjected to multivariate statistical discriminant analysis (i.e., Support Vector Machine) to differentiate and classify pork loins into quality grades ("good" and "bad" in terms of tenderness and chewiness). Good agreement (>83% correct predictions) with sensory panel results was obtained. The method developed in this report has the potential to become a rapid objective assay for tenderness and chewiness of pork products that may find practical applications in pork industry.

4.2 Introduction

Quality of fresh pork is often defined by appearance and by sensory attributes from a consumer standpoint. While consumers can readily see color, firmness and marbling

attributes in a fresh pork chop, the sensory quality of a pork chop is more difficult to evaluate. Tenderness, chewiness and juiciness are among the more important sensory attributes of fresh meat(Mennecke, Townsend et al. 2007). The deviation in their quality experienced by consumers is a barrier to ensure demand for high quality fresh pork. Tenderness, chewiness and juiciness of fresh cooked pork are difficult to predict, though it is understood that pH(Bee, Anderson et al. 2007; Lonergan, Stalder et al. 2007), postmortem aging(Melody, Lonergan et al. 2004; Zhang, Lonergan et al. 2006) and marbling (Lonergan, Stalder et al. 2007) all contribute to tenderness of fresh pork. However, a robust objective method to rapidly evaluate and predict fresh pork sensory attributes remains to be developed.

To this date, the best evaluation methods of sensory attributes which provide the most accurate prediction of customer responses are through sensory panels. The reason is obvious: panels comprised human beings, whose evaluation best mimics general human responses. However, sensory panel evaluations are costly and time consuming. It is not possible to use it as routine quality assurance method in meat production. There is a great need for a rapid, non-destructive analysis technique that can be used to predict consumer responses.

Since tenderness and chewiness are primarily mechanical characteristics of cooked meat, a considerable number of studies have been conducted to investigate the correlations between them and physically measured properties (i.e., shear force, stress and strain response curves). Some reports showed strong correlations between mechanical properties (mainly Warner-Bratzler shear tests) of meat (i.e., beef) and the tenderness(Jeremiah and Phillips 2000), yet others suggested that only weak correlations could be established(Chan, Walker et al. 2002). Juiciness on the other hand is defined as the amount of perceived juice that is

released from the meat during mastication, which is related to the water holding capacity of the meat and its fat content(Fox, Wolfram et al. 1980; Huff-Lonergan and Lonergan 2005).

Meat tenderness, in general, is affected to a small degree by lipid composition(Rincker, Killefer et al. 2008), but a much greater proportion of the variation in tenderness is determined by the protein component and the structures that are made primarily of proteins in the connective tissue component as well as the myofibrillar component. The content of connective tissue explains difference in pork tenderness(Wheeler, Shackelford et al. 2000) especially when considerations across muscles are made. Importantly, changes in protein solubility(Barbut, Sosnicki et al. 2008; Kim, Huff-Lonergan et al. 2010; Kim, Lonergan et al. 2010), protein degradation(Melody, Lonergan et al. 2004; Huff Lonergan, Zhang et al. 2010), protein cross-linking(Kim, Huff-Lonergan et al. 2010) and protein nitrosylation (Huff Lonergan, Zhang et al. 2010) all contribute to differences in pork tenderness. In many cases, the rate and extent of postmortem pH decline are important determinants of some of these changes(Lonergan, Stalder et al. 2007; Barbut, Sosnicki et al. 2008). Unfortunately, in some cases, rapid, accurate determination of these features is difficult and costly. Development of a method to measure the changes in protein modifications in meat is a critical need to predict tenderness in fresh pork.

Near infrared (NIR) spectroscopy has been utilized by many groups as a method to quickly evaluate the biochemical characteristics of meats and their correlations to sensory attributes(Mitsumoto, Maeda et al. 1991; Park, Chen et al. 1998; Rodbotten, Mevik et al. 2001; Venel, Mullen et al. 2001; Liu, Lyon et al. 2003). However, in NIR spectroscopy, the overtones of fundamental molecular vibration modes are being measured which are often overlapped to yield broad bands that do not provide high resolution spectroscopic fingerprints

of different molecular functional groups, which subsequently limits the accuracy of the biochemical profiling of the meat. Mid-infrared Fourier Transform (FT-IR) spectroscopy has also been explored for meat characterization(Böcker, Ofstad et al. 2006). Although FT-IR yields high-resolution spectroscopic profiles for meat samples, it suffers from strong interference from omnipresent water in the meat samples.

Raman spectroscopy is another alternative vibrational spectroscopic method that has a considerable number of advantages compared to other food analysis techniques (Vapnik and Chervonenkis 1964; Beattie, Bell et al. 2004; Beattie, Bell et al. 2008). It is a noninvasive spectroscopic technique providing in situ information about the composition and structure of proteins and lipids, which are main components of pork (Beattie, Bell et al. 2004; Beattie, Bell et al. 2008; Herrero 2008). Raman spectroscopy is relatively insensitive to water and hence does not suffer from water interference, which is a severe problem in mid-IR spectroscopy like FT-IR, since foods commonly contain ≥75% water. In addition, it does not require any sample preparation and is nondestructive while at the same time providing high-resolution, detailed spectral information about the chemical composition of the sample.

Raman spectroscopy has been explored to predict the sensory quality of beef rounds(Beattie, Bell et al. 2004) and changes in pork properties during cooking and aging (Beattie, Bell et al. 2008). A relatively good correlation between Raman data and sensory panel's ratings of acceptability of texture and degree of tenderness was reported. However, previous studies did not establish a working model for classifying meats into pre-determined tenderness and/or chewiness categories that potentially can be used in a meat processing plant(Beattie, Bell et al. 2004).

Partial Least Square Regression (PLSR) is a commonly used method to model a response variable when there are a large number of predictor variables, known as components, as linear combinations of the original predictor variables, which has been widely applied in correlating spectroscopic characteristics to sensory attributes (Mitsumoto, Maeda et al. 1991; Park, Chen et al. 1998; Rodbotten, Mevik et al. 2001; Venel, Mullen et al. 2001; Liu, Lyon et al. 2003; Beattie, Bell et al. 2004; Beattie, Bell et al. 2008). Support Vector Machine (SVM) belongs to a new generation of machine learning system based on recent advances in statistical learning theory(Steinwart and Christmann 2008) for classification or regression. It is an extension to nonlinear models of the generalized portrait algorithm developed by Vladimir Vapnik (Cristianini and Shawe-Taylor 2000; Ben-Hur, Horn et al. 2002). The SVM algorithm is based on the statistical learning theory and the Vapnik-Chervonenkis (VC) dimension introduced by Vladimir Vapnik and Alexey Chervonenkis (Vapnik and Chervonenkis 1964). It is particularly suitable to separate two distinguishable groups. In SVM, input data are viewed as two sets of vectors in an n-dimensional space, an SVM will construct a separating hyper plane in that space, one which maximizes the margin between the two datasets. To calculate the margin, two parallel hyper planes are constructed, one on each side of the separating hyper plane. Intuitively, a good separation is achieved by the hyper plane that has the largest distance to the neighboring data points of both classes, since in general the larger the margin, the better the classification.

Our objectives were to determine the utility of using uncooked loin chop Raman Spectra data to predict sensory quality of pork loin chops. To achieve this objective, we investigated the correlations between Raman spectroscopic characteristics of uncooked pork loin chops and the corresponding sensory attributes of cooked chops (i.e., tenderness,

chewiness and juiciness). Additionally we developed Partial Least Square Regression models to predict the sensory quality of cooked pork loin chops based on the Raman spectroscopic characteristics of the uncooked chops. Furthermore, we developed a Raman spectroscopic binary barcoding method in conjunction with Support Vector Machine modeling to classify the sensory tenderness and chewiness of fresh pork loins, with excellent accuracy (>83%) for selection of the pork samples with tenderness/chewiness values at the two extreme ends. Potentially the Raman method can serve as selection tools to quickly screen and separate high quality (very tender) and low quality (very tough) meat during the meat processing.

4.3 Materials and Methods

4.3.1 Animals and sample collection

This experiment utilized pork loins from a project designed to determine the influence of selection for reduced residual feed intake on swine growth, pork composition and pork quality(Smith, Gabler et al. 2011). The boneless loins were removed from the carcass at 24 h postmortem, vacuum packaged, and were transported to the ISU Meat Laboratory on the same day. Boneless center loins (10th–12th thoracic vertebrae, n = 169; 2 d postmortem) were separated into 2.5 cm chops at the ISU Meat Laboratory. Loin chops that were to be used for sensory and star probe analyses(Lonergan, Stalder et al. 2007) were vacuum-packed and held for 7 to 10 d postmortem at 4 °C. Samples to be used for Raman measurement were vacuum packaged and held at 4 °C until they were frozen at 2 d postmortem.

4.3.2 Meat sensory quality and star probe value assessments

Star probe values and sensory quality scores were determined on cooked pork loin chops. Chops aged 7–10 d postmortem were cooked on clamshell grills to an internal temperature of 70 °C. The temperature of each chop was monitored individually using

thermocouples (Omega Engineering, Inc., Stamford, CT). The chops were cooled to room temperature prior to analysis(Lonergan, Stalder et al. 2007). A circular, five-pointed star probe that measures 9 mm in diameter with 6 mm between each point was attached to an Instron Universal Testing Machine (Model 5566, Instron, Norwood, MA). Each chop was punctured at a crosshead speed of 3.3 mm/s.

Chops cooked to an internal temperature of 70 °C were prepared for sensory analysis by an existing trained sensory(Lonergan, Stalder et al. 2007). This panel routinely evaluates fresh pork loin traits of tenderness, chewiness, and juiciness. Panelists had 2 one-hour orientation sessions to include the diversity of quality expected in this experiment. Cooked pork chops were evaluated for sensory tenderness, chewiness, and juiciness. A 15-cm line scale was used (0 = not tender, chewy, juicy; 15 = very tender, chewy, juicy) to evaluate sensory traits for all chops. Sensory data were recorded using a computerized sensory software system (Compusense five 4.6, Compusense, Inc., Guelph, Ontario, Canada). During each session, four panelists evaluated each pork loin chop. The same four panelists were used throughout the entire study.

4.3.3 Sample preparation and Raman measurements

Each pork sample was stored at −20 °C individually. They were fully thawed at ambient temperature before measurement. Raman measurements were performed using a DXR Dispersive Raman Microscope (Thermo Scientific, Inc., Madison, WI) with 780 nm, 14 mW excitation laser at ambient temperature. Raman spectra were collected with 2 s exposure time from 400 to 2000 cm^{-1} at a resolution of 1 cm^{-1}. The pork samples were placed directly on glass slides at the focus of the laser beam with no pretreatment. In each measurement, the excitation laser was focused (a ~ 1 mm diameter spot) onto 15 randomly

selected locations on the pork chop, and the 15 collected spectra were averaged to yield one spectrum of the pork sample to minimize variations inside the pork chop. Ten spectra were acquired for each pork sample following this protocol and were used in discriminant analysis.

4.3.4   Spectral data processing

All spectra were automatically baseline corrected and smoothed using a 5-point averaging smoothing algorithm to reduce the baseline variability at the region between 400 cm^{-1} and 2000 cm^{-1} and normalized using Omnic professional Software Suite (Thermo Scientific, Inc., Madison, WI). The spectra were then normalized against the maximum Raman peak (i.e., the intensity of the maximum Raman peak was set to 1), and the first and second derivatives of the Raman peak intensities versus wave numbers were calculated and used for generating the binary barcodes. Correlations between Raman spectral data (Raman intensity at each wave number for all 169 pork samples) and sensory attribute readings (panel values) were calculated. Partial Least Square Regression was also conducted to compress the dimension of the spectral data (1661 wave numbers) into 20 PLS components, and correlations between the sensory attribute values to each PLS component were also calculated to identify the PLS components that are more responsible for generating the variance in the sensory attributes.

Raman peaks are represented by their wave number (Raman shift) and intensity. The peak intensities are dependent on many factors that may vary from sample to sample (i.e., sample size, exposure time, etc.), but their Raman shift remains identical as long as the molecular makeup is the same. Therefore, in this study we developed a binary barcode to eliminate variations in the spectral data due to peak intensities, and highlight the unique Raman shift fingerprints of each sample. The binary barcode approach was originally

proposed by Patel, Premasiri, Moir, and Ziegler(Patel, Premasiri et al. 2008) to differentiate microorganisms based on their Raman spectroscopic signatures, in this study a similar approach was developed to improve the classification accuracy for pork loins.

The binary barcodes were generated based on the second derivative spectra in the 400 cm^{-1} to 2000 cm^{-1} range. A binary value (0 or 1) was assigned to each calculated second derivative spectral data point primarily based on the sign of the second derivative, i.e., 1 for positive second derivatives (upward curvature), and 0 for negative second derivatives (downward curvature). Furthermore, a threshold for zero was set at 6% of the maximum absolute value of the second derivative for positive second derivative readings (for all absolute values larger than the threshold, 1 was retained; otherwise it was switched to 0). This threshold helps discriminate against residual noise components. Contribution to the measured spectra from low level background noises was thus removed by assigning 0 to it. Remaining 1 s represents contributions to the measured spectra from relevant meat samples. The threshold value (6%) was determined experimentally by finding the barcodes that provided the best prediction for the sensory attributes. for the SVM model. The main goal is to predict sensory attributes (i.e., tenderness and chewiness) that are at the two ends of the panel evaluation spectrum. The 169 pork loin samples were divided into 3 groups according to the value of specific sensory attributes and/or star probe values. One calibration set and one test set were set in such a way that both the calibration set and the test set showed approximately the same distribution of one specific variable. Different calibration samples were chosen randomly to calculate the average classification accuracy (over 10 random sampling). Chemometric analysis was conducted using both WinDas (Wiley & Sons, Chichester, UK, 1998 version) and Matlab (The MathWorks, Natick, MA) software.

4.4 Results and Discussion

4.4.1 Sensory tenderness, star probe, sensory chewiness, and sensory juiciness

Values of sensory tenderness, chewiness, juiciness and star probe vary significantly between samples, as shown in Figure 4.1. Star probe values were negatively correlated to sensory tenderness scores, which was in agreement with earlier report (Lonergan, Stalder et al. 2007).
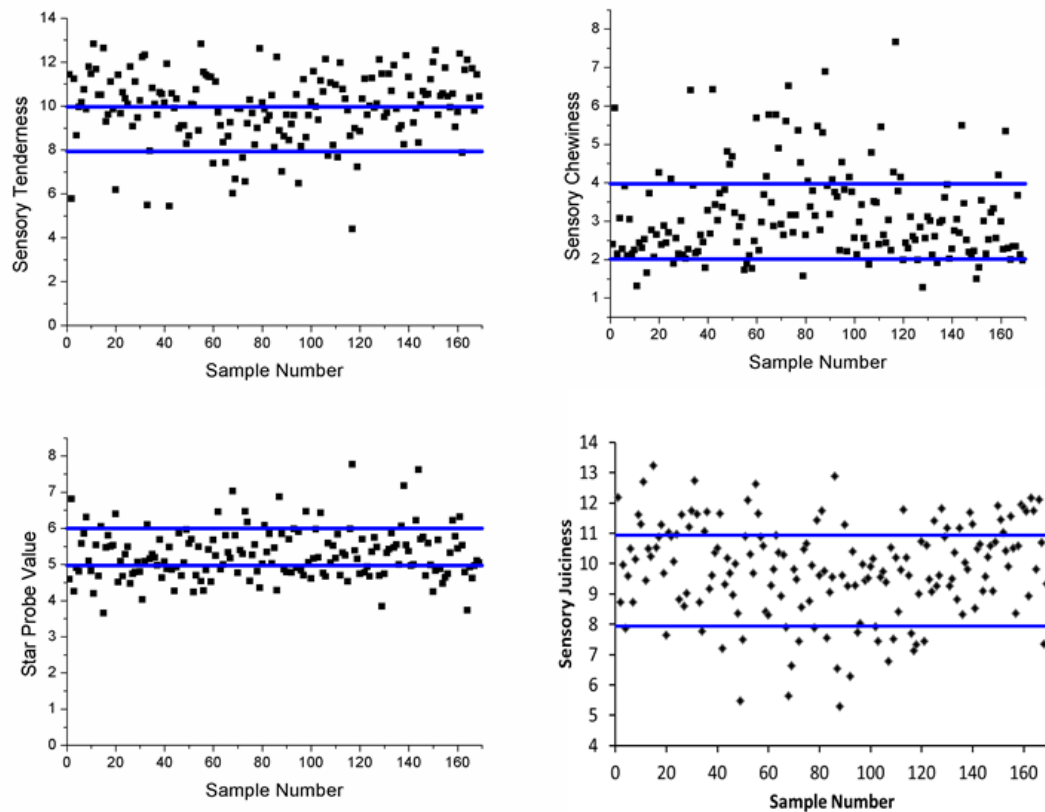
Figure 4.1 Sensory tenderness (A), sensory chewiness (B), sensory juiciness (C) and star probe (D) for 169 pork samples.

Tenderness was determined on a scale of 0–15; the range was 4 to 13 with higher scores representing greater tenderness. Chewiness was determined on a scale of 0–10; the range was between 1 and 9 with higher scores representing greater chewiness. Juiciness was determined on a scale of 0–15; the range was between 4 and 14 with higher scores representing greater juiciness.

Since one of the primary goals is to correctly predict pork samples that fall into the two extreme ends of their sensory texture attributes (e.g., tenderness and chewiness), we

divided the samples into three groups based on their sensory texture attributes: high quality (tenderness score > 10, chewiness score < 2), medium quality (10 > tenderness score > 8, 4 > chewiness score > 2) and poor quality (tenderness score < 8, chewiness score > 4).

4.4.2 Raman spectroscopic analysis

Typical Raman spectra of pork samples in the 400-2000 cm $^{-1}$ region are shown in Figure 4.2. Baseline correction, smoothing and normalization were applied to reduce background noises. The wavenumber and intensity changes in the Raman bands were indicative of changes in the secondary and tertiary structures and variations in local environments of meat proteins, which in turn determine the characteristics/properties of the meat. The Raman band centered near 1653 cm $^{-1}$ (Figure 4.2), represents amide I band which is an indicator of the overall concentration of proteins(Herrero 2008).
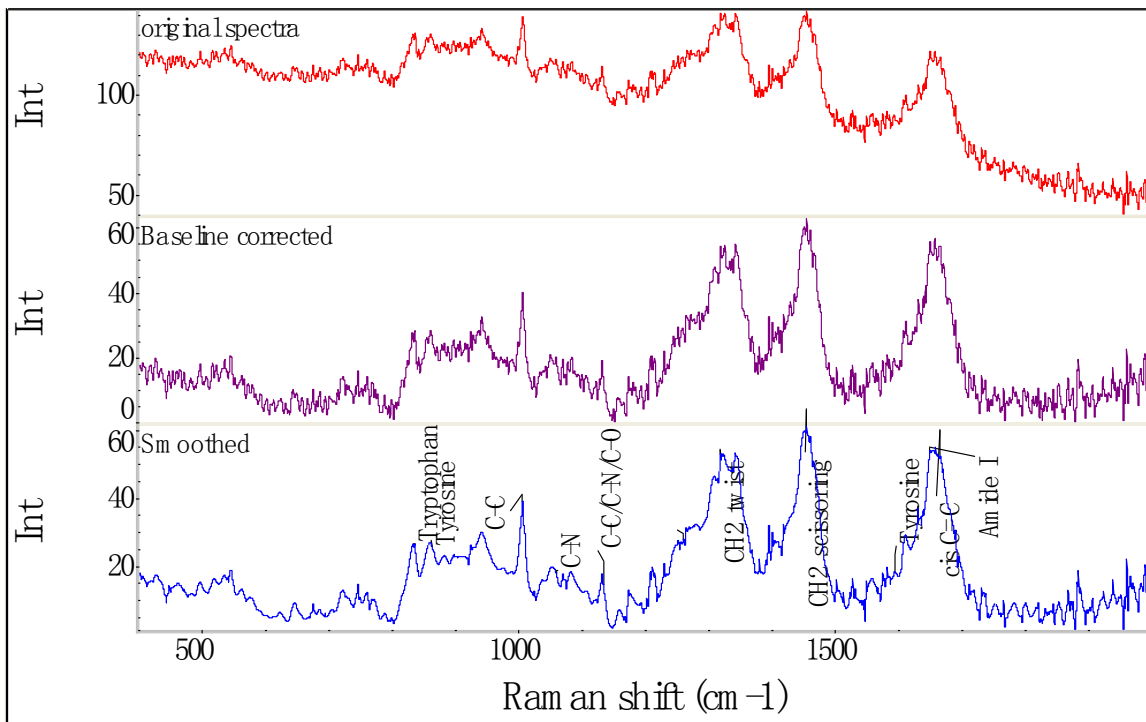

Figure 4.2 Typical Raman spectra of pork loins (original, baseline corrected and smoothed).

The Pearson correlation coefficients between each of the well-modeled sensory attributes (tenderness, chewiness and juiciness) and Raman intensity at each wave number of all spectra of 169 samples were calculated and shown in Figure 4.3. In general, Raman intensities are only moderately correlated to the sensory attributes; it is understandable, sensory attributes are complex, subjective factors; they cannot be directly explained by physically measured parameters. Another interesting observation was that the correlations between tenderness and juiciness and Raman spectral data showed very similar patterns, which were very different from the pattern of the correlation between chewiness and Raman spectral data. It suggests that variations in tenderness and juiciness may have similar biochemical/ compositional origin (i.e., protein structure, protein components and structures that determine water holding capacity), while the underlying determining factor for chewiness (connective tissue amount/structure around the muscle fibers) may have a different biochemical explanation. Further investigation is necessary to better understand these observations.
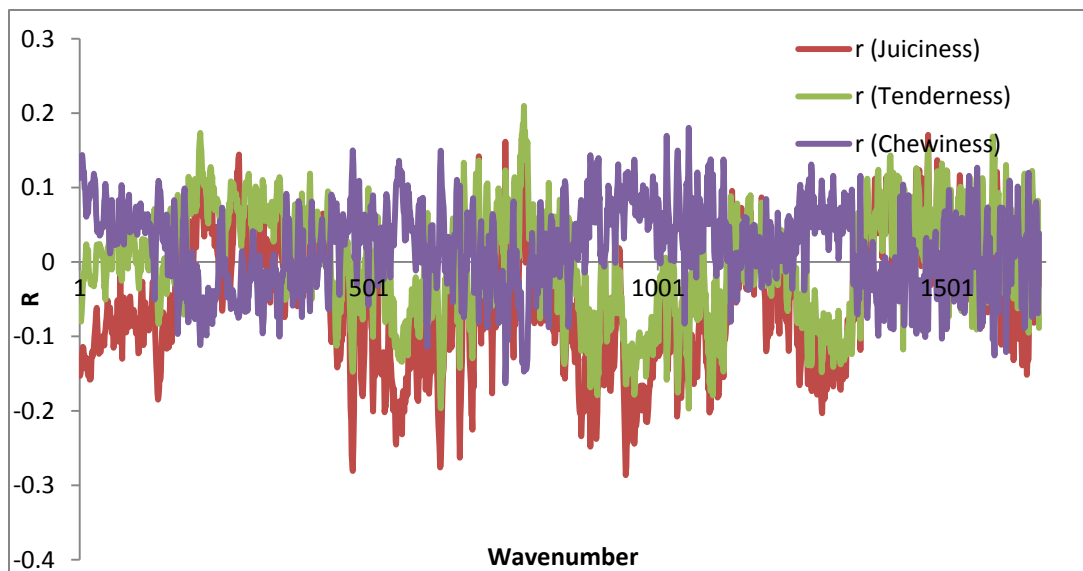

Figure 4.3 Pearson correlation coefficients (r) between Raman spectral data and sensory attributes (tenderness, chewiness and juiciness) (N = 169 samples).

4.4.3 Predication of sensory tenderness, chewiness and juiciness values based on PLS regression model

The first 20 PLS components were calculated from the Raman spectral data, more than 95% of the variances could be accounted for by the first 10 PLS components. The Pearson correlation coefficients between PLS components and sensory attributes calculated, and the first 10 PLS components are more strongly correlated to the sensory attributes than the original spectra. Hence, the first 10 PLS components were used for regression model development.

To develop the regression model, spectra of 117 pork samples (70% of total samples) were randomly selected as a training set. The remaining 52 pork samples were designated as the validation/testing set. The PLSR model and the testing results were illustrated in Figure 4.4, good linear regression models were established between the PLS components and all three sensory attributes ($R^2 = 0.986$ for tenderness and chewiness, 0.982 for juiciness). Table 4.1 shows the validation results. For an error tolerance of 25% (i.e., predicted value = (1.0 ± 0.25) × observed value), the prediction accuracy is 82.7%, 43.8% and 82.7%, for tenderness, chewiness and juiciness, respectively; for an error tolerance of 10% (predicted value = (1.0 ± 0.1) × observed value), the prediction accuracy is 40.8%, 21.1% and 43.8%, respectively. For an error tolerance of 5% (predicted value = (1.0 ± 0.05) × observed value), the prediction accuracy is 23.2%, 9.6% and 17.3%, respectively. The prediction accuracy for chewiness is significantly lower than that for tenderness and juiciness. Sensory tenderness is directly correlated to the proteins in the connective tissue component as well as the myofibrillar component of the meat, while sensory juiciness is related to the water holding capacity of the meat, which is also primarily dependent on the protein structures/compositions of the muscle fibers and connective tissues(Kim, Huff-Lonergan et al. 2010). The chewiness is primarily

dependent on the amount and structures of the connective tissues. The significant discrepancy in prediction accuracy between tenderness/juiciness and chewiness suggests that Raman spectroscopic signatures of meat may be more closely related to the protein composition/structures of the myofibrillar component than that of connective tissues. More investigation is needed for further understanding. The standard deviations of the sensory panel values were around 5%, the prediction accuracy of the PLS model based on Raman spectral data was hence significantly deviated from the sensory panel results. However, to predict consumer responses to a meat product, it may not be necessary to know the precise sensory panel values. If a prediction can be acquired that distinguishes the extreme cases (i.e., very good quality vs. very poor quality) with good reliability, such prediction would be beneficial to a meat producer to classify its meat products. Therefore, we further developed a new classification model using Raman spectral data to differentiate and classify pork loins based on their sensory attribute grades. The sensory attributes we investigated were sensory tenderness and chewiness.
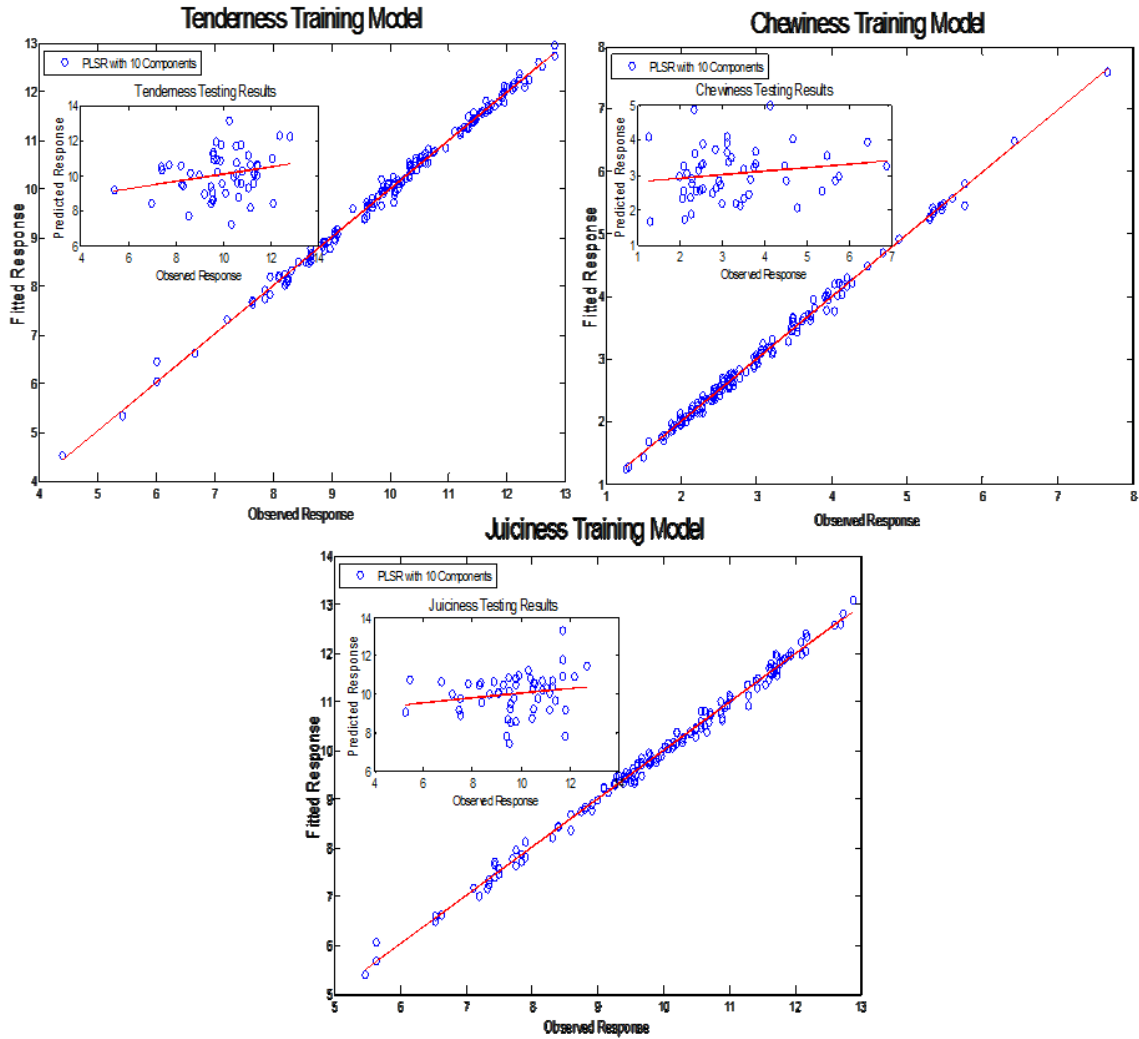
Figure 4.4 PLS Regression models and testing plots (inlets) for the prediction of sensory attributes of the pork loins using Raman spectroscopy (A: tenderness, B: chewiness and C: juiciness).

Table 4.1 Accuracy of the PLS regression prediction for sensory tenderness, chewiness and juiciness with different error tolerance.

Error tolerance	±25%	±10%	±5%
Tenderness	82.7%	40.8%	23.2%
Chewiness	43.8%	21.1%	9.6%
Juiciness	82.7 %	43.8%	17.3%

4.4.4   Discretization of spectra for classification

In spectroscopic data processing, first and second derivatives are routinely calculated to remove slowly varying background noises which otherwise would contribute non-essential variances to the subsequent statistical analysis. First derivative spectra avoid contributions resulting from fluctuations in spectral background, but are still sensitive to Raman vibration intensity fluctuations. Second derivative spectra similarly minimize background variability and tend to further reduce sensitivity to intensity fluctuations. Furthermore, the signs of the second derivatives, indicating the locations of peaks and valleys, are found to be extremely robust identification features with minimal variability in replicated measurements. The binary barcodes (with a 6% threshold) calculated from these signs of second derivatives further eliminated signal fluctuations due to all the sources of intensity variations.

The selection of a threshold was determined through investigation of the optimal threshold value that would yield the best classification accuracy. Threshold values of 0–24% of the maximum second derivatives were investigated, and 6% was identified as the optimal value to retain the most information that yielded the best classification results. It was used throughout the study.

4.4.5   Classification of pork loins by sensory tenderness and sensory chewiness

A primary question was to determine if Raman spectroscopic characteristics could be used to classify pork loins into three distinguishable quality grade groups (good, medium, poor) as defined by their tenderness or chewiness values. As shown in Figure 4.5, using the binary barcodes for each pork samples, with canonical variant analysis, a classification based on tenderness (Figure 4.5A) and chewiness (Figure 4.5B) was achieved that demonstrated three well-separated groups for each quality category. The successful classification shows

that the Raman spectroscopic binary barcodes for different pork samples are uniquely

correlated to their sensory attributes.
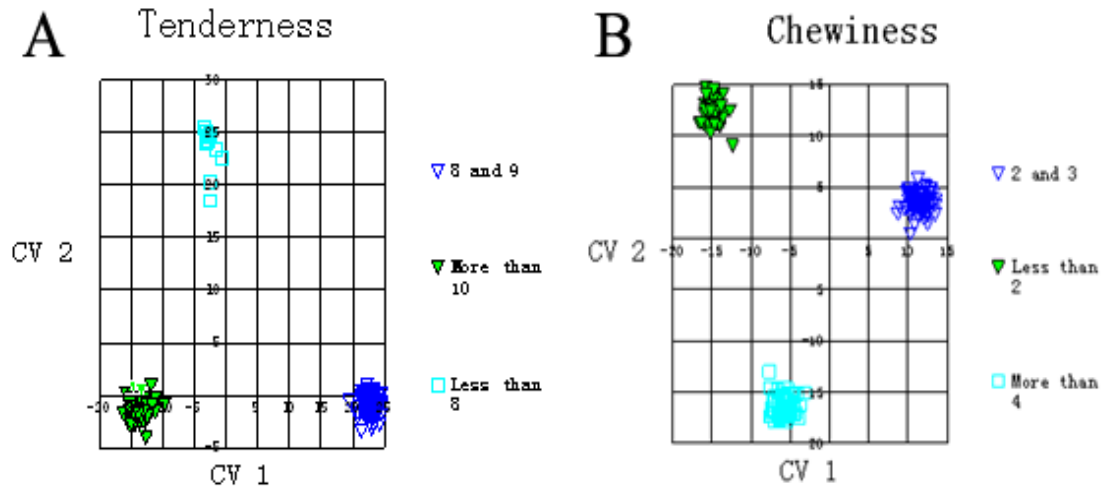
Figure 4.5 Classification of pork loins into three quality categories based on their Raman
spectroscopic barcodes and sensory panel classifications.
A. Left panel: for tenderness; B. Right panel, for chewiness.

Furthermore, the PLS generated clusters were employed in a Support Vector Machine

(SVM) discriminant model to classify unknown pork loin samples into different quality

categories based on their Raman spectroscopic binary barcodes. The results are shown in

Figure 4.6. For each test, we randomly selected 100 spectra of known pork samples to

construct a training set, and then spectra from 20 randomly chosen, unclassified samples

were used for testing. The process was repeated for 5 times and the average classification

accuracy was calculated. The classification accuracy for correctly predicting a sample that

belongs to an extreme category (good vs. poor) is shown in Table 4.2. The SVM model

performed better in classifying the more tender meats. For the meats with tenderness grade

higher than 11, the classification accuracy was 95.8%; for the meats with tenderness grade

lower than 9, the classification accuracy was 83.8%. The high predictive accuracy is also

benefited from the fact that the training set and the testing set are from the same population

of meat samples. It remains to be seen how independent testing samples will affect the
predictive accuracy.
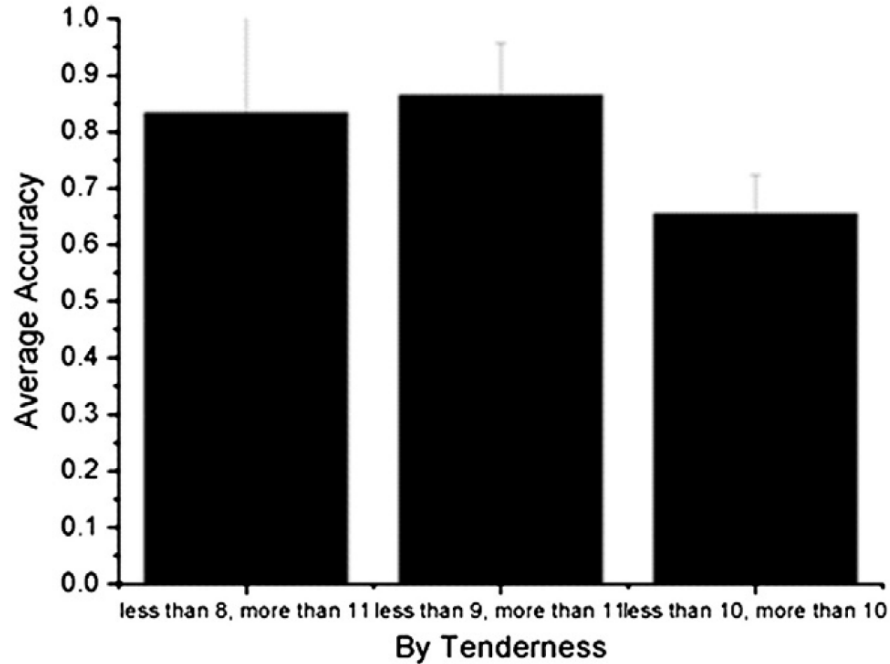
Figure 4.6 Prediction of classifying pork samples into different tenderness grades based on their
Raman spectroscopic barcodes.
Each error bar indicates the standard deviation of classification accuracy from 5 training and testing
using Support Vector Machine.

Table 4.2 The average classification accuracies for pork Raman spectra between poor (tenderness
grade b 9) and good (tenderness grade > 11).
The average accuracies are calculated from 5 repetitions of training and testing using Support Vector
Machine.

	Poor	Good
Classified as "Poor"	83.80%	4.20%
Classified as "Good"	16.20%	95.80%

We also investigated the effect of changing the definition of the grade categories on
the classification accuracy. We reset the "poor" class to be samples with tenderness scores
below 8, instead of 9. The overall prediction accuracy decreased slightly from 88% to 83%;

however, if instead of defining "poor" and "good" classes at the extreme ends of the tenderness spectrum, a simple separation line was set (tenderness score = 10) to define the two classes, the prediction accuracy diminished significantly to 64%. Apparently, pork samples that belong to the medium quality category are more difficult to predict based on their Raman spectroscopic characteristics.

As a comparison, correlation between star probe values and sensory tenderness of the pork samples was shown in Figure 4.7A. The correlation coefficient (R) was −0.31886, suggesting that mechanical measurement correlates moderately with sensory tenderness. Interestingly, it was observed that the prediction accuracy for star probe categories (in parallel with the tenderness categories) was less than that for the actual sensory tenderness (73% for star probe vs. 85% for tenderness). Since tenderness is primarily determined by the biochemical characteristics of the meat, Raman spectrosensing, which measures the biochemical characteristics of the meat, is indeed a better tool to predict sensory tenderness than to predict mechanical properties of the meat, which are only indirectly correlated to its biochemical properties.
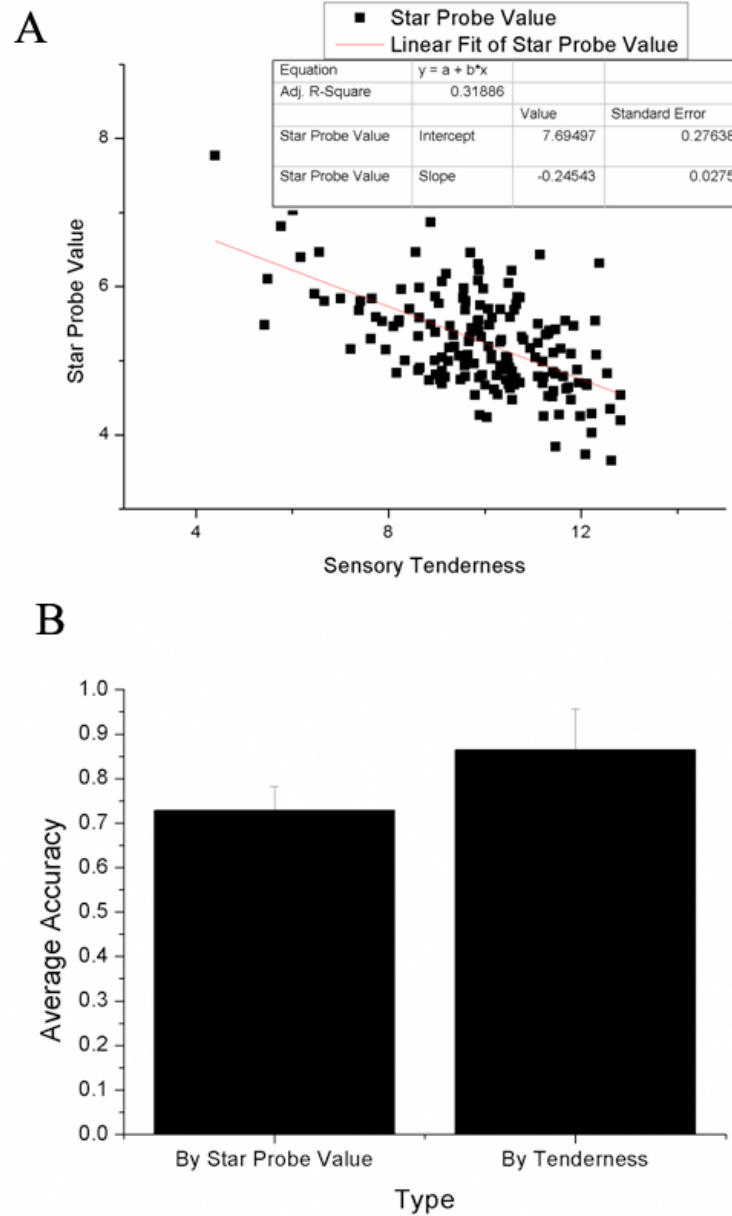
Figure 4.7 Comparison between mechanical measurements and Raman spectrosensing in determining sensory tenderness.
A. Correlations between star probe value and sensory tenderness; B. Prediction accuracy for classification of sensory tenderness and for star probe values. Each error bar indicates the standard deviation of classification accuracy from 5 training and testing using Support Vector Machine.

Classification for sensory chewiness was also conducted using similar approaches as

for sensory tenderness using the Raman spectroscopic binary barcodes for pork loin samples.

The results are shown in Table 4.3. The prediction accuracy for "good" class (chewiness b 2)

was 100% over five random tests; the prediction accuracy for "poor" class (chewiness > 4) was 83.3% over five random tests. However, if the classification criterion was set to separate the samples only into two categories with the boundary at chewiness score of 3 or 4, the prediction accuracy dropped to ~ 70% and 63%, respectively (data not shown). Similar to the case of sensory tenderness, pork samples with medium levels of chewiness are the most difficult to classify.

Table 4.3 The average classification accuracies for pork Raman spectra between poor (chewiness grade > 4) and good (chewiness grade < 2).
The average accuracies are calculated from 5 repetitions of training and testing using Support Vector Machine.

	Poor	Good
Classified as "Poor"	83.30%	0.00%
Classified as "Good"	16.70%	100.00%

Another interesting observation was that the prediction accuracy for "good" samples, either for tenderness or chewiness, was consistently better than that for "poor" samples. Further study is needed to identify the biochemical compositional markers that differentiate pork samples. Potentially the Raman spectroscopic method can become a tool to quickly identify premium meat products.

4.5 Conclusions

In this report, Partial Least Square Regression models were developed to predicate the value of sensory tenderness, chewiness and juiciness based on Raman spectroscopic characteristics of pork loins, it was demonstrated that sensory attributes of pork loins are moderately correlated to their Raman spectroscopic characteristics. Furthermore, a new Raman spectroscopic binary barcoding model was created to classify pork loins into grades by sensory tenderness and chewiness. The method was demonstrated to yield good

performance in identifying pork loins that belong to extreme categories of their sensory quality (i.e., superior and inferior).

In this study, Raman spectra were acquired from frozen/thawed meat samples, yet the sensory evaluation was performed on fresh samples. The freezing/thawing operation may change the structural characteristics of the samples, and some chemical compositional changes may have occurred during the storage. All these factors may have affected the correlations between the Raman data and the sensory data negatively. Still, the predictive accuracy was reasonably good. Potentially, Raman spectral acquisition can be done rapidly (less than 10 s) with handheld portable Raman spectrometer directly from a pork carcass inside a slaughterhouse. By applying the methods of performance-enhancing data processing and multivariate statistical discriminant modeling developed in this work, it is possible that a rapid, on-line screening tool can be developed eventually for the pork producers to quickly select meats with superior quality and/or poor quality to better serve customers.

4.6 Acknowledgments

4.7 References

Barbut, S., A. Sosnicki, et al. (2008). "Progress in reducing the pale, soft and exudative problem in pork and poultry meat." Meat Science **79**(1): 46-63.

Beattie, J. R., S. E. J. Bell, et al. (2008). "Preliminary investigations on the effects of ageing and cooking on the Raman spectra of porcine longissimus dorsi." Meat Science **80**(4): 1205-1211.

Beattie, R. J., S. J. Bell, et al. (2004). "Preliminary investigation of the application of Raman spectroscopy to the prediction of the sensory quality of beef silverside." Meat Science **66**(4): 903-913.

Bee, G., A. L. Anderson, et al. (2007). "Rate and extent of pH decline affect proteolysis of cytoskeletal proteins and water-holding capacity in pork." Meat Science **76**(2): 359-365.

Ben-Hur, A., D. Horn, et al. (2002). "Support vector clustering." The Journal of Machine Learning Research **2**: 125-137.

Böcker, U., R. Ofstad, et al. (2006). "Salt-induced changes in pork myofibrillar tissue investigated by FT-IR microspectroscopy and light microscopy." Journal of Agricultural and Food Chemistry **54**(18): 6733-6740.

Chan, D., P. Walker, et al. (2002). "Prediction of pork quality characteristics using visible and near-infrared spectroscopy." Transactions of the ASAE **45**(5): 1519-1527.

Cristianini, N. and J. Shawe-Taylor (2000). An Introduction to Support Vector Machines and other Kernel-Based Learning Methods. Cambridge, UK, Cambridge University Press.

Fox, J., S. Wolfram, et al. (1980). "Physical, chemical, sensory, and microbiological properties and shelf life of PSE and normal pork chops." Journal of Food Science **45**(4): 787-790.

Herrero, A. M. (2008). "Raman spectroscopy a promising technique for quality assessment of meat and fish: A review." Food Chemistry **107**(4): 1642-1651.

Huff-Lonergan, E. and S. M. Lonergan (2005). "Mechanisms of water-holding capacity of meat: The role of postmortem biochemical and structural changes." Meat Science **71**(1): 194-204.

Huff Lonergan, E., W. Zhang, et al. (2010). "Biochemistry of postmortem muscle: Lessons on mechanisms of meat tenderization." Meat Science **86**(1): 184-195.

Jeremiah, L. and D. Phillips (2000). "Evaluation of a probe for predicting beef tenderness." Meat Science **55**(4): 493-502.

Kim, Y. H., E. Huff-Lonergan, et al. (2010). "High-oxygen modified atmosphere packaging system induces lipid and myoglobin oxidation and protein polymerization." Meat Science **85**(4): 759-767.

Kim, Y. H., S. M. Lonergan, et al. (2010). "Protein denaturing conditions in beef deep semimembranosus muscle results in limited μ-calpain activation and protein degradation." Meat Science **86**(3): 883-887.

Liu, Y., B. G. Lyon, et al. (2003). "Prediction of color, texture, and sensory characteristics of beef steaks by visible and near infrared reflectance spectroscopy: A feasibility study." Meat Science **65**(3): 1107-1115.

Lonergan, S., K. Stalder, et al. (2007). "Influence of lipid content on pork sensory quality within pH classification." Journal of Animal Science **85**(4): 1074-1079.

Melody, J., S. Lonergan, et al. (2004). "Early postmortem biochemical factors influence tenderness and water-holding capacity of three porcine muscles." Journal of Animal Science **82**(4): 1195-1205.

Mennecke, B., A. Townsend, et al. (2007). "A study of the factors that influence consumer attitudes toward beef products using the conjoint market analysis tool." Journal of Animal Science **85**(10): 2639-2659.

Mitsumoto, M., S. Maeda, et al. (1991). "Near-Infrared spectroscopy determination of physical and chemical characteristics in beef cuts." Journal of Food Science **56**(6): 1493-1496.

Park, B., Y. Chen, et al. (1998). "Near-infrared reflectance analysis for predicting beef longissimus tenderness." Journal of Animal Science **76**(8): 2115-2120.

Patel, I., W. Premasiri, et al. (2008). "Barcoding bacterial cells: A SERS based methodology for pathogen identification." Journal of Raman Spectroscopy **39**(11): 1660-1672.

Rincker, P., J. Killefer, et al. (2008). "Intramuscular fat content has little influence on the eating quality of fresh pork loin chops." Journal of Animal Science **86**(3): 730-737.

Rodbotten, R., B. H. Mevik, et al. (2001). "Prediction and classification of tenderness in beef from non-invasive diode array detected NIR spectra." Journal of Near Infrared Spectroscopy **9**(3): 199-210.

Smith, R., N. Gabler, et al. (2011). "Effects of selection for decreased residual feed intake on composition and quality of fresh pork." Journal of Animal Science **89**(1): 192-200.

Steinwart, I. and A. Christmann (2008). Support Vector Machines. New York, NY, USA, Springer Verlag.

Vapnik, V. and A. Chervonenkis (1964). "A note on one class of perceptrons." Automation and Remote Control **25**(1).

Venel, C., A. M. Mullen, et al. (2001). "Prediction of tenderness and other quality attributes of beef by near infrared reflectance spectroscopy between 750 and 1100 nm: Further studies." Journal of Near Infrared Spectroscopy **9**(3): 185-198.

Wheeler, T., S. Shackelford, et al. (2000). "Variation in proteolysis, sarcomere length, collagen content, and tenderness among major pork muscles." Journal of Animal Science **78**(4): 958-965.

Zhang, W., S. M. Lonergan, et al. (2006). "Contribution of postmortem changes of integrin, desmin and μ-calpain to variation in water holding capacity of pork." Meat Science **74**(3): 578-585.

Chapter 5.   RAPID EVALUATION OF BOAR TAINT USING RAMAN SPECTROSCOPY AND CHEMOMETRICS

Modified from a paper prepared to submit

Qi Wang[1], Karl Hamouche[1] and Chenxu Yu[1]

[1]Department of Agricultural and Biosystems Engineering, Iowa State University, Ames, Iowa, 50011

5.1 Abstract

Boar taint is an undesirable flavor in cooked pork from male pigs that mainly originates from androstenone and skatole compounds. Conventional detection methods for boar taint require time-consuming sample preparation and sophisticated instrumentation that are not suitable for onsite evaluation of freshly slaughtered carcasses. In this study, Raman spectroscopic screening method in conjunction with discriminant modeling was developed to rapidly determine whether or not androstenone (AN) and/or skatole (SK) levels in pork back fat collected from male pigs are above designated threshold levels. Based on the spectral readings, classification of the fat samples into two categories (high AN vs. low AN, high SK vs. low SK) was achieved at 90% accuracy. By implementing a simple methanol extraction method to remove SK and AN from the fat samples, classification was further refined to four categories (high, medium high, medium low, low) for both An and SK, with improved accuracies (94-95%). The innovative Raman spectroscopic screening has the potential to become a rapid evaluation routine for onsite boar taint monitoring in slaughter houses.

5.2 Introduction

Boar taint is the offensive odor or taste that can be evident during the cooking or eating of pork or pork products derived from non-castrated male pigs once they reach puberty.

Studies show that about 75% of consumers are sensitive to boar taint so it is necessary for pork producers to control it(Bonneau, Le Denmat et al. 1992). Androstenone (AN) and skatole (SK), two malodorous fat-soluble compounds, are considered to be the two main contributors to boar taint. Androstenone, first isolated from boar fat by Patterson(Patterson 1968), is produced in the testes as male pigs reach puberty and exhibiting an intense urine-like odor. The biology of androstenone in pigs and its contribution to boar taint has been extensively studied (Brooks and Pearson 1986). Skatole is a byproduct of intestinal bacterial digestion of amino acid. It is produced in equivalent amounts in both males and female pigs, but it is poorly metabolized and eliminated by males, hence it tends to accumulate in the fat of male pigs (Squires and Schenkel 2009). Its contribution to boar taint has been established in a number of studies (Hansson, Lundstrom et al. 1980; Miller, Kottler et al. 2003; Schiestl and Roubik 2003). Both of the two malodorous compounds contribute to boar taint, and they interact with each other's presence in a complex manner which is still not fully understood. Androstenone production and storage is highly dependent on pigs' age, weight and genotype (Bonneau 1982), which differ widely in various countries. From a practical point of view, it can be tempting to rely more heavily on skatole for evaluating boar taint risk in carcasses or meat, since this compound can be measured on the slaughter-line, whereas there is no such readily available method for fat-dissolved androstenone measurement. So far, the "skatole equivalent method" is also the only method that has been taken into use on an industrial scale at-line for the purpose of sorting boar tainted carcasses. It is a colorimetric method based on solvent extraction of fat followed by addition of reagent and spectrophotometric fluorescence measurementl(Mortensen and Sørensen 1984).

Androstenone and skatole only start to accumulate in the fat of pigs when they sexually mature. For centuries, male pigs have been castrated to prevent boar taint which can show up in a small percentage of boars in some breeds (Jeong, Choi et al. 2008). Improvest®, a veterinary pharmaceutical produced by Pfizer (Pfizer Animal Health, Kalamazoo, MI), is a 9 amino-acid base pair gonadotropin releasing factor (GnRF) conjugate that immunologically "castrate" male pigs by disrupting their reproductive functions. A recent study showed that immunological castration with Improvest® prevents androstenone accumulation in male pigs even when allowed to grow to ending live weights over 130 kg (Boler 2011). Thus, measuring the content of androstenone in back fat of pigs is a good way of monitoring whether or not the "Improvest®" administered has functioned properly. Use of Improvst® has been shown to improve cutting yields of male pigs with no negative impact on fresh and cured product characteristics and quality (Boler 2011).

The risk of boar taint development increases as concentration of androstenone goes above 500 ng/g fat, and especially above 1000 ng/g fat; for skatole, the risk of boar taint goes up as the concentration exceeds 200-250 ng/g fat. These two compounds may interact with each other in complex ways that further increase the risk of boar taint development(Robic, Larzul et al. 2008), hence monitoring their concentrations in parallel is important. The pig fat matrix is complicated. Several types of steroids and organic compounds can be found in the pig fat. These compounds affect the quantitative analysis of androstenone and skatole. Boar taint was traditionally evaluated using sensory profiling in scientific study(Furnols, Guerrero et al. 2007). In recent years instrumentation analysis has been applied to evaluate boar taint. LC-MS (Verheyden, Noppe et al. 2007; Chen, Ren et al. 2010) and HPLC (Garcia-Regueiro and Diaz 1989; Banon, Costa et al. 2003) methods were developed for

accurate quantification of androstenone and skatole in pig fat. However, these assays require time-consuming sample preparation, and therefore are not suitable for onsite implementation in slaughterhouses. (Henion, Brewer et al. 1998).

Pig fats, with different compositions of dissolved steroids and other organic compounds, display specific Raman spectroscopic fingerprints which are direct reflection of their chemical makeup(Schrader and Steigner 1973; Harada, Miura et al. 1986). Fats containing higher levels of androstenone and skatole compounds may yield spectroscopic signatures that are distinguishable from fats that only contain low levels of these compounds, although accurate quantification of the relevant compounds (i.e., androstenone and skatole) may not be feasible. Nevertheless, to determine whether a pork product is acceptable to consumers, it may not be necessary to accurately evaluate the exact quantity of the compounds; it might be sufficient to just determine if a threshold (i.e., 500 or 1000 ng/g of AN) has been reached and hence a "good" or "bad" classification can be granted to the product. Raman spectroscopy combined with multivariate discriminant analysis may provide a solution to address this need. Statistically significant differences between spectroscopic signatures that represent different categories (i.e., High vs. low androstenone/skatole) of boar taint compounds could be identified when a large number of samples are analyzed; and using these signatures a discriminant model can be created to differentiate these categories(Guzmán, Baeten et al. 2012); Once the discriminant model is established, any unknown sample can be tested against the model to determine to which category it belongs with good reliability and accuracy.

The objective of this study is to develop a Raman spectroscopic screening method in conjunction with discriminant modeling to rapidly analyze pig fat samples to classify them into categories based on levels of AN or SK.

5.3 Materials and methods

5.3.1 Sample preparation and Raman spectral acquisition

105 pork fat samples (some are from pigs treated with Improvest®) with the concentration of androstenone ranging from extremely low (<20 ng/g), to very high (>2000 ng/g) and concentration of skatole between ~30 ng/g to 700 ng/g, were acquired from Pfizer Animal Health (Kalamazoo, MI). Residual muscle tissues were carefully trimmed and samples were then mounted onto glass microscope slides and subjected to Raman spectroscopic measurement.

For samples subjected to AN/SK removal through methanol extraction, 5g of fat sample were placed in glass disposable centrifuge tube in boiling water bath for 5 mins to melt the fat. 2ml methanol was then added into the tube. After vigorous stirring, the sample was centrifuged at 4 °C 2 minutes to separate the supernatant methanol from the fat. Supernatant is micropipetted into the lid of an eppendorf tube and covered with cover slip for Raman measurements. The supernatant contains AN and SK extracted from the fat samples.

Raman measurements were performed using a DXR Dispersive Raman Microscope (Thermo Scientific, Inc., Madison, WI) with 780nm, 14 mW excitation laser at ambient temperature. Raman spectra were collected with 2s exposure time from 200 and to 2800 cm^{-1} at a resolution of 1 cm^{-1}. At least 5 replicates were acquired from each sample.

5.3.2 Spectra preprocessing and data compression

All spectra were baseline corrected, normalized and smoothed using 5-point averaging smoothing algorithm to reduce the baseline variability at the region between 200 cm^{-1} to 2800 cm^{-1}. The first derivative and second derivative spectra were calculated from the normalized spectra. To highlight the important spectral signatures representing the chemical landscape of each sample, and to minimize the effect of variations in the spectral data due to peak intensities, a binary barcode was developed. A binary value (0 or 1) was assigned to each second derivative spectral data point primarily based on the sign or the value of the second derivative, i.e., 1 for upward curvature (positive second derivatives), and 0 for downward curvature (negative second derivatives).

In Raman spectra, each wavenumber represents a dimension or variable. Commonly, data of one Raman spectrum contain thousands of dimensions, which bring a great challenge for following statistical analysis. For discriminant analysis, as the dimensions of the data become large, the limitation on the capability of detecting distinguishable classes becomes severe. Due to the fact that most statistical methods are based on optimization criteria, it is advisable to reduce the dimension of the problem. This dimension reduction results in decreasing computational costs and increasing probability of finding the best model representing the data. For this purpose a Principal component regression (PCA) is executed for data compression in this study.

All data processing was conducted using R, a widely used language and software tool for statistical computing and graphics

5.3.3 Cross-validation and discriminant analysis

Cross-validation is a technique for assessing how the results of a statistical analysis will generalize to an independent dataset. One round of cross-validation involves partitioning a sample of data into complementary subsets, performing the analysis on one subset (called the training set), and validating the analysis on the other subset (called the validation set or testing set). To reduce variability, multiple rounds of cross-validation are performed using different partitions, and the validation results are averaged over the rounds.

In this study, the discriminant model to classify "unknown" spectra into each category was developed using support vector machine algorithm(Steinwart and Christmann 2008) implemented based on Matlab SVM toolbox(Canu, Grandvalet et al. 2005) or R package "e1071"(Karatzoglou, Meyer et al. 2005; Dimitriadou, Hornik et al. 2007) in R with folded cross validation.

5.4 Results

5.4.1 Binary spectra

Raman peaks are represented by their wavenumber (Raman shift) and intensity. The peak intensities are dependent on many factors that may vary from sample to sample (i.e., sample size, exposure time, etc.), but their Raman shifts remain identical as long as the molecular makeup is the same. Therefore, the binary bar-codes are calculated from signs of second derivative spectra to highlight the important chemical landscape of each sample and minimize the effect of variations. A threshold for zeros was selected as a percentage of the maximum absolute value of the second derivative for positive second derivative readings (for all absolute value larger than the threshold, 1 was retained; otherwise it was switched to 0). Contribution to the measured spectra from low level background noises was thus removed by

assigning 0 to it. Therefore, for fat samples with very low AN and/or SK levels, 0 may be assigned to unique AN and/or SK peaks whilst 1 will be retained if the AN and SK levels are higher. The distinction between low/high AN/SK samples will be highlighted. The threshold value was determined experimentally by finding the barcodes that provided the best prediction for differentiating the two categories (high vs. low). Figure 5.1 shows the typical binary barcodes generated for fat samples with low vs. high androstenone (>500 ng/g fat) and low v.s. high skatole (>250 ng/g fat) levels. Here the optimal threshold value was found to be 10%.
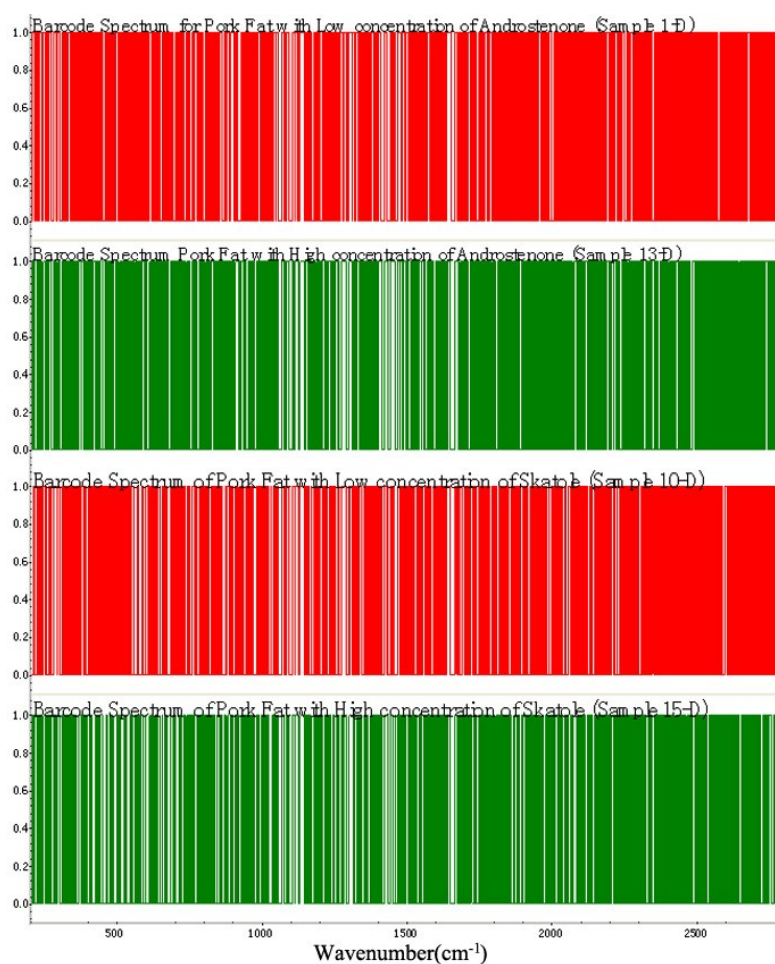

Figure 5.1 Binary barcode based on secondary derivative sign.
C-C at 860-880 cm^{-1}, 1050-1100 cm^{-1} C=C at 1290-1320 cm^{-1}, -CH3 at 1290-1310, 1430-1460 cm^{-1}, C=O at 1740-1750 cm^{-1}.

5.4.2 Accuracy using spectra from un-treated pork fat

The discriminant model to classify "unknown" spectra into each category (high AN, low AN, high SK, low SK) was developed using Support Vector Machine (SVM) algorithm implemented with Matlab SVM toolbox. Partial Least Square Regression (PLSR) algorithm was used to further compress the data sets (the binary barcodes) and generated inputs for the SVM model. The main goal here is to accurately classify fat samples that are at the two extreme ends of the AN/SK levels. The measured spectra of fat samples were divided into 2 groups (i.e., AN high/low groups and SK high/low groups) according to the values of their AN and SK contents.

Training (calibration) sets and test sets were set in such a way that both the training sets and the test sets showed approximately the same distribution of one specific variable (i.e., they have roughly the same numbers of "high" or "low" entries). Different training/test sets were chosen randomly to calculate the average classification accuracy (over 10 random sampling). Given a set of training data, each marked as belonging to one of two categories; an SVM training algorithm builds a model that assigns new data points into one category or the other. Penalty coefficient of optimization (C) and kernel function are the main parameters of SVM training algorithm. A Gaussian radial basis (RBF) kernel, which is one of the most popular kernel function, was selected for SVM, and the optimal values for C and σ of RBF function, which determine the area of influence the support vector has over the data space, are 100 and 1.6, respectively. Table 5.1 shows the average classification accuracy for the samples with high/low AN and SK levels, with a list of different cutoff thresholds for high/low levels for AN and SK, respectively.

Table 5.1 The average classification accuracies between high/low samples using the whole spectra ranging from 200-2800 cm^{-1}.

Skatole threshold (ng/g)	The number of samples tested with skatole higher than threshold	The accuracy of classification %	Androstenone threshold (ng/g)	The number of samples which androstenone is more than threshold	The accuracy of classification for androstenone %
300	5	92.31	2000	7	92.86
200	17	83.33	1000	31	89.92
150	29	92.86	800	36	85.71
			500	44	91.33

The best classification accuracy for both AN and SK is ~92%, for cutoff threshold values towards the extreme ends. The classification accuracy is lower when the cutoff-threshold values for high/low categories are in the intermediate range. It confirms the reasoning that the classification would be the most accurate for samples at the extreme ends of AN or SK contents.

With the direct spectral analysis, major improvement over the prediction accuracy would be difficult. The fat samples are predominantly comprised of triglyceride, at 10^{6-8} times higher content than AN and SK. The spectral signatures of AN and SK are often overwhelmed by that of triglyceride. Besides, the fat samples are far from homogeneous and consistent, variations from sample to sample contribute significantly to their spectral differences. When a new, unknown sample was subjected to the discriminant analysis, these complications add onto the difficulty of correctly classifying the sample into the proper category.

A support vector machine model was developed to further classify the samples into "bands" of AN and SK contents based on their binary barcodes. The "bands" are listed in Table 5.2, with the classification accuracy.

Table 5.2 Classification accuracy with different "bands" of AN and SK contents.

Skatole contents	The number of spectra tested within each band	The accuracy of classify for skatole %	Androstenone coontents	The number of spectra tested within each band	The accuracy of classify for androstenone
>150	5	91.67	>2200	4	91.67
130-150	7	83.33	2000-2200	6	90.91
110-130	8	81.82	1800-2000	5	75
90-110	6	68.33	1600-1800	10	75
70-90	11	66.67	1400-1600	12	72.73
50-70	7	78.33	1200-1400	15	75
<50	4	91.67	1000-1200	9	73.64
			800-1000	11	76.67
			600-800	22	78.33
			400-600	4	85
			<400	19	95

The accuracy of classifying samples into "bands" of SK and AN contents again confirms the observation that the classification model yields the best results for samples at the extreme ends of AN and SK contents. The accuracy deteriorates significantly for samples with intermediate AN/SK contents. Generally, the lack of accuracy is mainly caused by the weak signals coming from the AN and SK, and the strong interferences from other ingredient of the samples, as well as the unaccounted for variations from sample-to-sample due to their uniqueness in terms of chemical composition.

5.4.3 Differentiation accuracy of processed pork fat samples before/after methanol based removal

If the AN and/or SK contents of a fat sample is high, when these ingredients are removed from the sample by methanol extraction, the Raman spectroscopic signatures of the treated sample would differ from that of the original sample due to the disappearance of AN/SK specific peaks. A differentiation test would yield a positive result with high accuracy (i.e., samples before/after treatment are distinguishable). On the other hand, if the initial AN/SK contents are low, their removal would not alter the spectral signatures much, and a

differentiation test may yield a negative results (i.e., samples before/after treatment are indistinguishable). In this approach, the analysis is conducted on the same fat sample before/after treatment, hence the great variations across fat samples from different sources won't affect the results. It is also hypothesized that the differentiation accuracy would be directly correlated to the AN/SK contents of the fat sample, as high AN/SK content should yield high differentiation accuracy.

105 samples with various AN and SK contents were investigated. A summary of the sample SK and AN contents is listed in Table 5.3 and 5.4.

Table 5.3 Distribution of SK content data (Unit: ng/g fat).

Minimum	1st Quartile	Median	Mean	3rd quartile	Maximum
6.893	52.5	96.1	168.9	157.8	800.6

Table 5.4 Distribution of AN content data (Unit: ng/g fat).

Minimum	1st Quartile	Median	Mean	3rd quartile	Maximum
BLQ<(20)	355.6	1487	1669	2715	6245

To analyze the real fat samples, we first categorized the samples into 3 groups, high (H), medium (M) and low (L), the grouping criteria are listed in Table 5.5 and 5.6, respectively for AN and SK.

Table 5.5 Grouping for SK classification (Unit: ng/g fat).

	H	M	L
Grouping	≥500	100-500	<100
Spectra number	60	214	366

Table 5.6 Grouping for AN classification (Unit: ng/g fat).

	H	M	L
Grouping	≥1500	600-1500	≤600
Spectra number	316	114	210

Table 5.7 shows the differentiation accuracy for samples from the three groups before/after the AN/SK removal treatments. Evidently, the differentiation accuracy is not high, and there is no clear trend as whether the accuracy is dependent on the AN/SK contents in the fat sample, as one may have expected.

Table 5.7 Differentiation accuracy of samples with different SK/AN contents before/after methanol based removal.

Skatole group	The number of spectra within each group	The average accuracy of differentiation	Androstenone group	The number of spectra within each group	The average accuracy of differentiation
H	60	75.0±1.8	H	316	70.2±2.7
M	214	66.1±2.8	M	114	82.4±1.2
L	366	63.3±3.5	L	210	61.1±2.3

There are several reasons for this to happen. In each group the actual AN or SK contents cover a large range, which may lead to variations in the differentiation analysis that leads to indefinite results. The fat samples may respond to the extraction-based removal procedure differently, given the complex nature of the fat.

5.4.4　Classification accuracy of methanol samples after methanol based removal

The extraction procedure generates not only processed fat samples (after AN/SK removal), but also methanol samples (with AN/SK extracted into them). Methanol is a simple, pure substrate before the extraction, which provides a consistent background matrix that can be used to establish a baseline for the subsequent differentiation/classification analysis.

Figure 5.2 shows the Raman spectra of pure methanol (green) and methanol after extraction. It is obvious that the extraction has brought new chemical substance into the methanol and changed its spectral characteristics. A quick differentiation analysis yields a 100% differentiation accuracy for all fat samples, even the ones with very low AN/SK contents.
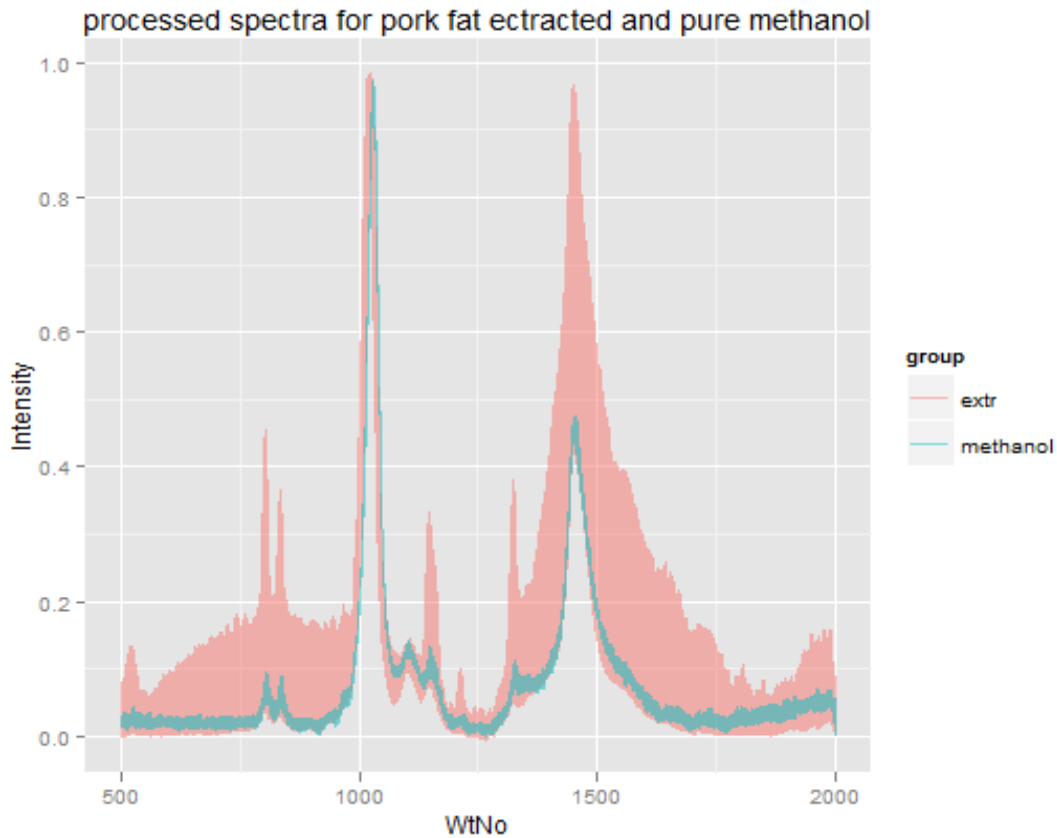

Figure 5.2 Processed spectra for pork fat extracted and pure methanol.

We then investigated whether we can use the extracted methanol spectra as classifiers to classify the fat samples. In this effort, we categorized the fat samples into four groups, as shown in Table 5.8 and 5.9. After spectra pre-processing and data compression, the classification model was developed using support vector machine algorithm (Steinwart and Christmann 2008) implemented using R package "e1071"(Karatzoglou, Meyer et al. 2005;

Dimitriadou, Hornik et al. 2007) with folded cross validation. Figures 5.3 and 5.4 show the classification accuracy for SK and AN of all fat samples.

Table 5.8 Grouping for SK classification (Unit: ng/g fat).

	H	MH	ML	L
Grouping	≥157.8	96.1≤MH<157.8	52.5<MH<96.1	≤52.5
Spectra number	174	158	142	166

Table 5.9 Grouping for AN classification (Unit: ng/g fat).

	H	MH	ML	L
Grouping	≥2715	1487≤MH<2715	355.6<MH<1487	≤355.6
Spectra number	146	170	154	170
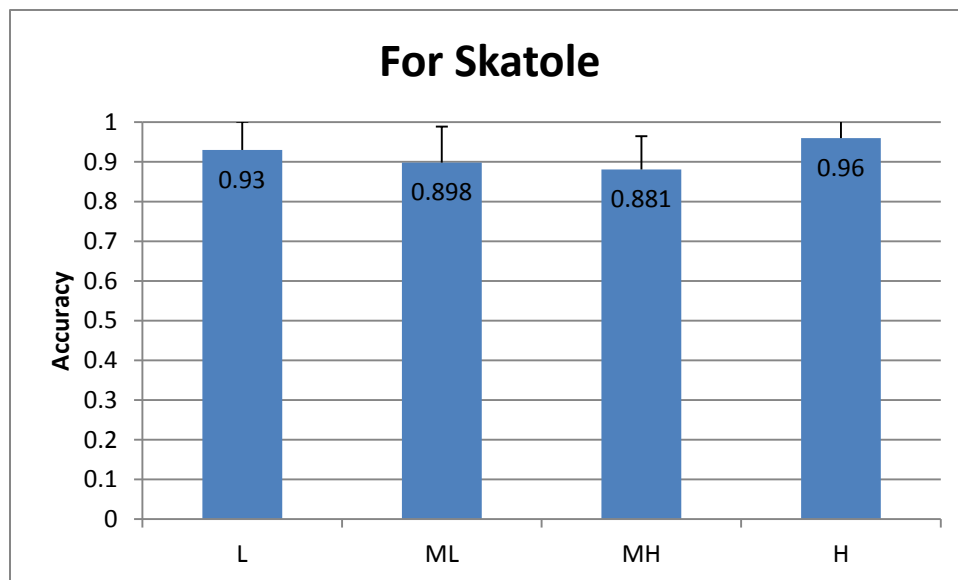
Figure 5.3 Classification accuracy for SK into 4 content groups.
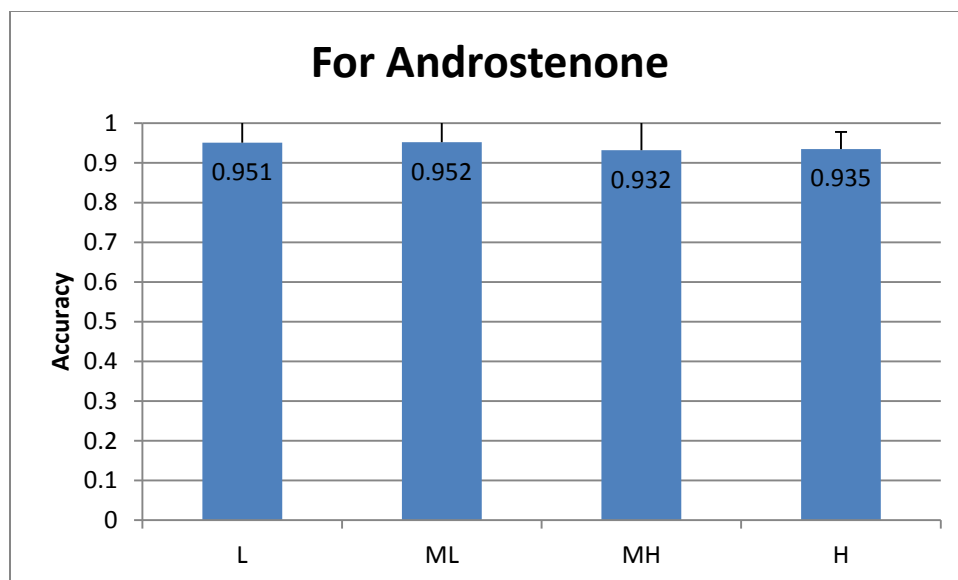
Figure 5.4 Classification accuracy for AN into 4 content groups.

It is encouraging that the simple methanol extraction significantly improved the classification accuracy, especially for the AN analysis. The classification accuracy for all four groups is at ~94-95%. We have further simplified the protocol to a 1 min microwave heating followed by a 30 s methanol extraction. The methanol is then subjected to a spectroscopic measurement which takes 30 s. The total time for one analysis is about 2 minutes. A fully automated system can be built with a portable Raman spectrometer for onsite sample evaluation.

5.5 Conclusions

In this study, Raman spectroscopic screening methods in conjunction with multivariate discriminant analysis were developed for quick evaluation of contents of boar taint compounds in back fat samples directly collected from pig carcasses. With a simple, easy-to-use sample preparation protocol based on methanol extraction, classification of fat samples based on their androstenone or skatole contents into qualitative categories can be achieved with reasonably high accuracy (~95%). The easy-to-use nature of this method

makes it an appealing alternative to time consuming and sophisticated lab protocols that are the norm today for boar taint analysis. Potentially Raman screening can become a valuable option for onsite evaluation of boar taint in slaughterhouses.

5.6 Acknowledgments

5.7 References

Banon, S., E. Costa, et al. (2003). "A comparative study of boar taint in cooked and dry-cured meat." Meat Science **63**(3): 381-388.

Boler, D. D. (2011). Effects of gonadotropin releasing factor immunological (Improvest®) on carcass characteristics, pork quality, and further processing characteristics of finishing male pigs. Animal Sciences, University of Illinois at Urbana-Champaign. **Ph.D.**

Bonneau, M. (1982). "Compounds responsible for boar taint, with special emphasis on androstenone: A review." Livestock Production Science **9**(6): 687-705.

Bonneau, M., M. Le Denmat, et al. (1992). "Contributions of fat androstenone and skatole to boar taint: Sensory attributes of fat and pork meat." Livestock Production Science **32**(1): 63-80.

Brooks, R. and A. Pearson (1986). "Steroid hormone pathways in the pig, with special emphasis on boar odor: A review." Journal of Animal Science **62**(3): 632.

Canu, S., Y. Grandvalet, et al. (2005). "SVM and kernel methods matlab toolbox." Perception Systemes et Information **2**: 2.

Chen, G., L. Ren, et al. (2010). "Determination of androstenone levels in porcine plasma by LC-MS/MS." Food Chemistry **122**(4): 1278-1282.

Dimitriadou, E., K. Hornik, et al. (2007). "The e1071 package." CRAN.

Furnols, M. F. I., L. Guerrero, et al. (2007). "Sensory characterization of boar taint in entire male pigs." Journal of Sensory Studies **15**(4): 393-409.

Garcia-Regueiro, J. and I. Diaz (1989). "Evaluation of the contribution of skatole, indole, androstenone and androstenols to boar-taint in back fat of pigs by HPLC and capillary gas chromatography (CGC)." Meat Science **25**(4): 307-316.

Guzmán, E., V. Baeten, et al. (2012). "A portable Raman sensor for the rapid discrimination of olives according to fruit quality." Talanta **93**: 94-98.

Hansson, K. E., K. Lundstrom, et al. (1980). "The importance of androstenone and skatole for boar taint." Swedish Journal of Agricultural Research **10**(4): 167-173.

Harada, I., T. Miura, et al. (1986). "Origin of the doublet at 1360 and 1340 cm^{-1} in the Raman spectra of tryptophan and related compounds." Spectrochimica Acta Part A: Molecular Spectroscopy **42**(2-3): 307-312.

Henion, J., E. Brewer, et al. (1998). "Sample preparation for LC/MS/MS: Analyzing biological and environmental samples." Analytical Chemistry **70**(19): 650-656.

Jeong, J., J. Choi, et al. (2008). The effects of immunocastration on meat quality and sensory properties of pork loins. Proceedings of the 20th International Pig Veterinary Society Congress, Durban, South Africa.

Karatzoglou, A., D. Meyer, et al. (2005). Support vector machines in R. Vienna, Department of Statistics and Mathematics, Department of Statistics and Mathematics, WU Vienna University of Economics and Business.

Miller, M., S. Kottler, et al. (2003). "3-Methylindole induces transient olfactory mucosal injury in ponies." Veterinary Pathology **40**(4): 363-370.

Mortensen, A. and S. Sørensen (1984). Relationship Between Boar Taint and Skatole Determined with a New Analysis Method. Proceedings of the 30th European meeting of meat research workers, Bristol, England.

Patterson, R. (1968). "5α-androst-16-ene-3-one: Compound responsible for taint in boar fat." Journal of the Science of Food and Agriculture **19**(1): 31-38.

Robic, A., C. Larzul, et al. (2008). "Genetic and metabolic aspects of androstenone and skatole deposition in pig adipose tissue: A review." Genetics Selection Evolution **40**(5): 581.

Schiestl, F. and D. W. Roubik (2003). "Odor compound detection in male euglossine bees." Journal of Chemical Ecology **29**(1): 253-257.

Schrader, B. and E. Steigner (1973). "Raman spectroscopy of steroids." Modern Methods of Steroid Analysis: 231.

Squires, E. and F. Schenkel (2009). Potential strategies to reduce boar taint. Guelph, ON, Canada, Department of Animal and Poultry Science, University of Guelph**:** 105-114.

Steinwart, I. and A. Christmann (2008). Support Vector Machines. New York, NY, USA, Springer Verlag.

Verheyden, K., H. Noppe, et al. (2007). "Development and validation of a method for simultaneous analysis of the boar taint compounds indole, skatole and androstenone in pig fat using liquid chromatography-multiple mass spectrometry." <u>Journal of Chromatography A</u> **1174**(1-2): 132-137.

Chapter 6.   GENERAL CONCLUSIONS AND FUTURE PERSPECTIVE

6.1 General Conclusions

In this dissertation, the potential of using Raman spectroscopy as an effective detection technique for glaucoma at both late and early stages was explored. It was demonstrated that reproducible Raman spectra with good signal quality can be obtained from canine retinal tissue sections. With multivariate discriminant analysis, a support vector machine classification model was developed to differentiate retinal ganglion cells from late-stage glaucomatous versus healthy canine tissues based on their Raman spectroscopic signatures. Furthermore, spectroscopic markers were identified associated with different neuropathic conditions (i.e., AEIOP and CON). Since AEIOP mimics the pathological symptoms of acute early stage glaucoma, it was demonstrated that Raman spectroscopic screening could potentially become a powerful tool for detection and characterization of early stages of the disease.

The feasibility of applying Raman spectroscopic method to evaluate and predict tenderness, juiciness and chewiness of fresh, uncooked pork were also proved here. A new Raman spectroscopic binary barcoding model was created to classify pork loins into extreme categories (i.e., superior and inferior) of sensory tenderness and chewiness with reasonably good prediction accuracy. Raman spectra can be acquired rapidly (less than 10 seconds) with handheld portable Raman spectrometer directly from a pork carcass inside a slaughterhouse. It is possible that a rapid, on-line screening tool can be developed eventually for meat processers to quickly select meats with superior quality to better serve consumers.

Another problem the pork industry is facing is to quickly evaluate undesirable boar taint in pork products. There is still no method available for in-line or onsite detection of boar taint in freshly slaughtered carcasses. In this dissertation, Raman spectroscopic screening method in conjunction with discriminant modeling was developed to tackle this problem. It was demonstrated that rapid determination of whether or not major boar taint compounds (i.e., androstenone (AN) and/or skatole (SK)) are beyond certain threshold levels could be made with good accuracy (>90%) with direct analysis of pork backfat. With the help of a simple methanol extraction, the classification accuracy for boar taint compounds was improved to ~94-95%.

As a general conclusion, through this work it was demonstrated that Raman spectroscopic methods are powerful tools for the analysis of biological samples. It is particularly suitable for the identification of chemical variations in biological samples, caused by differences in molecular compositions in the samples. These differences can be the result of onset and progression of diseases, or genetic heritage of individual animals. With the help of multivariate discriminant analysis, the spectroscopic screening can be successfully implemented to distinguish and differentiate various biological samples, with broad applications in agriculture, food and medical sciences.

6.2 Future Perspective

The future perspective discussion is focusing on the potential of using Raman spectroscopic screening for *in vivo* glaucoma diagnosis. *In vitro* studies in dogs have established the feasibility of identifying Raman specific spectroscopic markers that are directly related to glaucoma. Also, discriminant model was developed for the identification

of diseases tissues with good predictive accuracy. However, before *in vivo* testing can be conducted, laser safety issues must be addressed.

As discussed before, for the 780 nm diode laser that was used in current study, the power density delivered on the sample was significantly higher than the threshold limit value (TLV), which determines the maximum permissible energy exposure to the retina in an *in vivo* measurement. To utilize Raman spectroscopy for *in vivo* imaging, the laser power density on the retina has to be greatly reduced.

One possible solution to overcome excessive retinal exposure to the high level of laser energy is to utilize pulse laser with extreme short time-gated or time-resolved detection $(10^{-12}s)$(Lippert, Gschneidtner et al. 2010). The recent dramatic advances in laser technology allow compact table-top lasers with tunable broadband spectrum, from the infrared to the visible, and with adjustable pulse durations down to few ps ($1ps=10^{-12}$) or even shorter. With such a short excitation time, time-gated or time-resolved collection of signal photons can be implemented to capture only Raman photons. Background fluorescence is eliminated (detection time is shorter than the fluorescence lifetime so that fluorescence has not developed)(Bird, Eliceiri et al. 2004), and the signal-to-noise ratio of the Raman spectral measurement can be significantly improved, allowing much weaker Raman signals to be detectable. An extremely short detection time also allows a much higher laser power to be applied without increasing the overall retinal laser energy exposure which is critical for non-invasive and damage-free diagnostics. Simple calculation reveals that at 10^{-12} exposure time, the TLV is 2601 mW/cm^2, which is much higher compared to the energy levels used in this study.

For time-correlated single photon counting system for time-resolved micro-photoluminescence (μ-PL), the samples were excited by ultrafast laser diodes (LDs) with proper spectral profiles which should be mounted onto an adjustable focal length collimating optics with a heat sink and driven by a fast pulse generator for the pulsed mode. For shorter pulses, a 10 W pumped oscillator will be used which delivers 1.1 W, sub-20 fs (femtosecond, 1fs = 0.001ps) pulse with ~70 nm bandwidth. A gradient neutral density filter combined with other neutral density filters should be inserted in the optical path to vary the excitation intensity, ideally over more than three orders of magnitude. The laser beam was either (i) lightly focused by a lens to a ~500-700 μm spot diameter for uniform excitation or, (ii) focused down to a minimum of ~10 μm diameter spot for localized excitation. The laser power was measured by an optical power meter placed before the sample. The luminescence is collected by the same focusing objective, i.e., confocal configuration, and imaged through a camera lens, giving a magnification of ~×15. This will provide diffraction limited (~1.7 μm) spatially resolved images. Sample surface tomography can be imaged a CCD camera with proper band-pass interference filter for which a ~2 μm spatial resolution can be achieved. The emissions can then spectrally resolved by a spectrometer.

Another major technical obstacle for *in vivo* Raman imaging of the retina is the design of the optical probing system. Fiber-optic probes through which electromagnetic waves are constrained and optical energy can be transported with minimal loss and at nearly constant average energy density over distances of up to several kilometers have been available since the 1970s. But most fiber-optic probes are not appropriate for collecting Raman spectra, because the fused silica that makes up the fibers generates its own Raman signal. Feld and Motz have published one design that has been particularly successful (Figure

6.1)(Motz, Hunter et al. 2004); it allows the researchers to characterize arterial plaques and breast cancer tumor margins, both during real surgeries (Römer, Brennan III et al. 1998; Manoharan, Shafer et al. 2008). Their probe, which is 2 mm in diameter, consists of a delivery fiber surrounded by a ring of collection fibers(Libby 1995). The delivery fiber has a micro optic filter on the tip that cuts out most of the fused-silica noise before the excitation beam hits the tissue. The collection fibers are also fitted with filters that cut off the reflected excitation light yet allow the Raman signal to pass back to the detector. Furthermore, the collection fibers, in which fiber-bundle imaging compression method are applied, use a multiplicity of fibers to collect a two-dimensional array of Raman spectra from a grid of samples points with all three dimensions (two spatial and one spectral) being measured simultaneously.
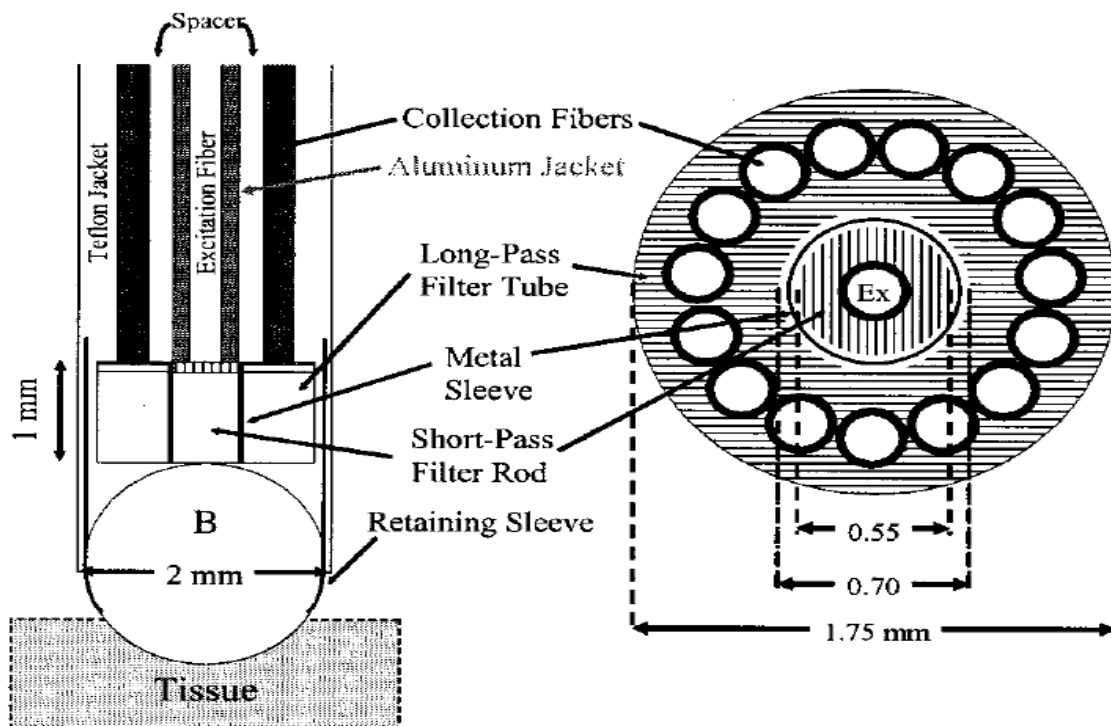
Figure 6.1 Schematic of the Feld and Motz Raman probe tip.

It shows a longitudinal view at left and a transverse cross section at the fiber-filter interface at the right. Ball lens B is in contact with the filter module that couples to the fiber bundle(Motz, Hunter et al. 2004).

Potentially, the combination of ultrafast pulsed lasers together with time-, spatially- and single photon-resolved Raman spectroscopy and fiber-bundle imaging technique, can yield a working Raman imaging system that allows *in vivo* Raman imaging of the retina It will provide fascinating opportunities to develop new *in vivo* early detection and diagnostic tool that can revolutionize clinical glaucoma diagnosis. It will make it possible to detect early glaucomatous changes even before any change in intraocular pressure, function and/or structure loss occurs.

6.3 References

Bird, D. K., K. W. Eliceiri, et al. (2004). "Simultaneous two-photon spectral and lifetime fluorescence microscopy." Applied Optics **43**(27): 5173-5182.

Libby, P. (1995). "Molecular bases of the acute coronary syndromes." Circulation **91**(11): 2844-2850.

Lippert, A. R., T. Gschneidtner, et al. (2010). "Lanthanide-based luminescent probes for selective time-gated detection of hydrogen peroxide in water and in living cells." Chemical Communications **46**(40): 7510-7512.

Manoharan, R., K. Shafer, et al. (2008). "Raman spectroscopy and fluorescence photon migration for breast cancer diagnosis and imaging." Photochemistry and Photobiology **67**(1): 15-22.

Motz, J. T., M. Hunter, et al. (2004). "Optical fiber probe for biomedical Raman spectroscopy." Applied Optics **43**(3): 542-554.

Römer, T. J., J. F. Brennan III, et al. (1998). "Histopathology of human coronary atherosclerosis by quantifying its chemical composition with Raman spectroscopy." Circulation **97**(9): 878-885.

ACKNOWLEDGEMENTS